

**SIMULATION OF REVERSE OSMOSIS AND OSMOTICALLY
DRIVEN MEMBRANE PROCESSES**

A Dissertation
Presented to
the Graduate School of
Clemson University

In Partial Fulfillment
of the Requirements for the Degree
Doctor of Philosophy
Environmental Engineering

by
Peng Xie
December 2016

Accepted by:
David A. Ladner, Committee Chair
Tanju Karanfil
Lawerence Murdoch
Scott Husson

ABSTRACT

To address the increasingly severe global water shortage and pollution problem reverse osmosis (RO) has been widely used because of its ability to produce high quality water. Meanwhile, related technologies have been developed, called osmotically driven membrane processes (ODMPs). These include forward osmosis (FO), which has potential for wastewater purification and desalination, and pressure retarded osmosis (PRO), which has the capacity to produce energy.

The main problems associated with RO and ODMPs are concentration polarization and membrane fouling which deteriorate the quality and quantity of the permeate flux and increase the operating cost of the system. The task of this study is to reduce concentration polarization and membrane fouling by providing more favorable hydrodynamics.

The majority of the efforts that try to maximize the flux and minimize the membrane fouling for these membrane filtration processes focus on membrane modification; however, the possibility of optimizing the hydrodynamics inside the membrane channel has received less attention. The hydrodynamics inside membrane channels can be greatly influenced by the presence of spacers. Spacers play an important role in defining the hydrodynamics inside the membrane channel by creating vortices in the fluid flow. A mesh spacer design is the most common type of spacer used in the spiral wound RO module. Many attempts at optimizing the current mesh spacer by changing the flow angle, filament thickness, shape, etc. have been made. Those studies suggest that higher permeate production will incur higher pressure drop. In addition, the shape of the mesh

spacer design will create dead zones and free surface area, which exacerbate the membrane fouling problem. In this dissertation is the development of a series of sinusoidal spacers to improve upon the conventional mesh spacers used in RO. This study also investigated the possibility of improving the performance of FO and PRO by using spacers.

The research consists of three sections. The first two sections focus on RO membrane filtration with sinusoidal spacers where both experiments and 3D multiphysics CFD models were used. The first section investigates the hydrodynamics and mass transfer inside sinusoidal membrane channels during seawater desalination. The CFD models were verified by comparing the permeate flux obtained from the experiments. Permeate flux and pressure drop from different sinusoidal membrane channels and the mesh spacer-filled membrane channel were compared to evaluate the performance of the spacers. Because fouling was not taken into consideration in the first section, the CFD model only studied the steady state. The results showed that the permeate flux from simulation matched well with the experiments and sinusoidal spacers were able to enhance permeate flux and reduce pressure drop.

The second section focuses on the performance of sinusoidal spacers for reducing humic acid membrane fouling. The degree of membrane fouling was evaluated through permeate flux decline over time and through imaging the fouling pattern on the membrane surface. The fouling pattern obtained from the experiments and the fouling pattern produced through CFD modeling were compared to verify the accuracy of the CFD models. Compared to the first section, the CFD models in the second section

simulated various time points over a range of time instead of only one steady state point. In order to reduce the computational burden, it was assumed that the foulant formed a single layer on the membrane surface and flux decline caused by the single layer foulant was neglected. The results showed that the CFD modeling could predict the fouling pattern on the membrane surface. Compared to mesh spacers, sinusoidal spacers could reduce the flux decline caused by humic acid membrane fouling.

The last section focuses on the impact of spacers in ODMPs. Compared to the CFD models for RO, the CFD models for ODMPs were comprised of three domains instead of one and the structure of the porous support layer of the membrane was considered in the model. With the additional domains and complexity of material transfer through the membrane the ODMP models were less stable and required more computational resources than the RO models. Thus for the bulk of the work it was necessary to use 2D simulations rather than 3D simulations for ODMPs. A few 3D simulations were successfully run in order to provide additional insight. The accuracy of the CFD models was verified by comparing the permeate flux in empty FO and PRO membrane channels obtained from experimental results in literature with the 2D CFD models. After verification another series of 2D CFD models were run to study the effect of spacers on hydrodynamics and mass transfer inside the membrane channel. A 3D model which studied only one unit of a mesh spacer was built to compare and verify the 2D CFD results. The results showed that (i) the permeate flux from CFD modeling from both FO and PRO matched well with the experimental results. (ii) The presence of spacers did not enhance the permeate flux significantly; however, the arrangement of spacer filaments

played an important role in the hydrodynamics. In addition, the results from the 3D models and 2D models were very similar, suggesting that 2D modeling was generally accurate. The 3D model did provide additional insight in showing more details of the hydrodynamics, which are not fully captured in 2D.

This study provides information on how to visualize and predict the mass transfer and hydrodynamics of RO and ODMPs which will benefit the future membrane research on the performance of RO and ODMPs. The investigation of building unobstructed membrane channels such as sinusoidal membrane channels will be helpful for novel membrane spacer designs.

DEDICATION

I would like to dedicate this thesis to my parents,
Qingyun Huang and Fushan Xie
all my relatives and friends to whom I am deeply in debt

ACKNOWLEDGMENTS

I would like to thank my advisor Dr. David A. Ladner for taking me as one of his first students and over the years he has been teaching me, nurturing me and encouraging me. This would not be accomplished without his vision, support and guidance. I would also like to thank Dr. Larry Murdoch, Dr. Tanju Karanfil and Dr. Scott Husson for devoting time to serve in my research committee. I would like to thank my parents Qingyun Huang and Fushan Xie, my brother Pei Xie and all my relatives and friends for their unconditional and unceasingly love and support.

I would like to thank Dr. Murdoch for teaching me CFD simulation with Comsol Multiphysics, Mr. Timothy Pruett for helping me making sinusoidal spacers with 3D printing, the students in the Creative Inquiry program for setting up the bench scale RO system. Also I would like to thank everyone in Dr. Ladner's research group for their love and support.

Principal funding support for this work was provided by the Department of Environmental Engineering and Earth Sciences at Clemson University. Partial funding was also obtained from National Science Foundation projects CBET #1534304 and CBET #1236070. Clemson University is acknowledged for generous allotment of computational time on the Palmetto Cluster.

TABLE OF CONTENTS

	Page
TITLE PAGE	i
ABSTRACT.....	ii
DEDICATION	vi
ACKNOWLEDGMENTS	vii
TABLE OF CONTENTS.....	viii
LIST OF TABLES	x
LIST OF FIGURES	xi
LIST OF SYMBOLS	xvii
LIST OF ACRONYMS	xx
I. INTRODUCTION AND LITERATURE REVIEW	1
CFD Modeling for Membrane Filtration.....	2
Sinusoidal Spacers on Concentration Polarization Mitigation in RO	5
Membrane Fouling and Spacers in RO	7
Osmotically Driven Membrane Process Modeling	9
II. RESEARCH OBJECTIVES	13
CFD Modeling and Experimentation Evaluation for Concentration Polarization Mitigation with Sinusoidal Spacers	13
Experimental and CFD Modeling Evaluation for Membrane Fouling Mitigation.....	13
Osmotically Driven Membrane Process Modeling	13
III. HYDRODYNAMICS OF SINUSOIDAL SPACERS FOR IMPROVED REVERSE OSMOSIS PERFORMANCE	15
Materials and Methods	15
Results and Discussion.....	25

Table of Contents (Continued)

	Page
Conclusions	34
IV. MITIGATING MEMBRANE FOULING WITH SINUSOIDAL SPACERS.....	35
Materials and Methods	35
Theoretical Equations	37
Results and Discussion.....	39
Conclusion.....	48
V. COMPUTATIONAL MODELING OF FLUID FLOW AND MASS TRANSPORT IN FORWARD OSMOSIS AND PRESSURE RETARDED OSMOSIS	49
Materials and Methods	49
Results and Discussion.....	59
Conclusion.....	77
VI. CONCLUSION AND RECOMMENDATIONS	80
Conclusions	80
Recommendations for Future research.....	83
APPENDICES	84
A: The Mesh Scheme and Quality Sensitivity Test of CFD models.....	85
B: CFD Modeling on the Individual Impact of Spacers on the Feed and Draw Side of FO Membrane Channels	88
C: Models for Dissertation.....	91

LIST OF TABLES

Table	Page
Table 5-1. Boundary settings for FO and PRO simulations. The location of each boundary is	52
Table 5-2. Summary of difference of permeate flux between simulation and literature data. In scenario #1, the feed solution concentration is 0 M and the draw solution concentration is 1 M, while in #2 the feed concentration is 0.5 M and the draw solution concentration is 1.5 M.....	61
Table 5-3. Standard deviations of water flux (LMH) in the literature data.....	61

LIST OF FIGURES

Figure	Page
Figure 3-1 Geometries of sinusoidal channels. The overall length of each channel is 130 mm. The cross-sectional view (bottom) applies to all geometries.....	16
Figure 3-2. Oblique view of a representative sinusoidal spacer built for experiments. This spacer has the $3\sin(\pi/12)$ geometry.....	17
Figure 3-3. Plan and section views of a representative sinusoidal spacer. As with Fig. 1, this spacer has the $3\sin(\pi/12)$ geometry. Blue arrows indicate the water flow path. Dimensions are in mm.	17
Figure 3-4 The mesh scheme of the sinusoidal spacer $6\sin(\pi/6)$. In order to capture the concentration gradient near the membrane surface, additional boundary layer mesh was employed near the membrane surface.	19
Figure 3-6. Bench-scale RO membrane test setup. Square symbols stand for controls (V for needle valve actuator voltage and of for the feed flow rate control). Diamond symbols stand for the data acquisition (Cf for feed concentration, Mp for permeate mass, Cp for permeate).....	23
Figure 3-7. Velocity magnitudes (color flood, m/s) for the five channel geometries. Simulations shown here used a pressure of 6900 kPa and NaCl concentration of 0.6 M. At left are the plan views showing one or two wavelengths of each channel, taken at a depth of 0.75 mm. The other three views show the velocity in transverse sections located at the (a) peak, (b) middle, and (c) valley of the sinusoidal channel. The measurement under each section indicates distance from the entrance.	26
Figure 3-8. Concentration profiles for the channels (color flood, M). Simulations shown here used a pressure of 6900 kPa and NaCl concentration of 0.6 M. At left are the plan views showing one or two wavelengths of each channel, taken at the membrane surface. The other three views show the concentration in transverse sections located at the (a) peak, (b) middle, and (c) valley of the sinusoidal channel. The	

measurement under each section indicates distance from the entrance. To better illustrate the CP, all the section views were extended 4 times in the x direction and only the quarter of the total channel next to the membrane is shown, with a jagged line indicating the break opposite the membrane.....	28
Figure 3-9. CP factors for different conditions in the numerical simulations	29
Figure 3-10. Flux data for different conditions in the numerical simulations.....	30
Figure 3-11. Flux data from experiments. Data are based on the average of triplicate tests. Error bars represent the standard deviation.....	31
Figure 3-12. Comparison between flux values for simulations and experiments. All working conditions (pressure and NaCl concentrations) are represented. Error bars show the standard deviation for triplicate experiments.....	32
Figure 3-13. Pressure gradient obtained from simulations for various channels. The mesh spacer data point is highlighted in red for quick comparison to this conventional condition.....	33
Figure 4-1. DI water flux compared with final flux from the experiments. Data are based on the average of triplicate tests. Error bars represent the standard deviation.	40
Figure 4-2. Flux decline percentage vs the pressure drop from all the spacers under cross flow velocity 0.15 m/s and applied pressure 600 psi.....	41
Figure 4-3. Simulation results of total mass of foulant adsorbed onto membrane surface over time from different spacers when the asoprtion equation did not consider the impact of shear stress. The cross flow velocity was 0.15 m/s and applied pressure was 600 psi.	42
Figure 4-4. Simulation results of total mass of foulant adsorbed onto membrane surface over time from different spacers when the asoprtion equation considered the impact of shear stress. The cross flow velocity was 0.15 m/s and applied pressure was 600 psi.	43

Figure 4-5. Simulation results of total mass of foulant adsorbed onto membrane surface over time from different spacers with shear stress under equal pressure drop condition.....	44
Figure 4-6. Energy consumption per unit volume of permeate production under equal pressure drop scenario with 0.001M sodium chloride solution.....	45
Figure 4-7. Comparison between fouled membrane images for simulations and experiments. The whole membrane coupon with spacer wall is shown at left; the zoomed view of membrane coupon is in the middle; the fouling distribution ($\mu\text{g}/\text{cm}^2$) on the membrane surface at $t=40000\text{s}$ from the simulation that included shear stress is shown at right.	47
Figure 5-1. Osmotic driven membrane channel domains for two configurations: (left) FO mode in which the active layer (indicated by the bold vertical line) faces the feed-side; (right) PRO mode in which the active layer faces the draw channel. The porous support layer is denoted by the grey area. Inflow of water and salt concentration in feed and draw are denoted by uf , ud , cf and cd respectively. Fluxes of water and salt are denoted by J_w and J_s , respectively. The boundaries are numbered 1–8.....	52
Figure 5-2 The mesh scheme (229,486 mesh elements) for 2D model of an empty membrane channel. The detailed mesh shape and distribution are presented in the two lower figures. The units of all axes are mm. In this model the TFC membrane (40 μm support layer thickness) is shown.....	54
Figure 5-3. 3D illustration of mesh spacer (left). Dash line indicates the location of the 2D model (a, top right). Dash lined square indicates the location of the 3D model (b, bottom right).....	55
Figure 5-4. The location of periodic boundaries (marked in purple).....	57
Figure 5-5 The mesh scheme (328528 mesh elements) for 2D spacer-filled FO model with 0.01 mm membrane to filament distance. The detailed mesh shape and distribution are presented in the lower two figures. The units of all axes are mm. In this model the HTI membrane (100 μm support layer thickness) is shown.	58

Figure 5-6 The mesh scheme (1536220 mesh elements) for 3D spacer-filled FO model with 0.01 mm membrane to filament distance.	59
Figure 5-7. Water flux (LMH) from simulation and literature.	60
Figure 5-8. Permeate flux from empty and spacer-filled channels with CC = 6 mm and 12 mm.	63
Figure 5-9. Water fluxes under different velocities along the membrane surface from the empty membrane channel and the spacer-filled membrane channels with CC = 6 mm and 12 mm and 0.01 mm distance between the membrane and spacer filaments. The first and last 1 mm of the channel were excluded to remove entrance and exit effects. The sketch of the part of the channel whose data was presented was placed on top of the corresponding plot to illustrate the location of the spacer inside the membrane channel.	64
Figure 5-10. Concentration profile (indicated by the color flood) and velocity profile (indicated by the arrows) under different inlet velocities of spacer-filled membrane channel with CC = 6 mm. The size of the arrows is proportional to the logarithmic value of the velocity in order to better show vortices. These data were from the section whose distance to the entrance was approximately 14.5 to 20.5 mm.	65
Figure 5-11. Illustration of (a) the empty channel and spacer-filled membrane channels with different membrane-filament distances (b) 0, (c) 0.01, (d) 0.05, (e) 0.1, (f) 0.15, and (g) 0.25 mm.	67
Figure 5-12. Permeate flux with different membrane-filament distances.	69
Figure 5-13. Water fluxes under different velocities along the membrane surface from the empty membrane channel and the spacer-filled membrane channels with various membrane-filament distances. The first and last 1 mm of the channel were excluded in order to remove entrance and exit effects. The sketch of the part of the channel whose data was presented was placed above the corresponding plot to illustrate the location of the spacer inside the membrane channel.	70
Figure 5-14. Concentration profile (indicated by the color flood) and velocity profile (indicated by the arrows) under different	

	inlet velocities and membrane-filament distances for spacer-filled membrane channels with CC = 6 mm. The size of the arrows is proportional to the logarithmic value of the velocity in order to better show the vortices. These data were from the section whose distance to the entrance was approximately 14.5 to 20.5 mm.	72
Figure 5-15.	Two series of cross sectional slices selected from 3D modeling. On the left is the section perpendicular to the flow direction and on the right is the section parallel to the flow direction. The sections from both directions included (a) one center section, (b) one section between the center and boundary section and (c) one boundary section.	73
Figure 5-16.	Concentration profile (indicated by the color flood) and velocity profile (indicated by the arrows) in the sections of the 3D model corresponding to Fig. 12. Velocity was 0.01 m/s. For each cross section, the size of the arrows is proportional to the value of the velocity.	74
Figure 5-17.	Concentration profile (indicated by the color flood) and velocity profile (indicated by the arrows) in (a) the middle section of the 3D model and (b) the section from the 2D model where the distance to the entrance was from 9.5 mm to 14.5 mm. The size of the arrows is proportional to the value of the velocity.	75
Figure 5-18.	Velocity profiles inside 3D spacer-filled channels. The flow path is indicated by the streamline and the local velocity value is indicated by the color. Two inlet flow rates were tested: (a) $6 \times 10^{-7} \text{ m}^3/\text{s}$ (corresponding to inlet velocity 0.01 m/s) and (b) $9 \times 10^{-6} \text{ m}^3/\text{s}$ (corresponding to inlet velocity 0.15 m/s). For each flow rate, an orthogonal view (left) and top view (right) are provided.	76
A-1.	Pressure drop and permeate flux under different mesh qualities in sinusoidal spacer $6\sin(\pi/6)$	87
B-1.	Illustration of the spacer configurations. (a) the spacer only existed in the feed side; (b) the spacer only existed in the draw side; (c) the spacer existed in both feed and draw side. The filament to membrane distance is 0 mm and the CC distance is 12 mm.	89

B-2. Illustration of the spacer configurations. (a) CC distance is 12 mm (b) CC distance is 8 mm; (c) CC distance is 5 mm. The filament to membrane distance is 0 mm and the spacer existed in both the feed and draw side.	89
B-3. Permeate flux from membrane channels with different flow velocity, CC distance and spacer configuration.	90

LIST OF SYMBOLS

Latin Letters

A	Hydraulic permeability of the membrane, $\text{m}/(\text{s}\cdot\text{Pa})$
a_{osm}	Osmotic pressure coefficient, $\text{Pa}\cdot\text{m}^3/\text{mol}$
B	Salt permeability of the membrane, $1/\text{s}$
c	Concentration in the channel, M
c_d	Inflow salt concentration at the draw side, M
c_f	Inflow salt concentration at the feed side, M
c_{in}	Inlet concentration, M
c_w	Concentration near the membrane, M
c_{sw}	Foulant concentration near the membrane, M
c_s	Foulant concentration being adsorbed to the membrane, mg/m^2
c_{se}	Equilibrium foulant concentration that can be adsorbed to the membrane, mg/m^2
D	Diffusion coefficient in the bulk, m^2/s
D_e	Effective diffusion coefficient in the membrane support layer, m^2/s
h	The mesh element size, mm
J_{DI}	Averaged flux during the DI water run during fouling experiments, LMH
J_f	Averaged flux at the end of fouling experiment, LMH
J_w	Flux of permeate, m/s
J_s	Flux of salt through the membrane for ODMPs, $\text{M}\cdot\text{m}/\text{s}$
k_l	Adsorption coefficient, $1/\text{s}$

k_2	Desorption coefficient
L	Length of the channel, mm
n	Normal direction of boundary
p	Pressure in the channel, kPa
p_{out}	Pressure at the outlet, kPa
Δp	Pressure difference across the membrane, kPa
R	Salt rejection ratio
u	Velocity magnitude, m/s;
u_{in}	Inlet velocity, m/s
u_d	Inflow velocity at the draw side, m/s
u_f	Inflow velocity at the feed side, m/s

Greek Letters

α	Flux decline ratio
β_F	Forchheimer coefficient
ε	Porosity of the membrane support layer
κ	Hydraulic conductivity, m/s
γ	Shear rate, 1/s
μ	Dynamics viscosity, Pa·s
$\Delta\pi$	Osmotic pressure difference between two sides of the membrane, Pa
π_d	Osmotic pressure at the draw side near the active layer of the membrane, Pa
π_f	Osmotic pressure at the feed side near the active layer of the membrane, Pa

ρ	Density of water, kg/m ³
τ	Shear stress, Pa
τ_m	Tortuosity of the membrane support layer

LIST OF ACRONYMS

CC	Center to center
CFD	Computational fluid dynamics
CP	Concentration polarization
ECP	External concentration polarization
FO	Forward osmosis
HPC	High-performance computing
ICP	Internal concentration polarization
ODMPs	Osmotically driven membrane processes
PRO	Pressure retarded osmosis
RO	Reverse osmosis

CHAPTER ONE

INTRODUCTION AND LITERATURE REVIEW

Reverse osmosis (RO) and osmotically driven membrane processes (ODMPs) are widely used membrane techniques. RO is a pressure driven membrane process which requires intensive external energy input to overcome the osmotic pressure difference to draw solvent through the membrane. It is widely used for producing high purity water because of its ability to reject most dissolved and suspended materials [1–3]. ODMPs can utilize an osmotic pressure difference to draw solvent through a semipermeable membrane [4–6]. Forward osmosis (FO) and pressure retarded osmosis (PRO) are the two operational modes for OMDPs [7,8] where in FO mode the active layer of membrane faces the feed solution and in PRO mode the active layer faces the draw solution [9,10]. ODMPs have gained considerable attention due to the capacity of energy production with PRO [11–13] and waste water purification and desalination with FO [14–17].

Two major problems associated with RO and ODMPs are membrane fouling and concentration polarization (CP), because they reduce the quality and quantity of the product water and increase the operational cost [1,3,4,18]. Many studies have shown that hydrodynamics inside membrane channels play an important role in CP and membrane fouling reduction [19–21]. Spacers are used in the membrane module to separate the membrane sheets and form flow channels. Spacers are able to increase the local fluid velocity and shear rate, thus enhancing the mass transfer of salts and foulants away from the membrane surface, which can reduce CP and membrane fouling [3,5,22–24]. Many

studies have reported that spacer design is critical in increasing the efficiency (reducing CP, fouling and pressure drop) of RO and ODMPs [11,19,25–27].

There are two important criteria when it comes to spacer design evaluation: (i) mass transfer efficiency and (ii) energy efficiency. While the energy consumption can be reflected in pressure drop per unit flow, the mass transfer efficiency in this study was reflected in the reduction of CP, which is challenging for measuring and direct observation from experiments. The visualization of the flow and mass transfer inside membrane channels has been greatly empowered by the advent of computational fluid dynamics (CFD) models; however, experimental studies are still important to verify the results from simulation. This work combines both experimental work and CFD simulations to investigate and improve the hydrodynamic conditions for RO and ODMPs.

CFD Modeling for Membrane Filtration

Observing and quantifying the flow and solute transfer within the membrane system, especially the concentration near the membrane surface, is difficult via experiments, thus analytical and numerical CFD solutions have been used to study the hydrodynamics. Early analytical and numerical solutions were not able to tackle spacer-filled membrane channels because it was hard to build such complicated geometry in the model and they needed to employ simplified or predefined velocity profiles [28–30]. Many later studies [20,21,31] have reported that spacers played an important role in defining velocity and concentration distribution inside membrane channels, so the early models without spacers were limited in their applicability.

Another simplification in early CFD modeling was that the permeate flow through the membrane (flux) was often ignored or set as a fixed number. By doing so, the interaction between the fluid flow and solute transport was ignored. This meant the models were unable to evaluate an important characteristic of membrane filtration and CP.

Recently, an increasing number of numerical models using CFD software have been reported [32–37]. The advantage of CFD software is that it can tackle complicated geometry such as 2D and 3D spacer-filled membrane channels [38–40]. For CFD, the biggest challenge is the necessity of a large computation capacity because the CP layer is thin, usually on the order of 10^{-3} mm, with a steep gradient profile, which requires a fine mesh near the membrane layer [26,41]. The use of finer mesh will increase the demand for memory and running time. In order to reduce the computational burden, many researchers have tried to simplify the numerical model, such as simplifying the geometry by transforming 3D to 2D [26,31,42], assuming the flux is independent of the concentration on the membrane surface by assigning a constant flux or fixed membrane surface concentration in the model [43,44], or even just neglecting the flux and only studying the shear rate and flow velocity distribution in membrane channels [25,45,46]. Even though using 2D models to represent 3D conditions would decrease the accuracy of the simulation, especially when the geometry or the flow path was asymmetrical [32,36,47], it was a necessary compromise when the computational capacity was unable to meet the requirement of 3D models. Therefore, if computational capacity allows, 3D CFD models are the best option for membrane filtration studies for both RO and ODMFs.

In this study 3D CFD models were used for the investigation of sinusoidal spacers' performance on seawater desalination and humic acid membrane fouling. On the contrary, 2D models were used for ODMP simulations of empty membrane channels and spacer-filled membrane channels, because the geometry and physics in ODMPs are more complicated than RO and required more computational power. The results of the full size 2D models and small size 3D models were compared in order to verify this simplification. The detailed explanation of the geometry and model setup is available in the ensuing sections and chapters for ODMPs.

Models were developed to calculate the permeate flux based on the concentration near the membrane surface instead of assigning a constant value, where the flow and mass transfer inside the RO and ODMP membrane channels can be described by coupling Navier-Stokes equations for the flow (Equations (1) and (2)) and the convection-diffusion equation for the mass transport (Equation (3)):

$$\nabla \cdot \mathbf{u} = 0 \quad (1)$$

$$\rho \mathbf{u} \nabla \cdot \mathbf{u} = \nabla \cdot [-P + \mu(\nabla \mathbf{u} + (\nabla \mathbf{u})^T)] \quad (2)$$

$$\nabla \cdot c = D \nabla^2 c \quad (3)$$

where \mathbf{u} is fluid velocity, ρ is density, P is pressure, μ is dynamic viscosity, c is concentration, and D is the diffusion coefficient. These models are fully coupled, in the sense that all equations are solved simultaneously, rather than solving the fluid flow equations first then solving the solute transport equations afterward.

The permeate flux through the membrane was determined by the irreversible thermodynamics model derived by Kedem and Kachalski [38]:

$$u_m = A \cdot (\Delta p - a_{osm} \cdot \Delta c) \quad (4)$$

Where u_m is the permeate flux, A is the membrane permeability, Δp is the difference between the applied pressure from both sides of the membrane, and a_{osm} is osmotic coefficient, $a_{osm} \cdot \Delta c$ is the difference in osmotic pressure between the feed and permeate sides of the membrane.

Sinusoidal Spacers on Concentration Polarization Mitigation in RO

CP generally refers to the phenomenon where the rejected solutes accumulate near the membrane causing the local concentration to be higher than the bulk flow [25,31]. CP diminishes the permeate quality, decreases flux, and can result in membrane fouling via precipitation and cake formation on the membrane surface [18,48–51]. Since CP has such an adverse impact on membrane filtration, understanding and being able to predict CP is important for RO module design [52,53].

Attempts to understand and measure CP date back as early as the 1960s [9,18,26,39,54,55]. Investigating and observing CP is a challenging task because the CP layer is thin and it occurs inside a membrane module where it is difficult to insert sensors and instrumentation for measurement. Early experimental work successfully demonstrated the adverse effect of CP, but was unable to quantify it [54,56]. With the advent of CFD modeling, researchers were able to use CFD models to better visualize the details of hydrodynamics and solute transport.

In order to reduce CP in a membrane channel, spacers have been used to increase the mass transfer. The mesh geometry spacer is the most common type used in currently marketed spiral-wound RO modules [20,57,58]. There are a plethora of studies showing that spacers can effectively decrease CP; however, the main problem associated with mesh spacers is that even though they can decrease CP, the presence of the spacer incurs higher pressure drop [19,31,36]. The spacers also create areas of stagnant flow, or dead zones, and entrapment sites where foulants can accumulate [42]. While a great deal of work in recent years has focused on membrane surface modification to make anti-fouling or foulant-resistant membranes [59–61], the benefits of those surface modifications may be diminished if spacer design is not properly addressed.

The reported efforts to optimize the thickness, angle and material of the mesh spacer to increase permeate flux and reduce fouling were mainly done via CFD modeling with or without experimental verification [25,45,46,62]. The drawback to those aforementioned designs was their success at mitigating CP and improving flux came at the cost of higher energy consumption; spacers disrupt the flow path, increasing the hydrodynamic resistance and longitudinal pressure drop [19,25,31,46,63,64].

In the present study we have combined both computational and experimental approaches to demonstrate the utility of a novel spacer with sinusoidal geometry. Sinusoidal channels have been used in apparatuses like heat exchangers to achieve considerable mass and heat transfer enhancement at low pressure drop [33,34]. Nishimura et al. [35-37] performed a series of experiments regarding flow characteristics and mass transfer in sinusoidal wavy channels, where the channels were able to generate

vortices both in transverse and longitudinal directions; e.g. 3D flow. The vortices disrupted the flow pattern, thus increasing mass transfer. Here we show that sinusoidal flow can similarly enhance mass transfer in RO, increasing flux with the same or lower energy requirements as conventional mesh spacers. To our knowledge the use of sinusoidal channels in RO applications has not yet been reported

Membrane Fouling and Spacers in RO

Membrane fouling, which generally refers to the attachment, accumulation and adsorption of foreign material on a membrane surface or within membrane pores, is a critical issue in membrane filtration [59,65–70]. Fouling will result in higher operational cost, shorter membrane lifespan, and less desirable permeate quality [59,65–69,71–73]. Studies on membrane fouling patterns often suggest that feed spacers play an important role in fouling development. Tran et al. [74] reported that fouling initially started along the feed spacer and then gradually encroached upon the rest of the clean membrane area. Gimmelshitein et al [75] studied the flow in spacer-filled channels and found that the spacer exacerbated the particle deposition on places near the mesh spacer filaments. Vrouwenvelder et al. [59] and Paassen et al. [72] studied the correlation between spacers and biofouling. They reported that biofouling was largely initiated on feed spacers and the pressure drop caused by biomass accumulation was much higher when the spacer was present.

It was demonstrated in our study that sinusoidal spacers had the potential to produce more permeate with lower pressure drop during seawater desalination because of a reduction in CP [36]. That work dealt only with non-adsorbing salts. In this study we add

adsorptive fouling into our experimental and modeling matrix to further evaluate the potential of these sinusoidal spacers.

Both bench-scale experiments and 3D CFD models were employed in this study. As mentioned previously, CFD is a widely used technology when it comes to spacer design [2,21,26,27,31,45–47]. A plethora studies of using 2D [27,31,39,42,55] or 3D [20,21,25,76,77] CFD models to investigate and improve membrane spacers is available in the literature. In many cases (such as the present work) the goal of new spacer design is to reduce fouling. Humic acid, which was used as a model foulant in this study acid, is a natural organic matter (NOM) which can be found in lakes, rivers and reservoirs and it is considered as a major foulant during membrane processes [78]. It is usually recommended that humic acid be removed as well as possible in pretreatment before RO [79]. Humic acid can form brownish gel-like chelates with multivalent ions on membrane surfaces [80,81]. Calcium-humate can cause significant irreversible flux decline [82], though solution chemistry is important in determining the magnitude of humic acid adsorption during membrane filtration [83,84].

Analysis of adsorptive membrane fouling is challenging because both the hydrodynamic (i.e. velocity, CP) and thermodynamic (i.e. humic acid-membrane interactions) conditions need to be considered. The Langmuir model is often used in predicting humic acid adsorption during membrane filtration [83–85], which is a good model to start with when dealing with adsorption [79], but hydrodynamics need to be considered in order to simulate adsorptive fouling on RO membranes in crossflow mode. Most current mathematical models are empirical [84,86,87] and do not fully consider

hydrodynamics. In this study, simulations investigate the influence of both thermodynamics and hydrodynamics on adsorptive membrane fouling in a crossflow environment when different spacers are used.

Osmotically Driven Membrane Process Modeling

The study of ODMPs has distinct differences compared to more conventional and well-understood pressure driven membrane processes, such as reverse osmosis (RO). In RO CP almost exclusively exists in the feed channel near the active side of the membrane [80,88]; however, in FO and PRO there exist two types of CP: one is in the channels near the vicinity of the membrane and is known as external concentration polarization (ECP), while the other is within the membrane support layer and is known as internal CP (ICP) [89,90]. While ECP could be effectively reduced by increasing flow velocity, this method is less effective for ICP [5,91] and ICP has become the primary hindrance for improving the water flux in FO [9,92]. Many studies have confirmed that ICP could be reduced by making the membrane thinner and more permeable [7,23,88,93,94]; however, breakthroughs in these material developments is time consuming and difficult.

One potential alternative for improving hydrodynamics and mass transport is to apply a feed spacer in ODMPs. The available reports of reducing CP with spacers is relatively lacking compared to the plethora of studies available for spacers in RO systems [6,95]. One possible reason for the relatively low interest in spacers was suggested by Park et al. [6] (when discussing FO): compared to spiral wound modules, it is currently believed that hollow fiber configurations are more suitable, which do not require a feed spacer. It is possible, however, that future developments could result in different designs

such as spiral wound modules (or other configurations) that are more economical and feasible for ODMPs, as occurred in the developmental history of RO. The knowledge of feed spacer impacts on ODMPs could be beneficial to further such development.

Some experimental efforts have been made to study the feed spacer impact on FO. Zou et al found that using a spacer in the feed side not only reduced the ECP but also lowered the fouling propensity [51]. Linares et al. [95] found that using thicker feed spacers could reduce flux decline caused by biofouling in FO. Zhang et al. [91] reported placing the feed spacer in the draw channel to contact with the membrane while the feed spacer in the feed channel far away from the membrane could enhance flux for FO. However, their spacer thickness (0.8 mm) was a lot smaller than the channel height (3.5 mm) which would not be possible in practice (such as in a spiral wound module) where the spacer holds the membrane leaves apart and thus the channel height is about the same as the spacer thickness. Similar to the RO studies described previously, these experimental results are useful, but it is difficult to experimentally observe and quantify the hydraulic and mass transfer conditions inside the system at the high spatial resolution required to understand CP. Computational methods are one way to make progress in this regard.

CFD is useful in studying FO and PRO because not only can it calculate and visualize the fluid flow inside the membrane channel, but also inside the membrane support layer which is different from RO simulation [20,23,34,35,38,46,94]. Extending CFD models by including solute transport enables us to also study mass transfer. Sagiv et al. [89] developed a 2D finite element method (FEM) model to study FO with several

different types and concentrations of draw solutions. McCutcheon et al. [5] developed a 2D analytical model to study the coupled effects of internal and external CP on permeate flux. Gruber et al. [33] built a 3D CFD model to study the FO process and optimize the module design. Similar to the ODMP experimental work discussed above, all of these computational studies simulated modules without spacers; CFD studies of ODMPs with spacers is very limited. The only literature found in our search was by Park et al. [6]. They studied the impact of spacer configuration on CP in FO and PRO in a 2D simulation by combining both external and internal concentration into a single parameter. They reported that the spacer could mitigate CP in both PRO and FO; however, the benefit of using spacers may be diminished because local water flux is blocked where the spacer touches the membrane [6]. Such a 2D model is very useful, but 2D simulations are not able to fully investigate the effects of flow angle and spacer orientation [6,16,24,32]; 3D models could be helpful for investigations of those aspects. The challenge to 3D simulations of spacer-filled FO and PRO models is that they require much more computational power and time. Prior to this study, no publication was available on 3D simulation of spacer-filled FO channels and the only 3D CFD model on empty FO that could be found was reported by Gruber et al. [33] in which they verified the flux results from simulation with experimental results and found that the analytical modeling approach would severely underestimate the ECP.

In this study a series of models were built to predict permeate flux. The simulation results of empty-channel (with no feed spacer) membrane cells were verified by comparison with experimental results from the literature. Then both 2D and 3D

spacer-filled FO models were built to investigate the impact of the feed spacer on hydrodynamics and mass transfer inside the membrane channel. The study also evaluates the degree to which feed spacers can potentially enhance permeate flux.

CHAPTER TWO

RESEARCH OBJECTIVES

CFD Modeling and Experimentation Evaluation for Concentration Polarization Mitigation with Sinusoidal Spacers

The first research motivation arose from a desire to design novel spacers for RO that could reduce CP with lower energy input than conventional mesh RO spacers. The specific objective was to develop CFD models that accurately simulated the hydrodynamics and mass transfer. This required a robust set of equations that could predict the permeate flux through the membrane, taking into account local osmotic pressure. Experiments were performed to validate the models and verify the performance of the sinusoidal spacers.

Experimental and CFD Modeling Evaluation for Membrane Fouling Mitigation

The second objective was to test and compare the performance of different sinusoidal spacers on adsorptive membrane fouling mitigation. CFD models were developed that could predict the foulant pattern on the membrane surface. The models were validated with a set of experiments using humic acid as a foulant material.

Osmotically Driven Membrane Process Modeling

The third objective was to investigate the impact of spacers in ODMPs. A key part of this objective was to develop CFD models that could simulate both feed and draw solution channels and predict flux based on osmotic gradients. An initial sub-objective was to validate the models using literature data, which did not incorporate spacers. The

final sub-objective was to extend the models to evaluate spacer-filled channels under different crossflow velocities and spacer configurations.

CHAPTER THREE

HYDRODYNAMICS OF SINUSOIDAL SPACERS FOR IMPROVED REVERSE OSMOSIS PERFORMANCE

Materials and Methods

Design and Manufacture of Sinusoidal Spacers

Five models of RO spacer channels were designed and built (Fig 2-1). The channels included four sinusoidal patterns with wall geometry described by Equation (5)

$$y = a \sin\left(\frac{2\pi x}{L}\right) \quad (5)$$

where a is the amplitude and L is the wavelength. a was either 3 or 6 mm, and L was either 12 or 24 mm. The cross-sectional geometry of the channel was a 1.5 mm by 6 mm rectangle, with the membrane lying along one of the 6 mm sides. A straight channel was also modeled, representing the non-sinusoidal control. For clarity, the channel geometries will be referred to as $3\sin(\pi/12)$, $3\sin(\pi/6)$, $6\sin(\pi/12)$, $6\sin(\pi/6)$, and straight channel.

The spacers for CP reduction study were built via milling machine with plastic ($6\sin(\pi/6)$ and straight) and brass ($3\sin(\pi/12)$) and the spacers for membrane fouling include all aforementioned designs and were built by 3D printing technology with the Clearvero material. A 3D rendering of one sinusoidal spacer is shown in Fig. 3-2 and the detailed drawing with dimensions is depicted in Fig. 3-3 where fluid flow directions are also indicated.

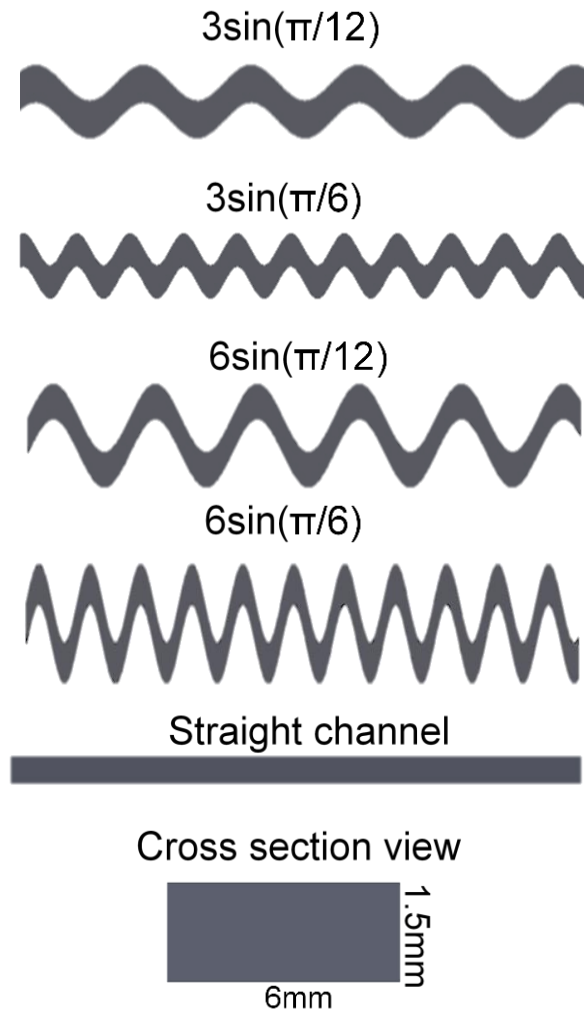


Figure 3-1 Geometries of sinusoidal channels. The overall length of each channel is 130 mm. The cross-sectional view (bottom) applies to all geometries

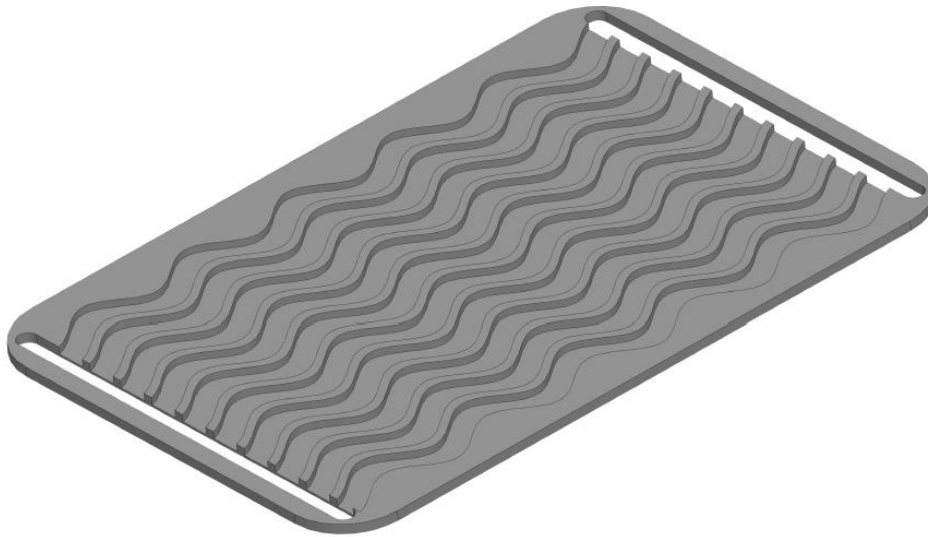


Figure 3-2. Oblique view of a representative sinusoidal spacer built for experiments. This spacer has the $3\sin(\pi/12)$ geometry.

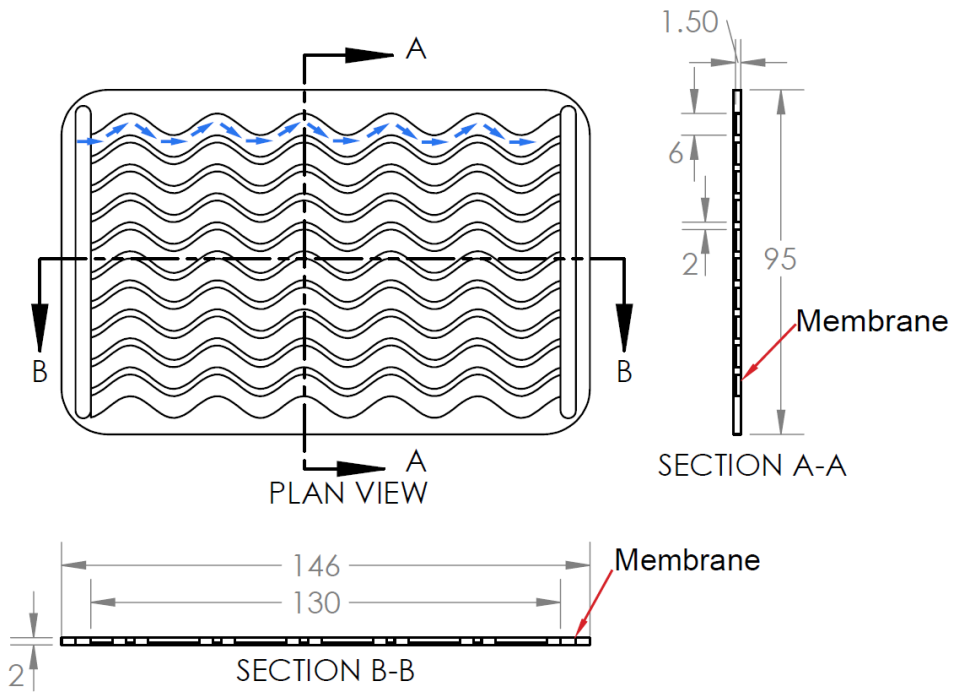


Figure 3-3. Plan and section views of a representative sinusoidal spacer. As with Fig. 1, this spacer has the $3\sin(\pi/12)$ geometry. Blue arrows indicate the water flow path. Dimensions are in mm.

Model Description

All sinusoidal spacers and a conventional mesh spacer were simulated. The mesh spacer channel had the same dimensions as the straight channel except that it was filled with a mesh spacer with the geometry of the filaments used in experiments. Due to the complexity of the flow field induced by the mesh spacer, the mesh spacer model (unlike the sinusoidal models) neglected the permeate through the membrane, because the volume flux of the permeate was less than 0.6% of the inflow rate ($1.35 \times 10^{-6} \text{ m}^3/\text{s}$); the mesh spacer model was only used to simulate the pressure gradient.

Models were created and solved using Comsol Multiphysics 4.2a. This code used the Galerkin finite element method which converts differential equations in a continuous domain into a discrete problem to solve governing equations over a computational mesh [96–98]. The mesh consisted of tetrahedral elements through the subdomain, with thin rectangular elements at the boundaries. Mesh density was evaluated by comparing results from different meshes. For example, the flux for sinusoidal channel $6\sin(\pi/6)$ with 783,230 elements differed less than 0.9% from the flux with a mesh density that was 12% greater (894,880 elements). This small change in the result (<1%) with a 12% change in mesh density was acceptable, so the mesh with fewer elements was used to decrease the computational intensity. The mesh densities for straight, $3\sin(\pi/12)$, $3\sin(\pi/6)$, $6\sin(\pi/12)$, and $6\sin(\pi/6)$ were 510, 458, 470, 533 and 644 elements per mm^3 and the volume for each channel was 1200 mm^3 . In order to capture the sharp concentration gradient near the membrane surface a layer mesh that consisted of 5 layers was employed near the

membrane in order to capture the gradient for sinusoidal spacers (Fig. 3-4). The reason that layer mesh was chosen was that it is very thin and can be stretched to match the surface geometry. For the rest of the geometry, tetrahedral shape mesh was used (Fig. 3-4).

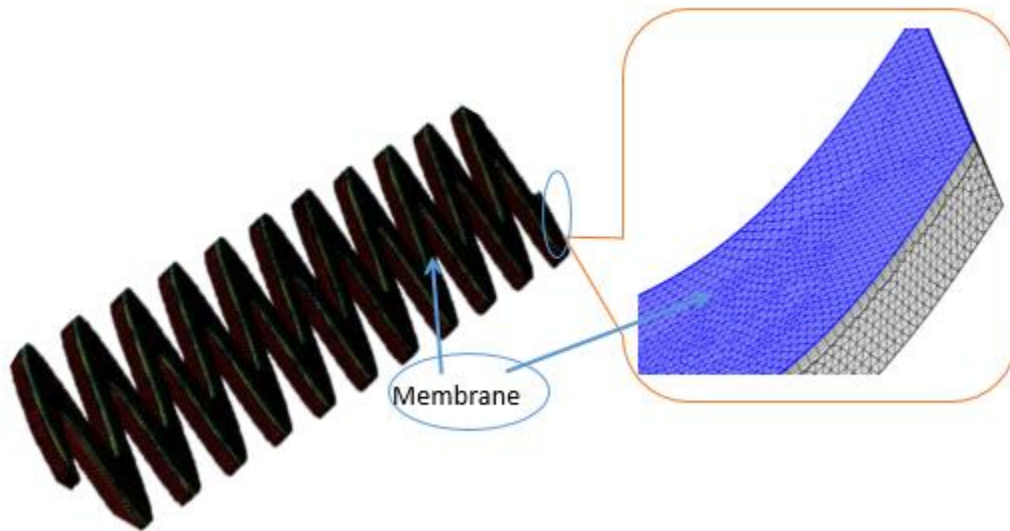


Figure 3-4 The mesh scheme of the sinusoidal spacer $6\sin(\pi/6)$. In order to capture the concentration gradient near the membrane surface, additional boundary layer mesh was employed near the membrane surface.

Fluid flow and transport of sodium chloride (the only solute) inside the channel was described by Equations (1) through (3). The boundary conditions for the inlet were set as follows: inlet velocity (u_{in}) = 0.148 m/s, inlet concentration (c_{in}) = 0.4, 0.5, or 0.6 M NaCl.

At the outlet, the pressure was set to 5500, 6200, or 6900 kPa. Viscous stress and diffusive flux at the outlet were assumed to be negligible. At the impermeable walls, the velocity was set at zero (no slip) and the mass flux of salt normal to the wall was also set

at zero. At the membrane the fluid velocity normal to the wall J_W was coupled to the surface concentration by Eq. 4. This equation is based on the irreversible thermodynamics model derived by Kedem and Kachalski [38] where A (5.24×10^{-12} m/(s·Pa)) is the water permeability of the membrane, which was measured in the experiments, Δp is the applied pressure, and c_w is the salt concentration at the membrane surface. Equation (4) uses a linear dependency of osmotic pressure on salt concentration ($\Delta\pi = a_{osm} \cdot c_w$) with a_{osm} ($4872 \text{ Pa}\cdot\text{m}^3/\text{mol}$) being the osmotic pressure coefficient [25]. Temperature ($T = 293 \text{ K}$), viscosity ($\mu = 0.001 \text{ kg}/(\text{m}\cdot\text{s})$), fluid density ($\rho = 1000 \text{ kg}/\text{m}^3$) and solute diffusivity ($D = 1.5 \times 10^{-9} \text{ m}^2/\text{s}$) were held constant throughout the simulations; though some of these could vary, holding them constant reduces the computational demand and is a sufficiently accurate approximation used by others [29]. In addition, the salt rejection is assumed to be 100% in the model. Actual salt rejection was at least 99% in all experiments, and no correlation was observed between rejection and pressure or between rejection and salt concentration.

As we tested the models, we found that the Péclet numbers in the sinusoidal channels were too high in some models for the simulation to obtain a converged solution. Theoretically, we could make the model converge if the mesh were fine enough; however, even using our maximum computational capacity the model did not converge. We believe this is due to the coupling of flow and solute transport in the membrane channel, as well as through the membrane. Simulations were able to quickly converge when they involved fluid flow only, or when the driving force for permeation depended only on the pressure and was not coupled with the enhanced osmotic pressure caused by

CP. For our fully-coupled, 3D case, we required an adjustment to the model equations, using Comsol’s stabilization technique. The stabilization technique (called “inconsistent stabilization” in Comsol) adds a term $\mu_{art} = \delta_{id} \cdot h \cdot u$ to Equation (2), where μ_{art} represents artificial diffusion, δ_{id} is the scaling factor (set by the user), and h is the mesh element size [98]. The concept of using artificial diffusion is not specific to our application, but is a method that has been employed by others to stabilize transport equations [99]. The resulting equation is:

$$\rho u \frac{\partial u}{\partial t} + \rho u \nabla \cdot u = -P + (\mu + \mu_{art}) \nabla^2 u \quad (6)$$

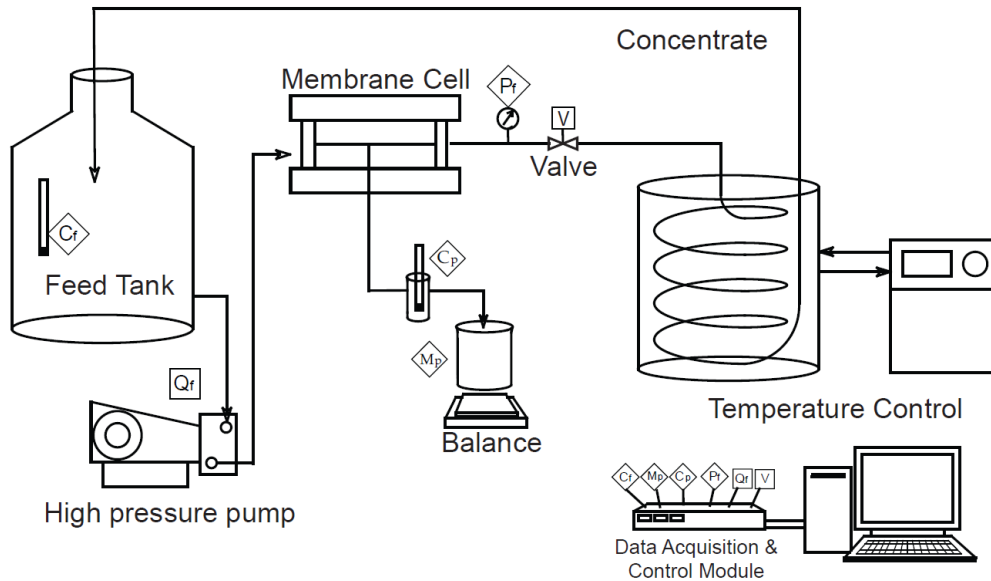
With the new term, the Péclet number expression, originally defined as $Pe = \frac{u \cdot h}{2(\mu)}$ in Comsol, was now expressed as $Pe = \frac{u \cdot h}{2(\mu + \mu_{art})}$. Normally, to ensure that the simulation can obtain a converged solution, the Péclet number should be lower than 1.

We acknowledge here that employing such a method changes the fluid properties from those expected based on first principles, so we ran several simulations to determine the smallest possible number for the scaling factor that would result in a converging solution for all models. The scaling factor of $\delta_{id} = 0.06$ was thus found and used in all models. Fortunately, this was a quite small adjustment and the models that converged with or without the scaling factor gave very similar results. Further, the simulation results were shown to be quite accurate when compared with experimental data (described below), giving further justification for the use of the stabilization technique in these simulations.

Each spacer was modeled using 0.6 M inflow salt concentration under the three inflow pressures (5500, 6200, and 6900 kPa). In addition, three different inflow concentrations (0.4, 0.5 and 0.6 M) were used with the 6900 kPa applied pressure. Simulations were performed on the Palmetto Cluster, Clemson University's primary high-performance computing (HPC) resource. Model runs typically used 40 GB of memory and ran for 20 minutes.

Experimental Setup

Modeling data were validated by experiments performed in a bench-scale RO unit. The spacers used in the experiments were designed to fit within the feed channel of the RO unit and were built by milling sinusoidal or straight channels into brass or plastic blocks. Brass was used initially because it is more rigid and easier to machine, especially for thin (2 mm) parts, such as these spacers. After practice and by using strongly adhering double-sided tape to secure the material, the machinist (in Clemson's Machining and Technical Services) was able to mill the spacers from plastic.



The RO unit (Fig. 3-6) included the following key components: SEPA II

Figure 3-5. Bench-scale RO membrane test setup. Square symbols stand for controls (V for needle valve actuator voltage and of for the feed flow rate control). Diamond symbols stand for the data acquisition (Cf for feed concentration, Mp for permeate mass, Cp for permeate)

membrane test cell (GE Osmonics; now Sterlitech), pump (model 231, Cat Pumps), pressure gauges, balance, temperature probe, conductivity probes (feed and permeate), data acquisition system (SCB-68, National Instruments), tubing, and valves. The pump speed was controlled by a phase inverter (S-11, Toshiba) and the concentrate needle valve position (which regulated the pressure in the membrane cell) was controlled by a valve actuator (MCJ-000AB-3-SS-2MG4, Hanbay Laboratory Automation). Because of the high corrosivity of concentrated salt water, the membrane test cell, tubing ($d= 3/8$ inch) and wetted parts of the pump were made of 316 stainless steel. Tygon tubes were used for the inlet to the pump and outlet of the temperature control heat exchanger. A

heat exchanger consisting of a 3-m-long coiled stainless steel tube and a temperature control unit was used to stabilize the water temperature.

A program written in Labview (National Instruments) was used for RO unit data acquisition and control. Most data were collected continuously (about 100 data points per second) through the data acquisition system and averaged over ten seconds for storage on hard disk. Permeate balance readings were collected through a serial connection once every ten seconds. The Labview program compared pressure readings to a set point and then adjusted the concentrate needle valve actuator as needed to maintain constant pressure (within 2% of the set point). The program also calculated the flux and displayed this value along with pressure, conductivities, and permeate mass for the operator. Data were saved every ten seconds in a file for post-processing in Matlab.

Three geometries were tested experimentally: straight channel, $3\sin(\pi/12)$, and $6\sin(\pi/6)$. The size and shape of each channel in the experiment were the same as in the CFD simulations. For comparison to conventional RO operation, one experimental set was performed using the 65 mil mesh feed spacer that is a standard accessory of the SEPA II membrane cell. (Though 65 mil is the spacer designation, its actual thickness was measured to be 1.5 mm.) Experimental pressure and flow rate were the same as those used in the simulations. The membrane was a Dow Filmtec SW30HR cut from a 4-inch spiral-wound element. Each membrane coupon was operated first with deionized water for 30 minutes to establish its clean-water flux and determine its hydraulic permeability. The experiments were then performed, replacing the DI water with the NaCl solution and adjusting the pressure to reach the desired set point and holding it steady for at least 20

minutes. The NaCl solutions (0.4, 0.5 and 0.6 M) were prepared by mixing the corresponding amount of NaCl with DI water. The data reported started at the end of the 20-minute period. Since the permeate was not recycled in the system, the feed concentration increased over time; however, the increase occurred very slowly and at each time point the system was at quasi-steady state. The feed concentration and permeate flux were monitored and the flux value for the salt concentration of interest was obtained by averaging flux values around the target concentration. All experiments were performed in triplicate, meaning that three different membrane coupons were tested for each spacer under all of the experimental conditions.

Results and Discussion

Velocity Field

Variations in wavelength and amplitude of the sinusoidal channels had a significant effect on the geometry of the flow field; the results are shown in Fig. 3-7. The flow geometry in the straight channel was the same in all of the section views, with a distribution resembling the parabolic profile typical of laminar conditions. Unlike the straight channel, an appreciable variation of velocity distribution was observed in the three sections—peak, middle, and valley—of the sinusoidal channels. (Note that the terms “peak, middle, and valley” here refer to the way the spacers appear in Fig. 3-7, at sections a, b, and c, respectively. These terms do not indicate elevation changes). In both the peak and valley (section a and c), the highest velocities occurred along the convex wall of the channel. In addition, the width of the high-velocity region and the magnitude

of the velocity varied along the channel. The size of the high velocity region was smaller but the magnitude was higher in the peaks and valleys compared to the middles (section b). With higher amplitude or shorter wavelength, the change in velocity from peak to middle to valley became greater.

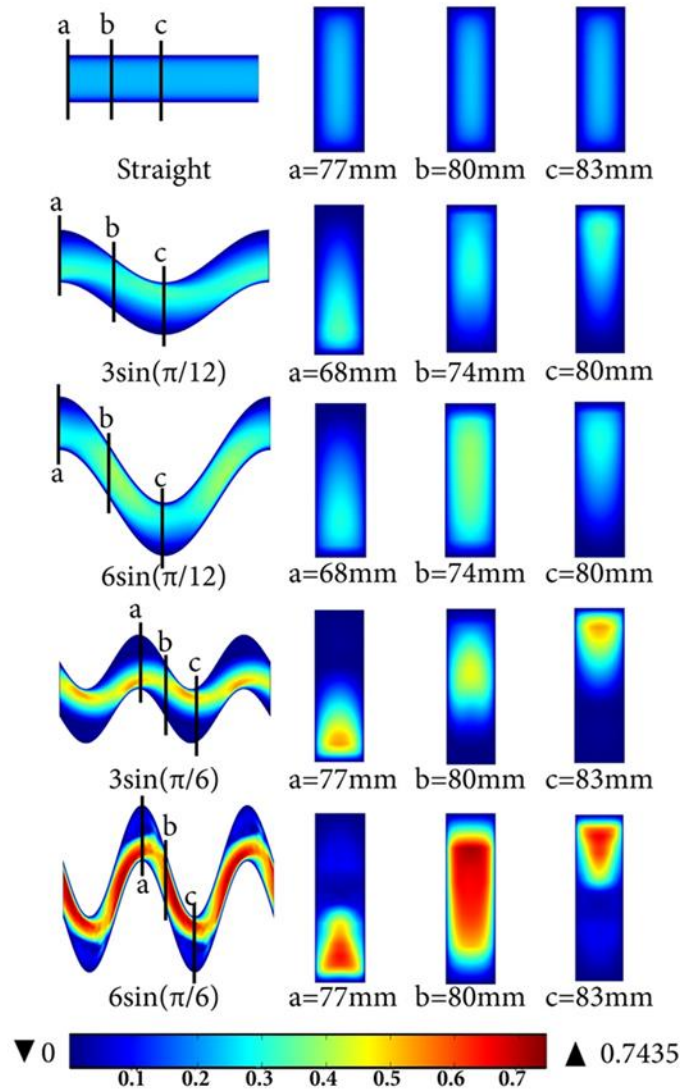


Figure 3-6. Velocity magnitudes (color flood, m/s) for the five channel geometries. Simulations shown here used a pressure of 6900 kPa and NaCl concentration of 0.6 M. At left are the plan views showing one or two wavelengths of each channel, taken at a depth of 0.75 mm. The other three views show the velocity in transverse sections located at the (a) peak, (b) middle, and (c) valley of the sinusoidal channel. The measurement under each section indicates distance from the entrance.

It seems that Taylor-Goertler vortices were generated in the peaks and valleys of the sinusoidal channels [35,36]. A vortex is shown for example in the cross-sectional views of the velocity profile for the $6\sin(\pi/6)$ channel in Fig. 3-7 at the peak and valley of the sinusoid. The main flow is shown in red, while the secondary (vortex) flow is indicated by a region of light blue opposite of the main flow. The vortex was a swirling flow generated by centrifugal force where the channel curved. The magnitude of this effect increased with the tortuosity of the channels. The swirling flow is important because it is expected to remove highly concentrated salt solution from the membrane, thereby decreasing CP and increasing the mass transfer rate. However, the vortices will also increase viscous energy dissipation and lead to greater pressure drop along the channel.

Concentration Field

The salt concentration in the straight channel increased sharply in the vicinity of the membrane, rising from an ambient concentration of 0.6 M to approximately 1.44 M adjacent to the membrane surface (Fig. 3-8). The concentration increased smoothly from the entrance to the downstream end and decreased from the membrane surface to the bulk solution, with some accumulation in the corners. However, salt in the sinusoidal channels tended to accumulate in the low velocity regions, with minimal concentration in high velocity areas. The plan view of Fig. 3-8 shows that the salt concentration at the membrane surface was lower in the more tortuous channels (with higher amplitude and shorter wavelength). The section views illustrate that the salt concentration was more

localized at the membrane in the lower-tortuosity channels, but more distributed in the higher-tortuosity cases.

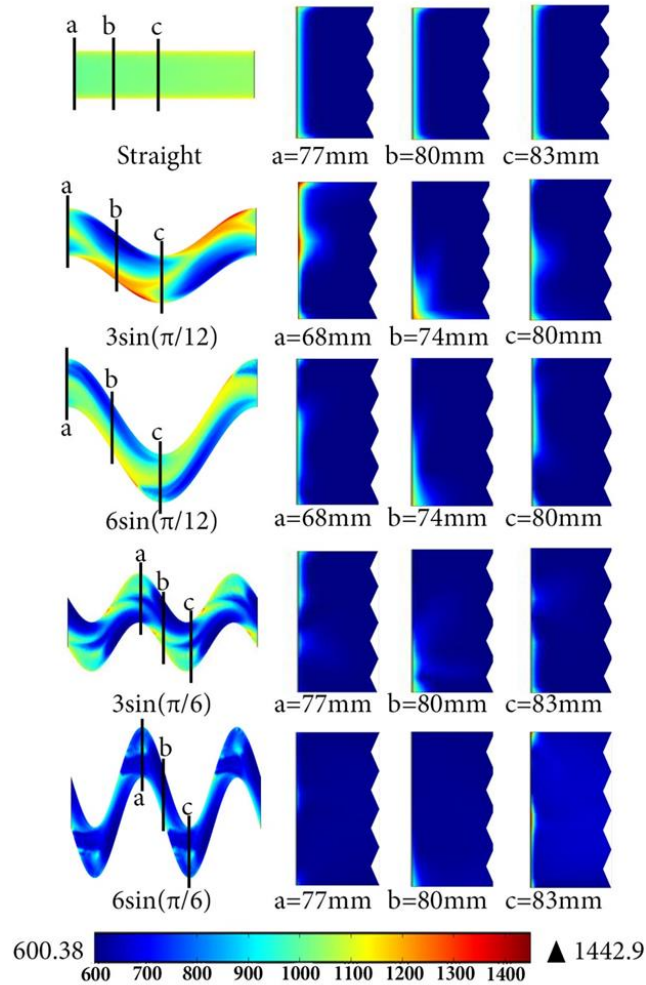


Figure 3-7. Concentration profiles for the channels (color flood, M). Simulations shown here used a pressure of 6900 kPa and NaCl concentration of 0.6 M. At left are the plan views showing one or two wavelengths of each channel, taken at the membrane surface. The other three views show the concentration in transverse sections located at the (a) peak, (b) middle, and (c) valley of the sinusoidal channel. The measurement under each section indicates distance from the entrance. To better illustrate the CP, all the section views were extended 4 times in the x direction and only the quarter of the total channel next to the membrane is shown, with a jagged line indicating the break opposite the membrane.

A quantitative evaluation of performance was done by calculating the CP factor, which is the ratio of the average salt concentration at the membrane wall divided by the

average (or feed) concentration (C_w/C_f). The results indicate that the CP factors for the sinusoidal channels were reduced compared to the straight channels (Fig. 3-9); for example, under the condition of 6900 kPa pressure and 0.6 M inlet concentration the reductions were 14, 16, 28, and 40% for the $3\sin(\pi/12)$, $6\sin(\pi/12)$, $3\sin(\pi/6)$ and $6\sin(\pi/6)$, respectively. These results suggest that in general increasing the ratio of a/L in Equation (1) helps to achieve lower CP.

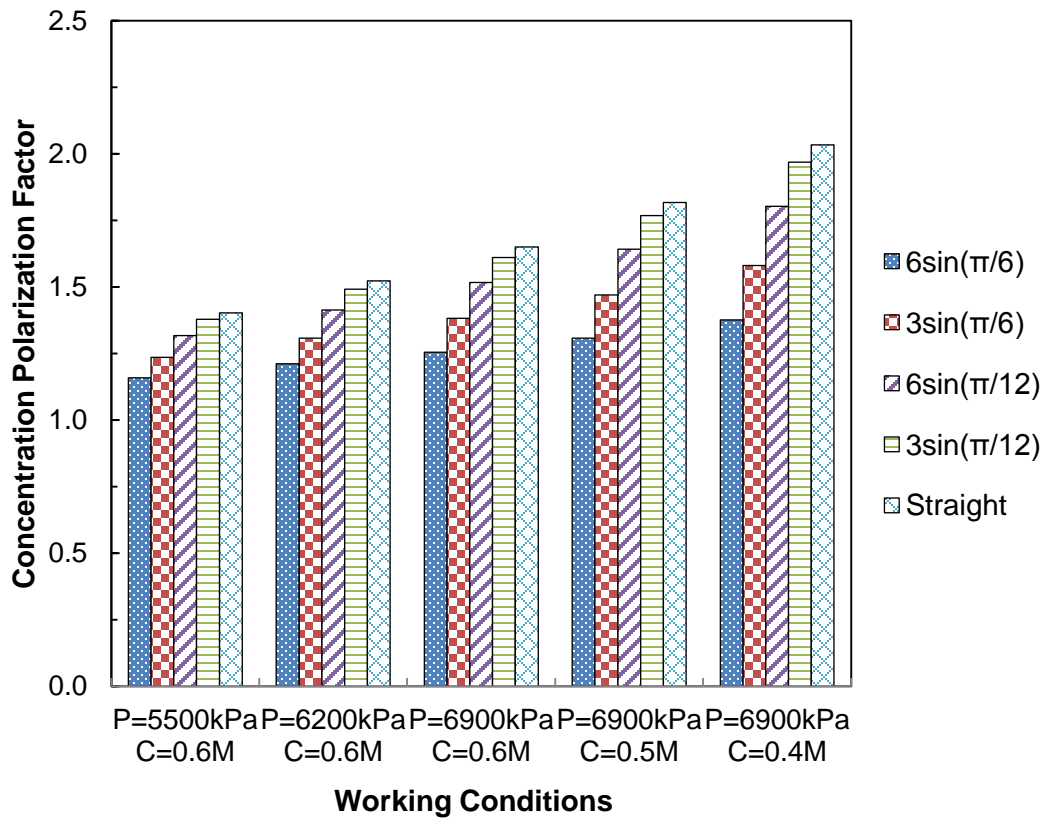


Figure 3-8. CP factors for different conditions in the numerical simulations

Permeate Flux

Permeate fluxes calculated from simulation data were greater in the sinusoidal channels compared to the straight channel (Fig. 3-10); for example, under the working

condition of 6900 kPa pressure and 0.6 M concentration the flux values were 1.28, 1.32, 1.54 and 1.79 times the straight channel flux for sinusoidal channels $3\sin(\pi/12)$, $6\sin(\pi/12)$, $3\sin(\pi/6)$ and $6\sin(\pi/6)$, respectively.

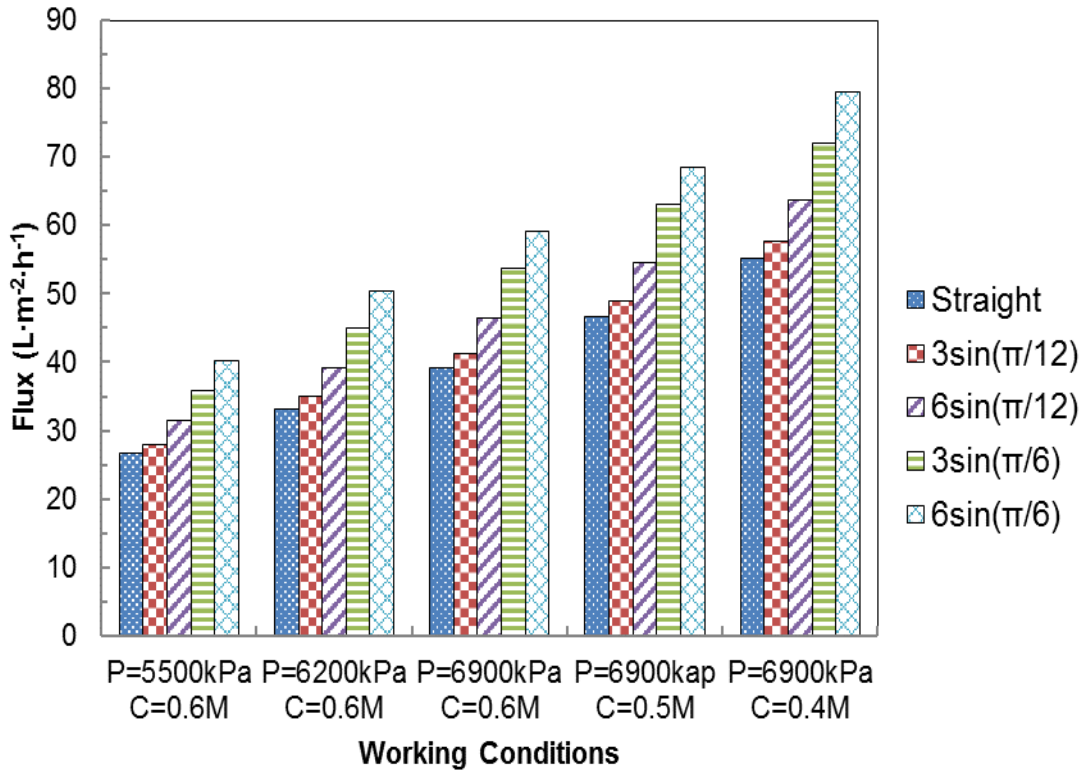


Figure 3-9. Flux data for different conditions in the numerical simulations.

Permeate flux was a quantity that could be verified with experimental data. The experimental flux data for straight, $3\sin(\pi/12)$ and $6\sin(\pi/6)$ channels were obtained from the bench scale setup (Fig. 3-11). In addition, the performance of the membrane system without any spacer was tested, and those results are termed “empty” channel (Fig. 3-11). Experimental results confirm that the permeate flux with spacers was higher than that from an empty channel. The permeate flux from the sinusoidal channels was greater than both the straight channel and the conventional mesh spacer.

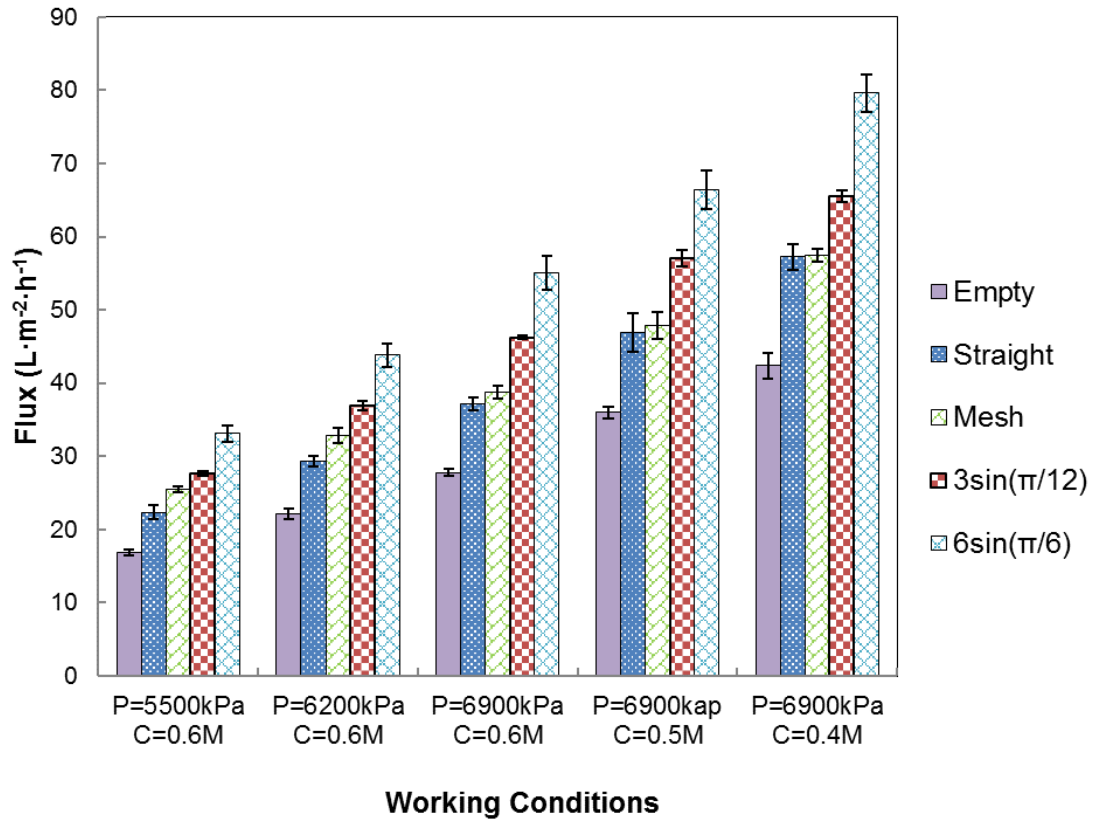


Figure 3-10. Flux data from experiments. Data are based on the average of triplicate tests. Error bars represent the standard deviation

The simulations successfully predicted the permeate fluxes in the experiments; Fig. 3-12 shows that the experimental and simulation data plotted against each other fall roughly onto a one-to-one line. There were some systematic variations, such as the simulations overpredicting the flux for the $6\sin(\pi/6)$ case; nevertheless, the modeling results are similar to the experimental results overall and it can be concluded that CFD was a useful tool in predicting the flux for these experiments.

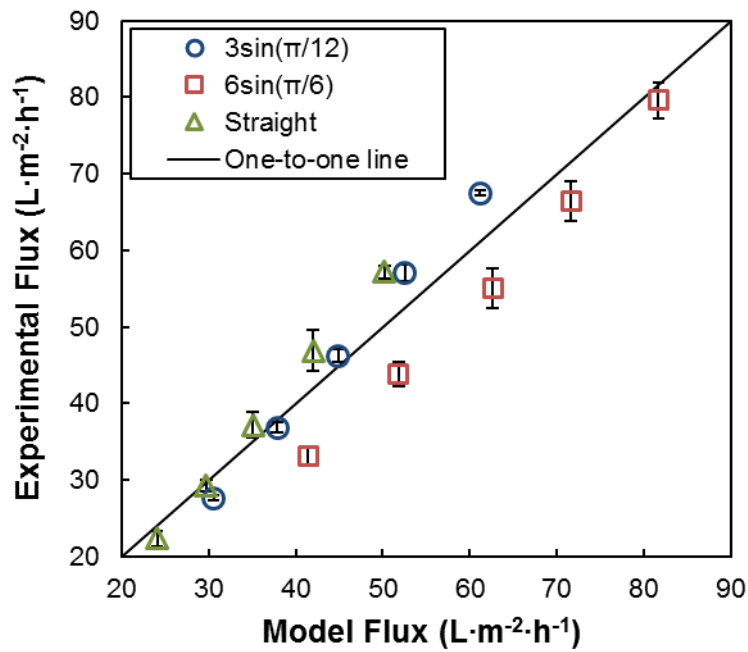


Figure 3-11. Comparison between flux values for simulations and experiments. All working conditions (pressure and NaCl concentrations) are represented. Error bars show the standard deviation for triplicate experiments.

Pressure Gradient

The energy requirements were evaluated using the overall pressure gradient, defined as the pressure drop (kPa) per meter of straight line distance between inlet and outlet. The pressure gradient could not be measured directly in the lab due to a lack of the high-precision pressure transducers that would be required to detect small differences in pressure across the membrane cell at an overall quite high pressure (up to 6900 kPa). Thus the pressure gradients were obtained only from the simulations.

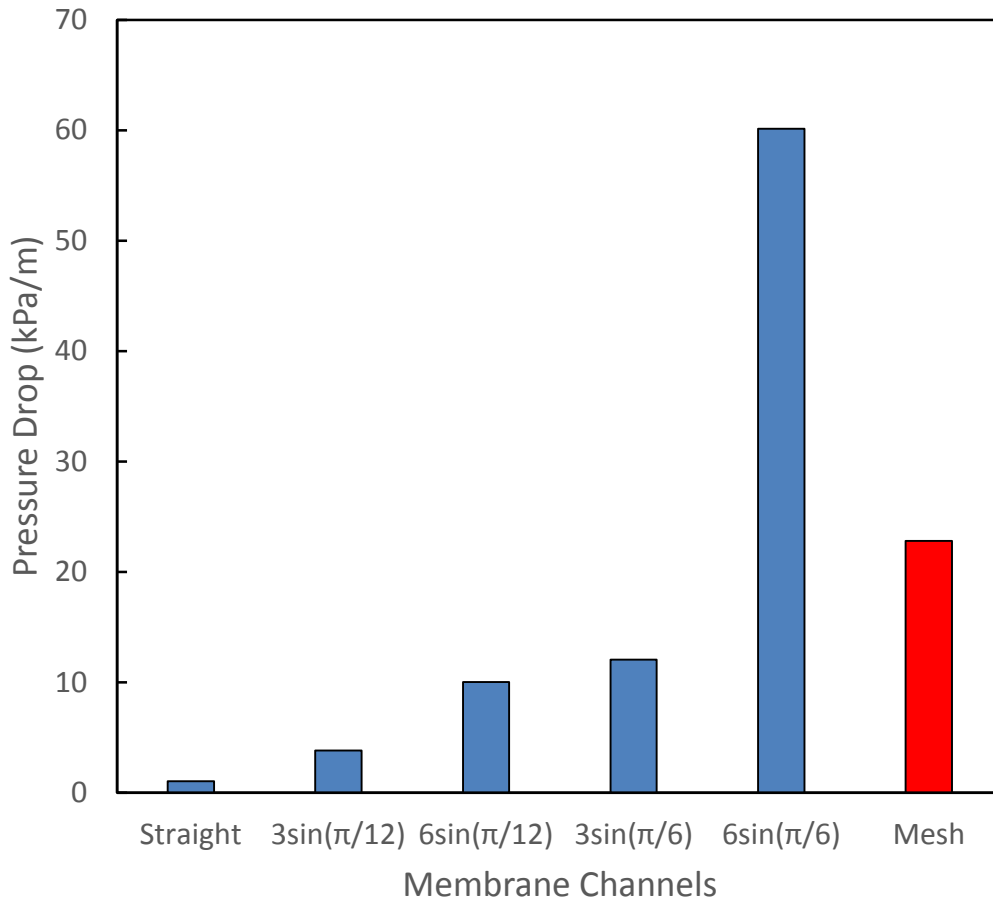


Figure 3-12. Pressure gradient obtained from simulations for various channels. The mesh spacer data point is highlighted in red for quick comparison to this conventional condition.

The pressure gradient was lowest (1.0 kPa/m) in the straight channel and increased to 7.3 kPa/m for the mesh spacer. The pressure gradient in the sinusoidal spacers spanned a broad range and generally increased with a/L (Fig. 3-13). The maximum pressure gradient was 60 kPa/m for the $6\sin(\pi/6)$ channel, which also had the best permeate flux. Thus, even though the $6\sin(\pi/6)$ geometry resulted in a two-fold flux enhancement compared to the straight channel, its pressure gradient was about eight

times greater than the mesh spacer, perhaps making it too energy intensive for practical application.

The $3\sin(\pi/12)$ channel produced higher permeate flux than the mesh spacer in experiments (Fig. 3-11) and it had a lower overall pressure gradient in the simulations (Fig. 3-13). This is an important finding because it demonstrates the feasibility of using CFD and experiments to identify RO spacer designs that may out-perform current technology. Numerical optimization methods are readily integrated with CFD and they provide a path forward for designing even better RO spacers in the future.

Conclusions

The performance of sinusoidal spacers in RO was simulated numerically and tested experimentally. Both experimental and modeling data demonstrate a permeate flux enhancement by sinusoidal channels. The simulation enabled the flow and concentration fields to be visualized inside the channels, showing that sinusoidal channels generated vortices with maximum flow velocities that increased with the amplitude and decreased with the wavelength of the sinusoid. The vortices increased mixing that reduced the concentration at the membrane, enhancing the permeate flux. The pressure drop, and thus the energy loss, increased with more tortuous sinusoids showing that an appropriate geometry must be designed to strike a balance between the benefits of enhanced flux and the costs of increased energy loss.

CHAPTER FOUR

MITIGATING MEMBRANE FOULING WITH SINUSOIDAL SPACERS

Materials and Methods

Experimental Setup

Before the experiments, the membrane coupon was soaked with deionized (DI) water overnight. For the first hour of each experiment, the system was operated with DI water in order to stabilize the membrane and obtain the clean-water flux to calculate the hydraulic permeability of the membrane. At the end of the first hour, the DI water was replaced by 10 L of fouling solution which consisted of humic acid (MP Biomedicals; catalog number 198763; lot number 7078J) (30 mg/L), calcium chloride (30 mmol/L) and sodium bicarbonate (1 mmol/L). The pH value of the fouling solution was 6.0. Humic acid was chosen as the foulant because of its ability to cause flux reduction and color the membrane surface.

Two sets of experiments with the same solution but different durations were performed. The purpose of the first set was to examine if sinusoidal spacers would be able to reduce flux decline compared to mesh spacers. The purpose of the second set of experiments was to obtain the fouling image on the membrane surface and use them to verify the fouling patterns from simulations. The first set of experiments was terminated when 5 L of permeate was collected. The average value of permeate flux over the last 10 seconds was used to compare with DI water flux obtained at the beginning of the experiment to calculate the flux decline. The second set of experiments were terminated after 1 L of permeate was collected. The stop point of these experiments was determined

by trial and error in order to generate membrane coupons which could show images of foulant distribution where the local variation of fouling severity was clearly visible. The membrane coupons after this set of fouling experiments were saved and scanned to create the fouled membrane images. All experiments were performed in triplicate, meaning that three different membrane coupons were tested in three different experiments for each spacer.

Model Description

The purpose of the modeling was to study the hydrodynamic and concentration profiles which are very difficult to observe via lab experiments. Simulations were performed in Comsol Multiphysics 4.2a on the Palmetto Cluster. The appropriate mesh density for each model was determined by comparing results from different mesh densities, as described in Chapter 3. The models used the same mesh scheme described there.

Models were designed to simulate the development of a foulant layer on the membrane surface over time under given thermo- and hydrodynamic conditions. The model also assumed that the foulant layer would not cause flux decline or changes in the cross-sectional area of the membrane channel. As a result, the profile of velocity and concentration distribution of non-foulant would remain constant so that the velocity could be solved by a steady state simulation separately in order to reduce the computational burden. The results of hydrodynamics and non-foulant concentration distribution were then coupled to complete the simulation of the fouling process on the membrane surface.

The foulant layer development was modeled as an adsorption process calculated in a time-dependent solver.

Theoretical Equations

Both steady state and time-dependent simulations were performed in this study. In the first simulation step, a steady state simulation was used to solve hydrodynamic parameters by fully coupling Equations (1) to (4). The inflow velocity was 0.15 m/s and the applied pressure was 600 psi. The hydrodynamics solution obtained from the first step was used as the initial condition for the second step. In the second step, a time-dependent simulation was used to describe the chemical transport and reaction that resulted in membrane fouling. In the model, foulant transport and adsorption was solved by Equations (5) and (6)

$$u\nabla \cdot c_f = D_f \nabla^2 c_f \quad (5)$$

$$\frac{dc_s}{dt} = k_1(c_{sm} - c_s)c_f - k_2c_s \quad (6)$$

Where c_f is the foulant concentration in the bulk, D_f is diffusion coefficient for foulant, c_s is the foulant concentration on the membrane surface, c_{sm} is the maximum surface concentration of foulant, and k_1 and k_2 are the adsorption and desorption rate constants, respectively. The values of D_f ($2.2 \times 10^{-11} \text{ (}\frac{m^2}{s}\text{)}$), k_1 , k_2 , and c_{sm} ($0.105 \frac{\mu g}{cm^2}$) are from the study of Jones et al. [84]. While D_f and c_{se} were reported directly, k_1 and k_2 were calculated via:

$$k_2 = R_0 \theta^2 D_f / C_{se} \quad (7)$$

$$k_1 = k_2 / \theta \quad (8)$$

Where R_0 (9000) is the ratio of diffusion-controlled adsorption characteristic time and reaction-controlled characteristic time. θ ($0.765(\mu\text{g}/\text{cm}^2 \times \text{s} \times 10^5)$) is the ratio between k_2 and k_1 .

The values of D_f , k_1 , k_2 , and c_{se} are from the study of Jones et al. [84], which described humic acid adsorption onto ultrafiltration membranes. The values used here were those reported for pH 8, and 0.001 M ionic strength because it was close to operational condition in our experiments. It is recognized that the exact adsorption parameters would likely vary between the Jones et al. study and this work, since the membrane materials were different and the humic acid was from a different supplier. These were chosen because they were the most appropriate parameters found in the literature (from similar experiments with polymeric membranes and humic acid). The simulation results are not meant to be exactly quantitative, but are rather meant to indicate relative accumulation levels and provide a qualitative understanding of fouling evolution.

Returning to Equation (6) we note that this is the differential equation form of Langmuir's adsorption model which has the following assumptions [84,100]:

1. The physical and chemical properties of the membrane surface are homogenous.
2. There is no interaction among solutes, nor among adsorbates.
3. The foulant only forms a monolayer on the membrane surface.

In this adsorption construct the impact of fluid flow is not included. In order to include the influence of hydrodynamics, a modified equation is proposed:

$$\frac{dc_s}{dt} = k_1(c_{se} - c_s)c_f - k_2c_s - R_s \quad (9)$$

Where the new term, R_s , is the desorption rate caused by the shear stress. When $c_s > 0$, R_s is defined as:

$$R_s = k_3 \tau f(\tau) \quad (10)$$

Where k_3 (5×10^{-17}) is a constant, τ is the shear stress, and $f(\tau)$ is a smoothed step function. Both k_3 and $f(\tau)$ were obtained via a trial and error method in which they were adjusted until a combination was found that produced fouling images similar to the ones from the experiments.

Results and Discussion

Flux Decline percentage and pressure drop

The flux decline percentage was measure as:

$$\alpha = \frac{J_{DI} - J_f}{J_{DI}} \times 100\% \quad (11)$$

where α is the flux decline percentage, J_{DI} is the average flux of the final three minutes of the DI water run and J_f is the average flux of the final three minutes of the fouling experiment. Flux decline percentage was used as the criterion to evaluate the fouling resistance performance of each spacer.

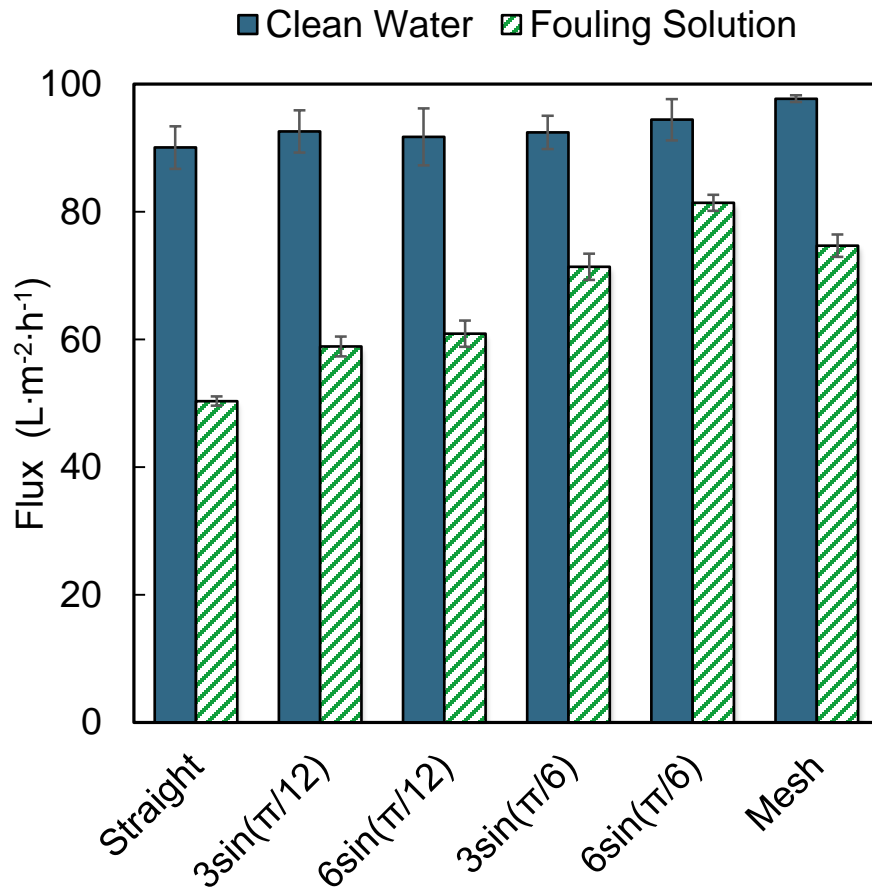


Figure 4-1. DI water flux compared with final flux from the experiments. Data are based on the average of triplicate tests. Error bars represent the standard deviation.

Among the sinusoidal spacers, the values of J_{DI} were similar to one another, while J_f was altered by the different spacer patterns (Fig.4-1). By increasing the amplitude or reducing the wavelength of the sinusoidal wave, J_f was increased. The mesh spacer showed a higher J_{DI} because it probably had a larger active membrane area but it should be noted that the active membrane areas for all sinusoidal spacers and the straight spacer were the same.

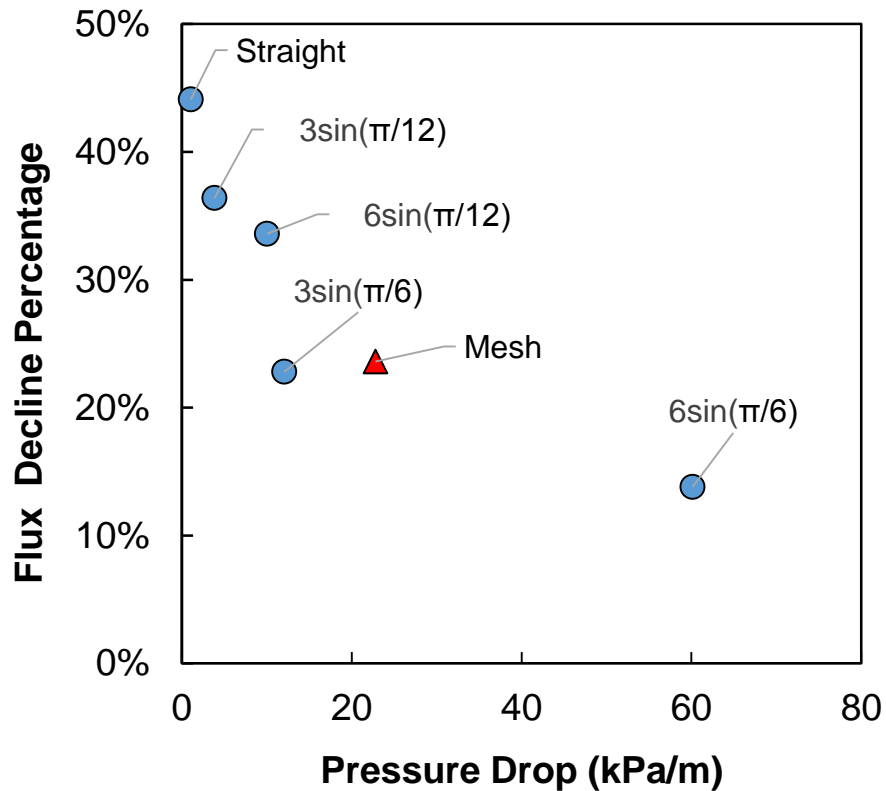


Figure 4-2. Flux decline percentage vs the pressure drop from all the spacers under cross flow velocity 0.15 m/s and applied pressure 600 psi.

As shown in Fig. 4-2 the sinusoidal spacers and mesh spacer all exhibited lower flux decline percentages than the straight spacer. In addition, the flux decline of the sinusoidal spacers $3\sin(\pi/6)$ (22.8%) and $6\sin(\pi/6)$ (13.8%) were lower than the conventional mesh spacer (23.6%) which demonstrates an improvement in fouling resistance.

The longitudinal pressure drop of the various channels was evaluated by computational simulation, and is compared with flux decline in Fig. 4-2 (note that Fig. 3-13 also shows the pressure drop data). The smallest pressure drop was observed with the straight channel (1 kPa/m) and the largest pressure drop was from the channel formed by $6\sin(\pi/6)$ (60 kPa/m). The mesh spacer showed the second largest pressure drop (23

kPa/m) which was greater than the $3\sin(\pi/6)$ spacer (12 kPa/m). These data show that $3\sin(\pi/6)$ was capable of reducing fouling more effectively and with less energy consumption than the mesh spacer under the same inflow velocity.

Foulant Accumulation on Membrane Surface

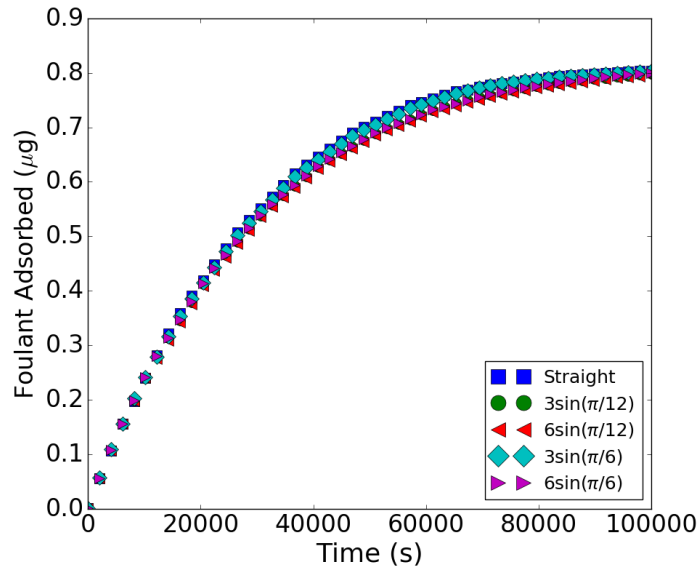


Figure 4-3. Simulation results of total mass of foulant adsorbed onto membrane surface over time from different spacers when the adsorption equation did not consider the impact of shear stress. The cross flow velocity was 0.15 m/s and applied pressure was 600 psi.

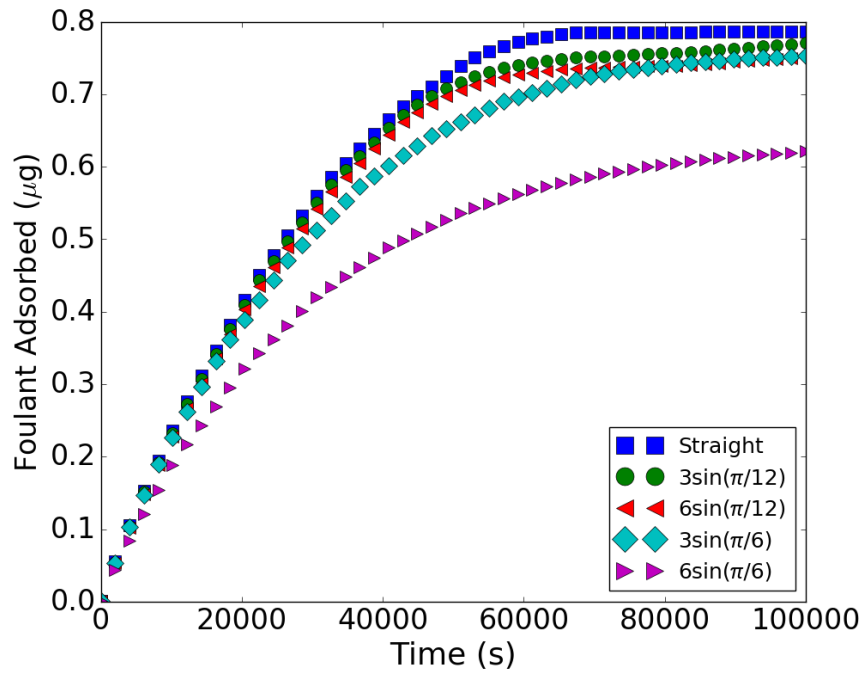


Figure 4-4. Simulation results of total mass of foulant adsorbed onto membrane surface over time from different spacers when the adsorption equation considered the impact of shear stress. The cross flow velocity was 0.15 m/s and applied pressure was 600 psi.

Without shear stress (Fig. 4-3), the foulant accumulation was similar among all spacers over the time. However, Fig. 4-4 showed that the foulant accumulation would be different if the shear stress was included. It was also shown in Fig. 4-4 that the spacer with higher tortuosity had less mass accumulated, which was consistent with the Fig. 4-1 in which the spacer with higher tortuosity exhibited lower flux decline. Therefore, the simulation that took shear stress into account was chosen in the following analysis. The velocity distribution (Fig. 3-7) from simulations showed that the vortices inside the sinusoidal channels increased with the tortuosity of the geometry. The enhanced vortices would cause higher shear stress which resulted in higher removal and pressure drop.

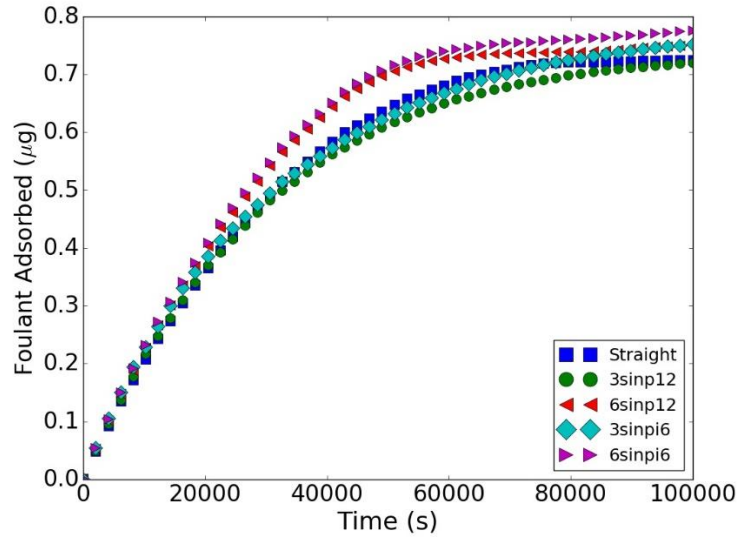


Figure 4-5. Simulation results of total mass of foulant adsorbed onto membrane surface over time from different spacers with shear stress under equal pressure drop condition.

To further the analysis of the spacer performance on energy consumption, we adjusted the inflow velocity for each spacer to arrive at the same level of pressure drop (10 kPa/m). With the new pressure drop came the new inflow velocities: $6\sin(\pi/6)$ (0.058 m/s), $3\sin(\pi/6)$ (0.132 m/s), $6\sin(\pi/12)$ (0.15 m/s), $3\sin(\pi/12)$ (0.245 m/s) and straight (0.32 m/s). Under these conditions, the straight spacer accumulated less foulant compared to all the sinusoidal spacers except $3\sin(\pi/12)$ (Fig. 4-5) and $6\sin(\pi/6)$, in contrast, accumulated the most foulant. This is because lower crossflow velocity would cause higher CP and lower shear stress on the membrane surface which would exacerbate the adsorption of foulant.

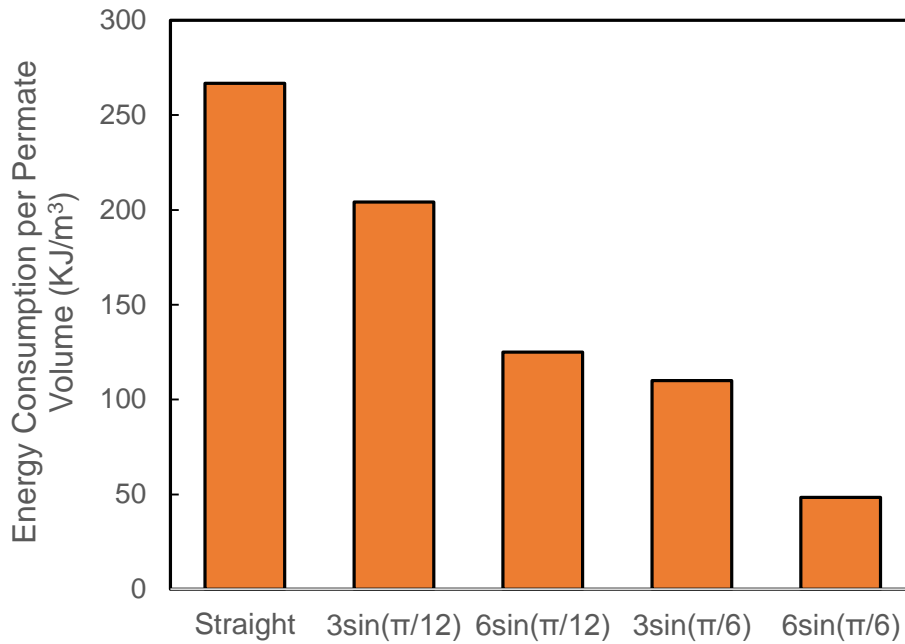


Figure 4-6. Energy consumption per unit volume of permeate production under equal pressure drop scenario with 0.001M sodium chloride solution.

Fig. 4-6 shows the energy consumption (ΔE) for producing unit volume of permeate with 0.001 M sodium chlorine solution. ΔE was calculated via:

$$\Delta E = \Delta P / Y \quad (12)$$

Where ΔP (kPa) is the longitudinal pressure drop and Y is the recovery.

It was shown that the energy consumption per unit volume of permeate production decreased as the tortuosity of the sinusoidal spacer increased. The straight spacer showed the highest energy consumption. This is because under these conditions the sinusoidal spacer with more tortuous geometry would be able to create higher recovery.

Fouling Image

The fouling distribution from simulations successfully captured the important details of the fouling pattern observed in the experiments (Fig. 4-7). The simulation images were chosen at $t = 40000$ s because the fouling patterns were clear at that time point. In the straight channel, the foulant deposited evenly in the direction perpendicular to the flow and fouling concentration reduced along the flow direction. In sinusoidal spacers, the fouling concentration exhibited a periodic pattern along the sinusoidal wave. The foulant tended to accumulate in the concave and convex locations where the least shear was present in the sinusoidal period.

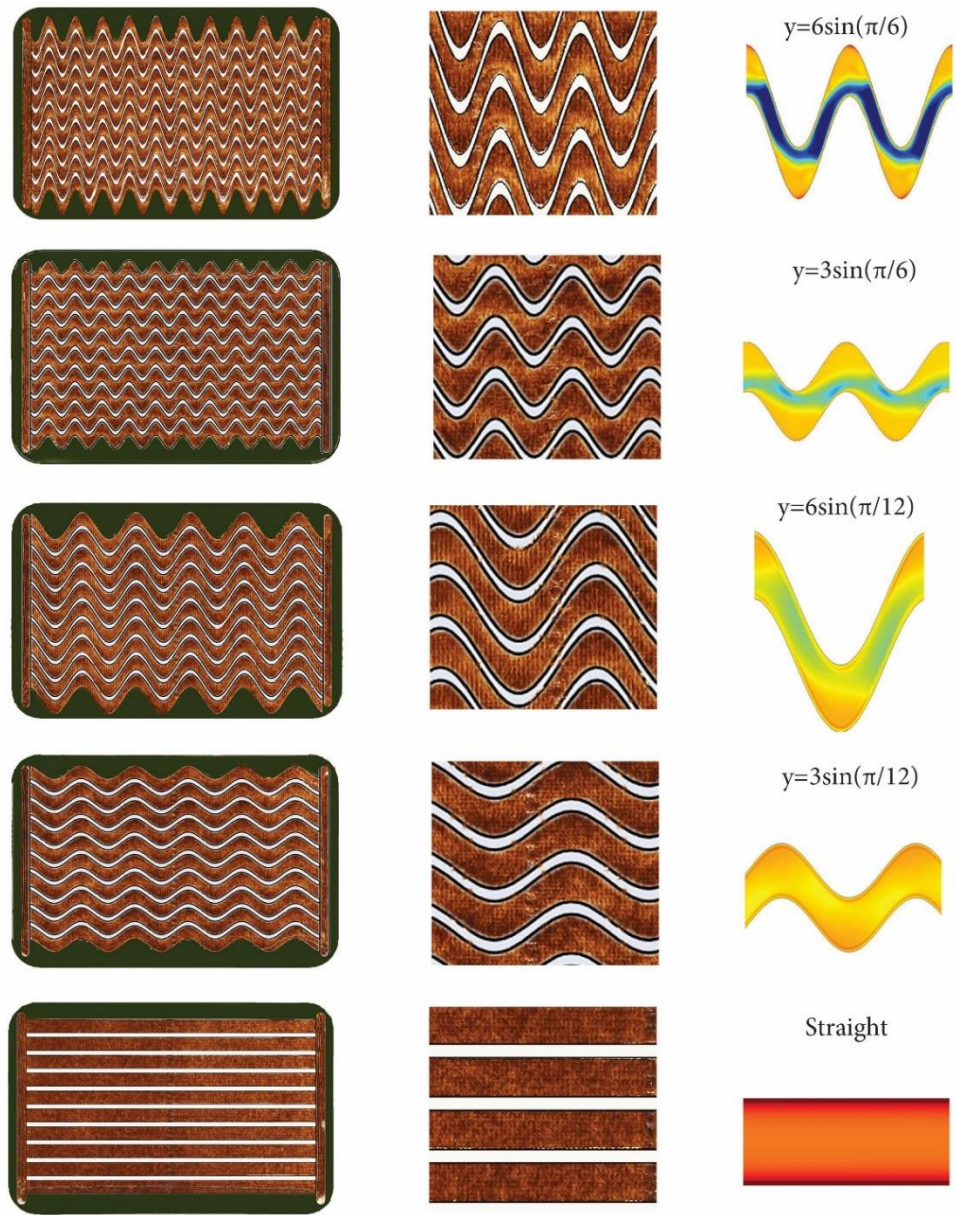


Figure 4-7. Comparison between fouled membrane images for simulations and experiments. The whole membrane coupon with spacer wall is shown at left; the zoomed view of membrane coupon is in the middle; the fouling distribution ($\mu\text{g}/\text{cm}^2$) on the membrane surface at $t=40000\text{s}$ from the simulation that included shear stress is shown at right.

Conclusion

The ability of sinusoidal spacers to reduce foulant deposition was tested and compared with a conventional mesh spacer and a straight spacer. The results showed that sinusoidal spacers were capable of decreasing deposition on membrane surface and maintaining relatively high fluxes. The flux decline ratio and pressure drop results suggested the promising prospect of using sinusoidal spacers to achieve higher flux with less energy consumption under fouling conditions. Simulation was used to qualitatively study the fouling process and the fouling distribution produced by simulation successfully predicted the local patterns of foulant accumulation. Deposition was greatest in low-velocity regions, but was reduced in high-velocity regions. An important finding of this work is that in at least one channel design [$3\sin(\pi/6)$] a decreased fouling propensity was accomplished with a relatively low pressure drop, suggesting that sinusoidal spacers (or similar novel designs yet to be developed) may be a viable approach for economically reducing fouling in membrane processes.

CHAPTER FIVE

COMPUTATIONAL MODELING OF FLUID FLOW AND MASS TRANSPORT IN FORWARD OSMOSIS AND PRESSURE RETARDED OSMOSIS

Materials and Methods

Membrane Characteristics

Two types of membranes: a thin-film composite (TFC) membrane and an asymmetric membrane were simulated in this study. The membrane characteristics such as water permeability and salt permeability were as reported in the literature [7]. For the TFC membrane, the thickness of the membrane support layer (40 μm) was estimated from information in the membrane patent application [101]. The hydraulic conductivity ($\kappa = 2.34 \times 10^{-15}$ m/s), porosity ($\varepsilon = 0.41$), tortuosity ($\tau = 1.7$) of the support layer were obtained from the papers of Tiraferri et al. [102] and Sagiv et al. [89]. For the asymmetric membrane, the thickness of the support layer (100 μm) and the porosity/tortuosity relationship ($\varepsilon/\tau = 0.163$) were obtained from the work of Phillip et al. [103]. The hydraulic conductivity ($\kappa = 2.34 \times 10^{-15}$ m/s) of the support layer was obtained from the paper of Sagiv et al. [89].

Equations for fluid flow and mass transfer

Water flow in the feed and draw channels was calculated by the Equations (1) and (2). The fluid flow within the membrane support layer was treated as fluid flow in a porous media which was calculated with the Darcy-Forchheimer law, which is solved numerically according to Equation (13).

$$\left(\frac{\rho}{\varepsilon}(\mathbf{u} \cdot \nabla) \frac{\mathbf{u}}{\varepsilon}\right) = \nabla \cdot \left[-P + \frac{\mu}{\varepsilon}(\nabla \mathbf{u} + (\nabla \mathbf{u})^T) - \frac{2\mu}{3\varepsilon}(\nabla \cdot \mathbf{u})\right] - (\mu k^{-1} + \beta_F |\mathbf{u}|)\mathbf{u} \quad (13)$$

Here u is velocity in the membrane support layer, ε is the layer's porosity, k is the layer's water permeability, and β_F is the Forchheimer coefficient, which is used to describe the impact of turbulent drag. It is calculated via:

$$\beta_F = \frac{1.75}{\sqrt{150\varepsilon^3}} \cdot \frac{\varepsilon\rho}{\sqrt{k}} \quad (14)$$

With the addition of Forchheimer coefficient Equation (13) would be able take into account the turbulence and transient effect at the interface of the free water channel and porous media [104].

The flux of water through the membrane selective layer was calculated by:

$$J_w = A_F \cdot (\pi_d - \pi_f) \quad (15)$$

Where J_w is the flux of water through the membrane, A_F is the water permeability of the membrane at 293 K (room temperature), π_d is the osmotic pressure on the draw solution side near the active layer of the membrane, and π_f is the osmotic pressure at the feed solution side near the active layer of the membrane. In the model the active layer had no thickness, but was instead treated as a boundary between the feed channel and support layer computational domains.

The solute (salt) transfer in the membrane channel was calculated by Equation (3). The solute transfer in the membrane support layer was calculated by:

$$u\nabla \cdot c = D_e \nabla^2 c \quad (16)$$

Where D_e is the effective diffusion coefficient in the membrane support layer calculated by:

$$D_e = \frac{\varepsilon}{\tau} D \quad (17)$$

The flux of salt through the membrane can be obtained by:

$$J_s = B \cdot \Delta c \quad (18)$$

Where J_s (mol/s/m²) is the flux of salt through the membrane, B (m/s) is the salt permeability of the membrane, and Δc is the salt concentration gradient between the two sides of the selective layer.

The laminar flow and transport of diluted species physics in Comsol Multiphysics were used to study flow and mass transport in the feed and draw channel. The flow in porous media and transport of diluted species physics in porous media in Comsol were used to study flow and mass transport in the membrane support layer.

The locations of the boundaries in the simulation of FO and PRO membrane channels are described in Fig. 5-1 and Table 5-1. In the table, the locations where mass (water and salt) flow into and out of the simulation are indicated by “inlet” and “outlet,” respectively. Where a variable is given (such as “ u_f ” for feed inlet velocity), the value of the variable is defined in the description of each scenario. Some of these values are fixed (u_f , u_d , c_f , and c_d), while others are calculated during the simulation (J_w and J_s). Steady state models were used throughout this ODMP simulation work.

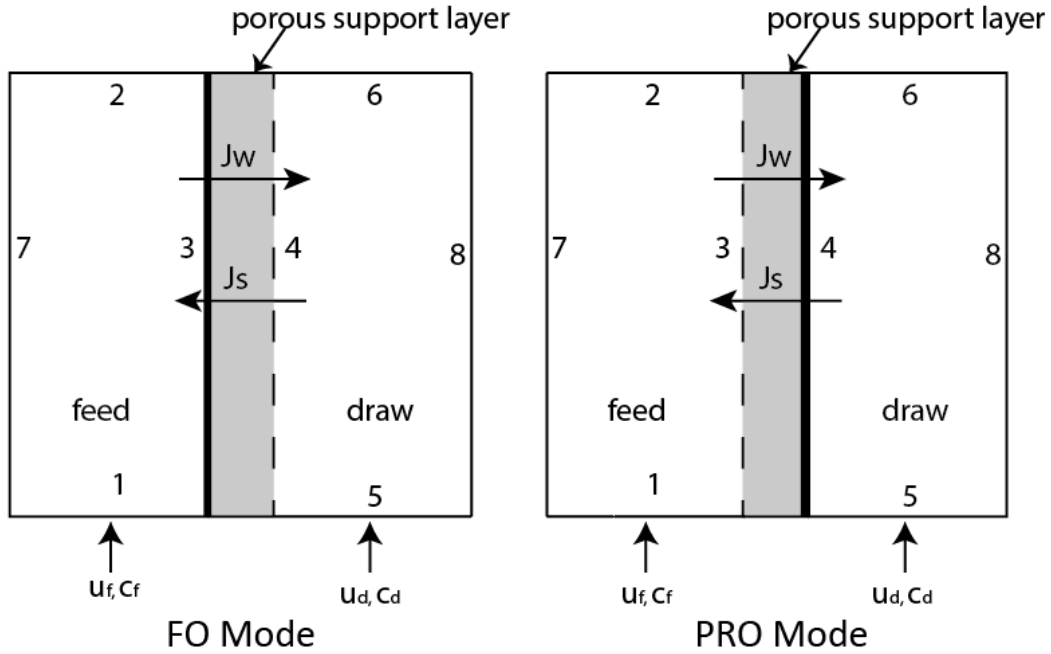


Figure 5-1. Osmotic driven membrane channel domains for two configurations: (left) FO mode in which the active layer (indicated by the bold vertical line) faces the feed-side; (right) PRO mode in which the active layer faces the draw channel. The porous support layer is denoted by the grey area. Inflow of water and salt concentration in feed and draw are denoted by u_f , u_d , c_f and c_d respectively. Fluxes of water and salt are denoted by J_w and J_s , respectively. The boundaries are numbered 1–8.

Table 5-1. Boundary settings for FO and PRO simulations. The location of each boundary is depicted in Fig. 5-1.

Boundary Number	Navier-Stokes			Solute Convection and Diffusion		
	Feed Channel	Porous	Draw Channel	Feed Channel	Porous	Draw Channel
1	Inlet (u_f)			Inlet (c_f)		
2	Outlet			Outlet		
3	Outlet (J_w)	Inlet (J_w)		Inlet (J_s)	Outlet (J_s)	
4		Outlet (J_w)	Inlet (J_w)		Inlet (J_s)	Outlet (J_s)
5			Inlet (u_d)			Inlet (c_d)
6			Outlet			Outlet
7	Impermeable No-slip			Impermeable No-slip		
8			Impermeable No-slip			Impermeable No-slip

Model verification with empty membrane channels

The first step of this study was to build 2D CFD models which had the same dimensions and operating conditions (flow channel dimensions, inlet velocity, concentration, and membrane type) as a set of experimental data. The data chosen were the result of a round-robin exercise where two membrane types were tested in empty channels by multiple laboratories to help establish standard protocols for performance evaluation [4]. These data were seen as a robust, validated set, useful for comparison with our simulation results. The CFD models were designed to calculate the permeate flux based on the calculated hydrodynamics and membrane characteristics inside the membrane channel. Flux through the membrane was calculated based on the osmotic driving force created by the difference in salt concentration at the membrane walls determined by the simulation. This is noteworthy because many CFD studies of membrane processes use a fixed flux determined from experiments. Here the flux was predicted, rather than fitted to the experimental data.

The dimensions of the feed channel and draw channel were 77 mm long by 26 mm wide by 3 mm deep. Two combinations of feed and draw concentrations were tested in the experiments [4]; they were (#1) feed concentration 0 M and draw concentration 1 M; (#2) feed concentration 0.5 M and draw concentration 1.5 M. Both combinations were tested in FO and PRO mode. The crossflow velocity (u_f) was 0.25 m/s. The mesh used in the 2D model is shown in Fig 5-2.

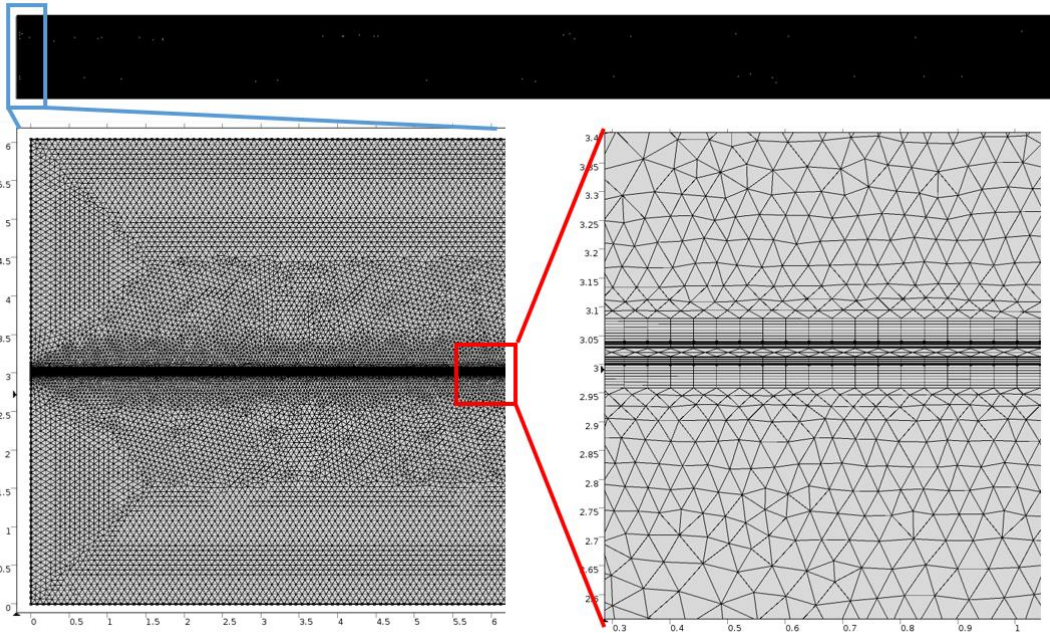


Figure 5-2 The mesh scheme (229,486 mesh elements) for 2D model of an empty membrane channel. The detailed mesh shape and distribution are presented in the two lower figures. The units of all axes are mm. In this model the TFC membrane (40 μm support layer thickness) is shown.

Spacer Filled 2D and 3D FO Channel

The model verification work discussed above was performed for simulations and experiments with empty channels. The modeling strategy thus verified was then used to evaluate spacer-filled channels. Both 2D and 3D simulations were used for this purpose. The benefit of 2D simulations is that the software can converge on a solution more easily than in 3D simulations. This allows for testing of a larger range of velocities than can be tested in 3D simulations. But because 2D simulations are not able to show the flow and concentration in angles that are not along the flow direction, 3D models are beneficial. The results from the two modeling approaches were analyzed and compared here.

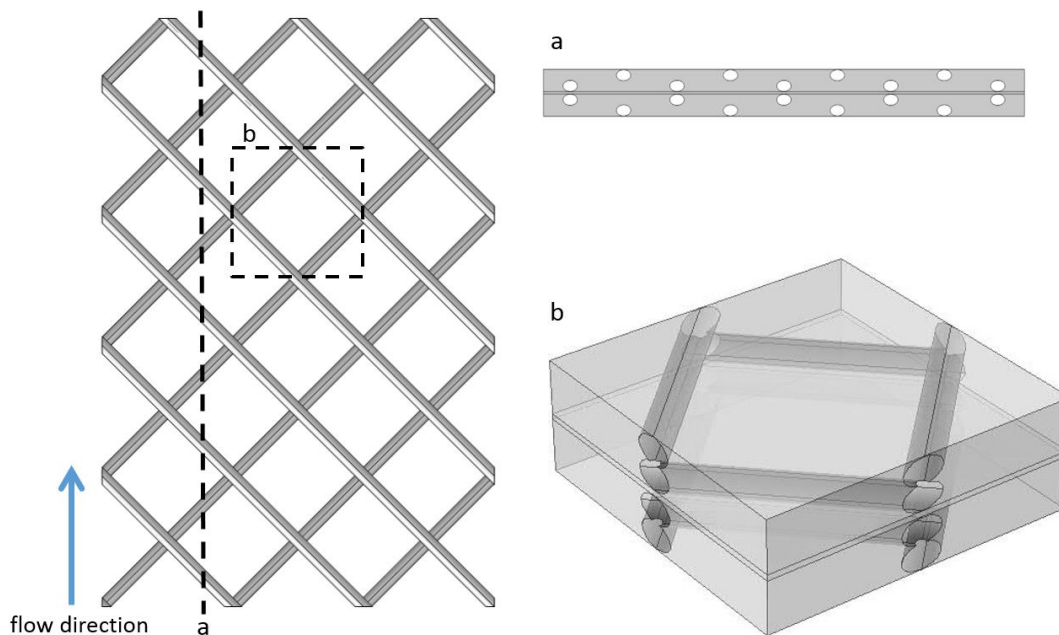


Figure 5-3. 3D illustration of mesh spacer (left). Dash line indicates the location of the 2D model (a, top right). Dash lined square indicates the location of the 3D model (b, bottom right).

The geometry of a conventional mesh spacer is usually portrayed as a fish net formed from two layers of filaments with circular cross section [32,47]. In this depiction, the top layers of filaments are always touching and blocking the membrane surface. However, based on studies of mesh feed spacer characterization by X-ray computed tomography cross sectional shape and thickness of the filaments is irregular and varies from location to location [57]. In many studies, the cross-section is considered as elliptical [57,105,106]. As a result, the filaments are not constantly in contact with the membrane; instead there is space between the membrane and the spacer in many locations. In this study, a modified geometry of 3D mesh feed spacer was used (Fig. 5-3). In this design, the mesh spacer was formed by two layers of filaments with elliptical cross sections. The center to center (CC) distance of the filaments on the same layer was 6 mm. Inside real spiral-wound modules the feed spacer is not uniformly blocking the membrane

due to the irregularity of the feed spacer shape and vibrations during operation so the membrane-filament distance should be taken into consideration. On the other hand, since membranes are tightly packed in modules the distance between spacer filaments and membranes should be very small. In this study, various membrane-filament distances were evaluated. For several model sets a 0.01 mm membrane-filament distance was chosen. The membrane channel height was set at 1 mm, so the 0.01 mm distance constitutes 1% of the membrane channel height. Note that a 3 mm channel height was used previously to make comparisons with the experimental data, which was collected with membrane cells that had that channel height. For the spacer-filled experiments, a 1 mm channel height was chosen because it is closer to the typical depth of membrane channels in spiral wound modules.

The geometry of the 2D models were taken as a cross sectional view of the 3D mesh spacer (Fig. 5-3). The dimensions for feed and draw channels were 27 mm long by 1 mm high. The dimensions for the membrane support layer were 27 mm long and 0.1 mm high. The geometry of the 3D model was taken as a portion of the mesh spacer (Fig. 5-3). Because running the 3D model required much more computational power, the dimension of the feed and draw membrane channels were limited to 6 mm long by 6 mm wide by 1 mm deep. The dimensions of the membrane support layer were 6 mm long by 6 mm wide by 0.1 mm deep. The boundary conditions were the same for the 2D empty membrane channel and the 2D spacer-filled membrane channel.).

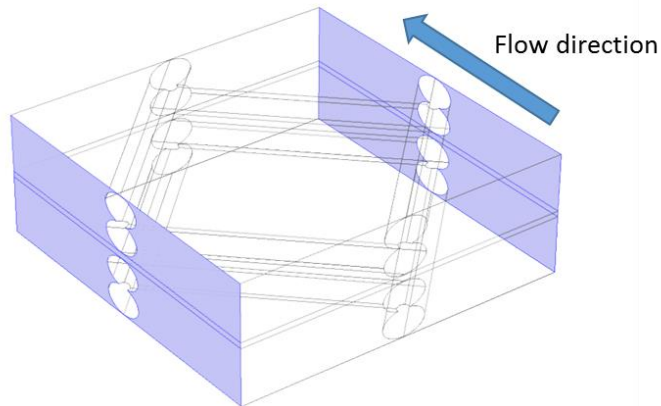


Figure 5-4. The location of periodic boundaries (marked in purple).

Because part of the entrance of the 3D model was blocked by the feed spacer (Fig. 5-4), the inlet boundary condition for the 3D model was flow rate ($6 \times 10^{-7} \text{ m}^3/\text{s}$) instead of inlet velocity as in the 2D model. This ensured that the average velocities in both 2D and 3D models would be more comparable. To reduce the impact of the boundary effects to the model, periodic boundary conditions were used in the boundaries of the channel that were 0° to the flow direction and were attached to the inlet and outlet (Fig. 5-4). It should be noted that the Reynolds number for empty membrane channels in the lab study was around 1500. Because the height of the channel was reduced from 3 mm to 1 mm and spacers were included, both 2D and 3D models were unable to converge at the original 0.25 m/s velocity. After a series of trials, the maximum cross flow velocity for a fully coupled 3D FO model to converge was 0.01 m/s. In order to study the flow pattern inside 3D FO membrane channels under higher cross flow velocity, another series of 3D models were built which only focused on fluid flow and assumed the concentration and permeate flux across the membrane was zero to help the model converge. Based on our

results the permeate flow rate was only up to 0.2% of the inlet flow rate so neglecting the permeate flux should not make a significant impact in the flow patterns. It should be stressed, however, that these zero-flux 3D models were only used to evaluate and visualize fluid flow patterns for the higher crossflow velocity cases. Conclusions regarding the effects of spacers on CP and flux were derived from the 2D and low crossflow velocity 3D simulations.

The mesh used for 2D and 3D models are shown in Figs. 5-5 and 5-6 respectively.

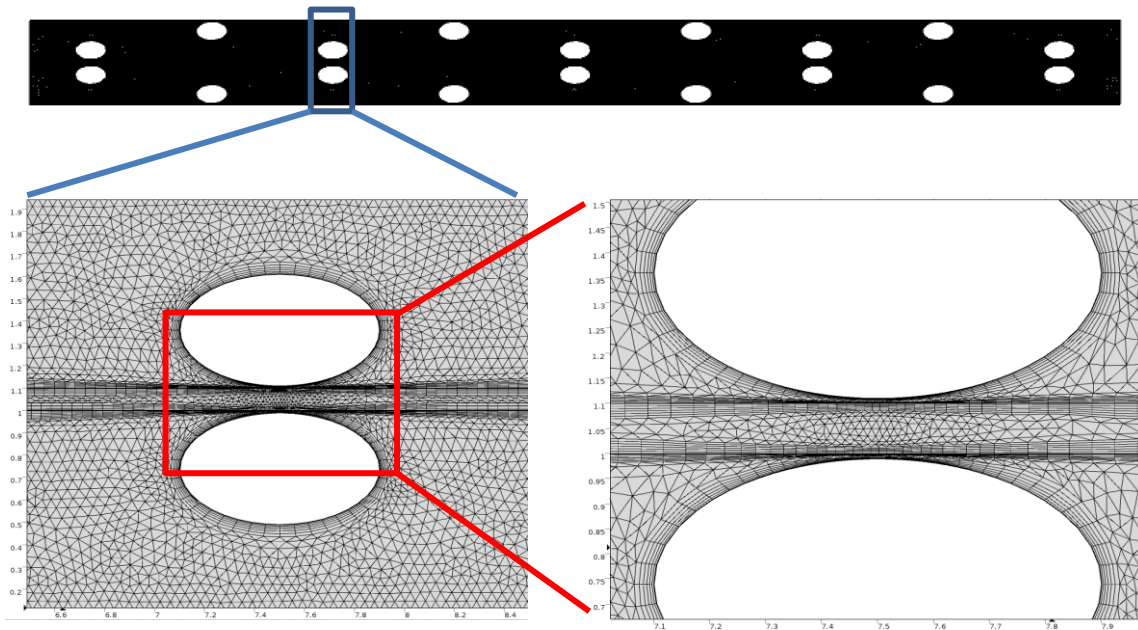


Figure 5-5 The mesh scheme (328528 mesh elements) for 2D spacer-filled FO model with 0.01 mm membrane to filament distance. The detailed mesh shape and distribution are presented in the lower two figures. The units of all axes are mm. In this model the HTI membrane (100 μm support layer thickness) is shown.

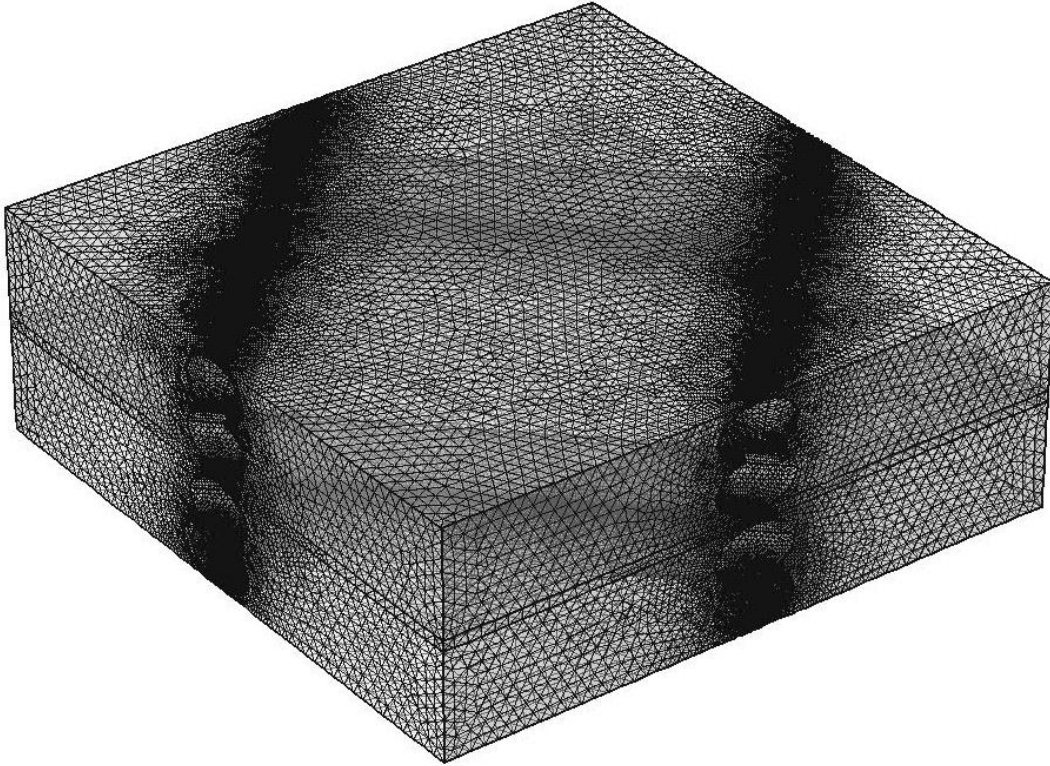


Figure 5-6 The mesh scheme (1536220 mesh elements) for 3D spacer-filled FO model with 0.01 mm membrane to filament distance.

Results and Discussion

Modeling verification

The water flux calculated from the 2D simulations was compared with the data from the experimental study [4]; results are presented in (Fig. 5-4). The error between the simulation results and literature report are summarized in Table 5-2. The error was calculated via:

$$E = \frac{|J_{model} - J_{lab}|}{J_{lab}} \times 100\% \quad (19)$$

Where E is the error between the simulations and the experiments, J_{model} is the flux obtained from the simulations and J_{lab} is the flux obtained from lab experiments.

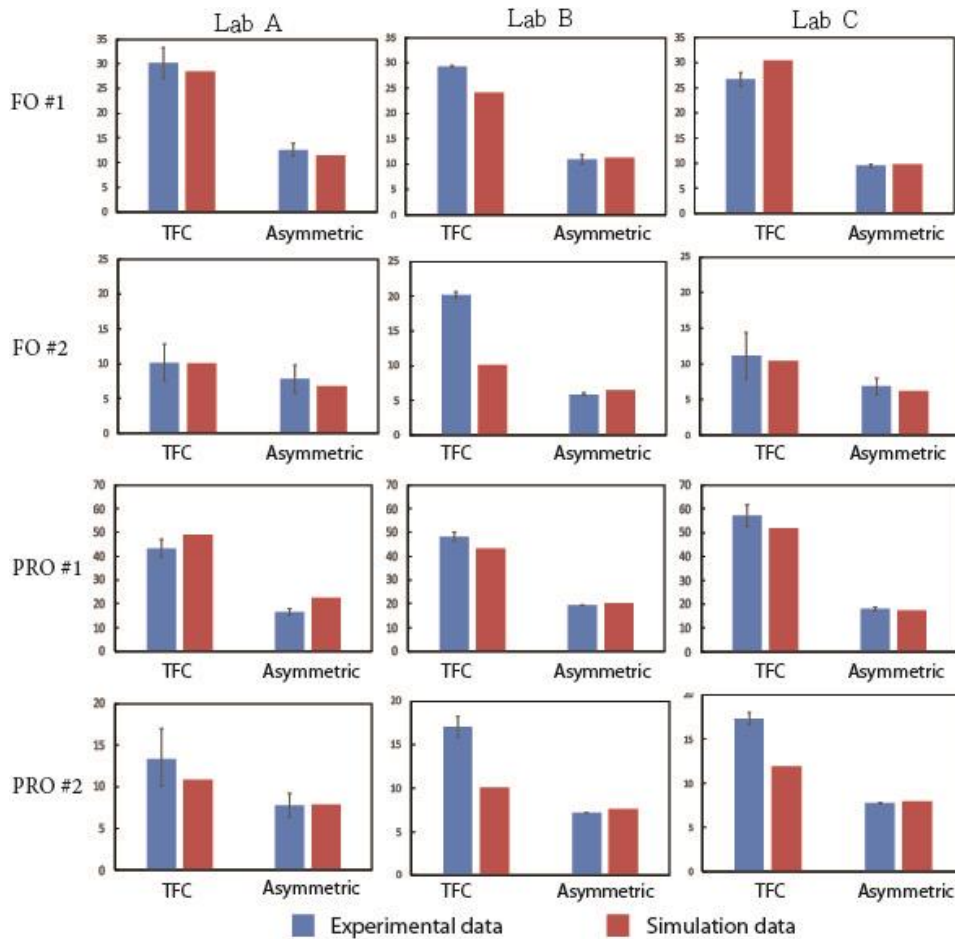


Figure 5-7. Water flux (LMH) from simulation and literature.

It is shown in Table 5-2 that except FO #2 and PRO #2 scenarios for the TFC membrane, the average difference was no more than 12%. And in general the difference was smaller for the asymmetric membrane and the two smallest average differences were found in FO #1 (5%) and PRO #2 (3%) scenarios for the asymmetric membrane. The two largest differences were observed in FO #2 (19%) and PRO #2 (30%) for the TFC membrane. It should be noted that those two scenarios also exhibited a notable difference in experimental water flux among the labs, *i.e.* in FO #2 the water flux reported by lab B

was much larger than the other two and the difference between experiments and simulations in that scenario was as high as 50%; in PRO #2 the water flux from the lab A was lower than the other two for the TFC membrane.

Table 5-2. Summary of difference of permeate flux between simulation and literature data. In scenario #1, the feed solution concentration is 0 M and the draw solution concentration is 1 M, while in #2 the feed concentration is 0.5 M and the draw solution concentration is 1.5 M.

	FO #1		FO #2		PRO #1		PRO #2	
	TFC	Asymmetric	TFC	Asymmetric	TFC	Asymmetric	TFC	Asymmetric
Lab A	6%	9%	1%	13%	13%	22%	19%	1%
Lab B	18%	3%	50%	10%	10%	11%	41%	6%
Lab C	14%	2%	7%	10%	9%	5%	31%	2%
Average	12%	5%	19%	11%	11%	12%	30%	3%

The standard deviation of each experimental result is shown in Table 5-3. The standard deviation of the experimental data on asymmetric membrane was smaller than the TFC membrane in general. As a result, parameters such as A_F and R for simulations of FO processes with spacers were based on FO with asymmetric membranes in scenario #1 (0 M feed salt concentration and 1 M draw concentration) reported by Lab B in the round-robin study. These were chosen because (as shown in Tables 5-2 and 5-3) these were the best match based on the difference between modeling and experiments (2%) and they had the lowest standard deviations (0.35 LMH).

Table 5-3. Standard deviations of water flux (LMH) in the literature data.

	FO #1		FO #2		PRO #1		PRO #2	
	TFC	Asymmetric	TFC	Asymmetric	TFC	Asymmetric	TFC	Asymmetric
Lab A	3.13	1.32	2.66	1.96	3.67	1.50	3.21	1.34
Lab B	0.14	0.97	0.43	0.16	1.83	0.10	1.16	0.04
Lab C	1.35	0.35	3.24	1.15	4.37	0.76	0.68	0.07
Average	1.54	0.88	2.11	1.09	3.29	0.79	1.69	0.48

2D Feed Spacer Filled FO Membrane Channel

Impact of spacer density

The results of the model verification exercise lend confidence toward using this modeling framework for predicting performance in alternative scenarios. Because the flux from the simulation was calculated via fully coupling the hydrodynamics and mass transfer inside the membrane channel and membrane characteristics, if the modeling could accurately predict the flux from the empty membrane channel, it is reasonable to believe that the modeling approach can also be used to predict the flux from the spacer-filled membrane channels.

Of particular interest in this work is to evaluate the effects of spacer placement in feed and draw channels. Two types of spacers with CC distance of 6 mm and 12 mm were tested in this study. The permeate flux at three different velocities (0.01, 0.08 and 0.15 m/s) from the spacer-filled membrane channels were compared to that of the empty membrane channel (Fig. 5-8). The results showed the permeate fluxes were lower in the spacer-filled channels than the empty channel at inlet velocity 0.01 m/s. In addition, the spacer with higher CC distance showed higher flux indicating that the presence of spacer reduced the permeate flux at the velocity 0.01 m/s. On the contrary, at velocities of 0.08 and 0.15 m/s, the spacer-filled channel showed higher flux than the empty channel and the spacer with lower center to center distance showed higher flux values indicating the presence of the spacer enhanced the permeate flux. Also the flux increment from 0.01 m/s to 0.08 m/s was much greater than from 0.08 m/s to 0.15 m/s which suggested increasing

velocity from 0.01 m/s to 0.08 m/s would be more beneficial than from 0.08 m/s to 0.15 m/s.

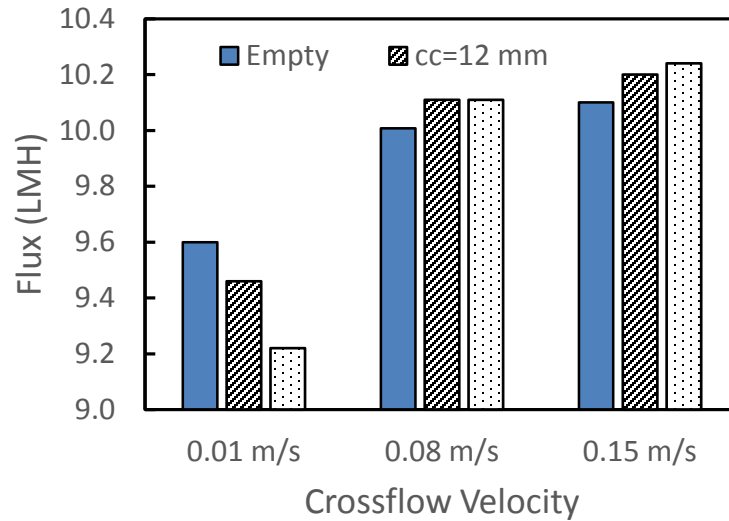


Figure 5-8. Permeate flux from empty and spacer-filled channels with CC = 6 mm and 12 mm.

The local water fluxes along the membrane surface from the different membrane channels are presented in Fig. 5-9. The feed spacer that was close to the membrane was able to cause flux variation in its vicinity. The local variation caused by the spacers was much more obvious under inlet velocity 0.01 m/s than 0.08 m/s and 0.15 m/s. Meanwhile the flux profiles for velocity 0.08 m/s and 0.15 m/s were very similar; the flux profile for velocity 0.01 m/s was distinct from the others in all of the membrane channels.

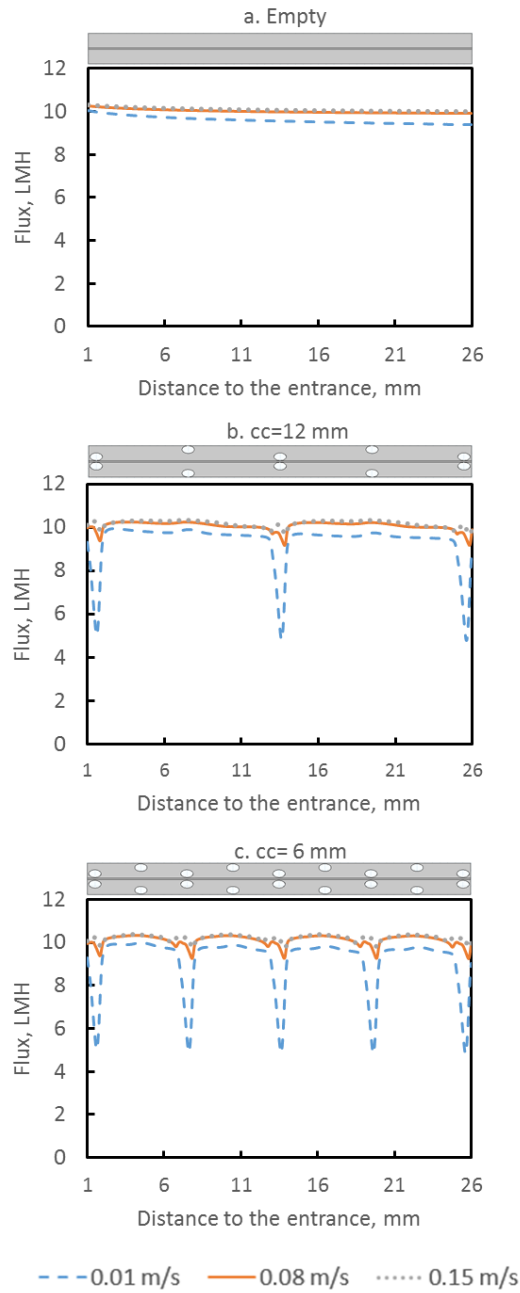


Figure 5-9. Water fluxes under different velocities along the membrane surface from the empty membrane channel and the spacer-filled membrane channels with CC = 6 mm and 12 mm and 0.01 mm distance between the membrane and spacer filaments. The first and last 1 mm of the channel were excluded to remove entrance and exit effects. The sketch of the part of the channel whose data was presented was placed on top of the corresponding plot to illustrate the location of the spacer inside the membrane channel.

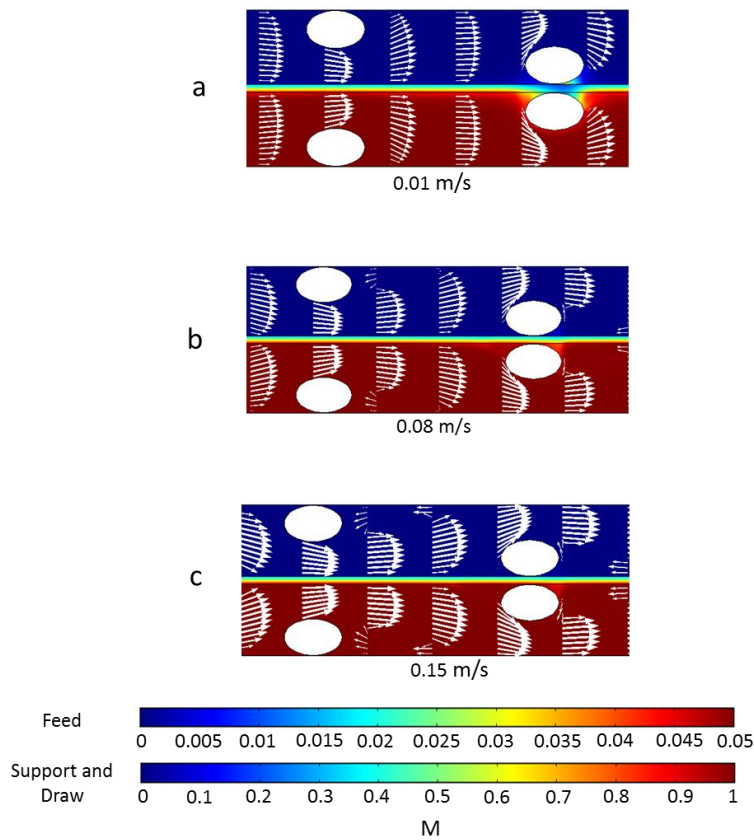


Figure 5-10. Concentration profile (indicated by the color flood) and velocity profile (indicated by the arrows) under different inlet velocities of spacer-filled membrane channel with $CC = 6$ mm. The size of the arrows is proportional to the logarithmic value of the velocity in order to better show vortices. These data were from the section whose distance to the entrance was approximately 14.5 to 20.5 mm.

In order to better understand why spacers functioned differently in flux enhancement under different velocities, the concentration and velocity profiles of spacer-filled membrane channels with $CC = 6$ mm and 0.01 mm distance from the filaments to the membrane were plotted in Fig. 5-10. In the flow profile, under velocity 0.08 (Fig. 5-10 b) and 0.15 m/s (Fig. 5-10 c), some velocity vectors with reverse direction were observed around the spacer filaments indicating vortices; however, in the channel with

0.01 m/s velocity such vortices were absent. The concentration profile under different velocities was different and the difference primarily existed in the draw channel. First of all, in the channel with 0.01 m/s velocity, a dead zone with apparent low concentration was observed on the draw side near the feed spacer that was close to the membrane while this dead zone was much less visible in channels with 0.08 m/s and 0.15 m/s velocity. In addition, even in the area that was not close to the spacer filaments, in the channel of 0.01 m/s velocity, a much thicker CP layer was found near the membrane surface on the draw side which is indicated by the light red color. This explains why in empty channels higher flux was observed with higher flow velocity. To sum up, it seemed that the higher inlet velocity would be able to create vortices near the feed spacer which minimized the dead zones near the spacer filaments. In addition, higher inlet velocity could also reduce the CP near the membrane surface even when the feed spacer was absent.

The impact of membrane-filament distance

Five different membrane-filament distance scenarios were studied, where the distances were 0, 0.01, 0.05, 0.1, 0.15 and 0.25 mm. Meanwhile, the same amount of space was also reserved as wall-filament distance (for alternating filaments). As a result, the sum of the membrane-filament distance and wall-filament distance took 0%, 2%, 10%, 20%, 30% and 50% of the channel height, respectively (Fig. 5-11).

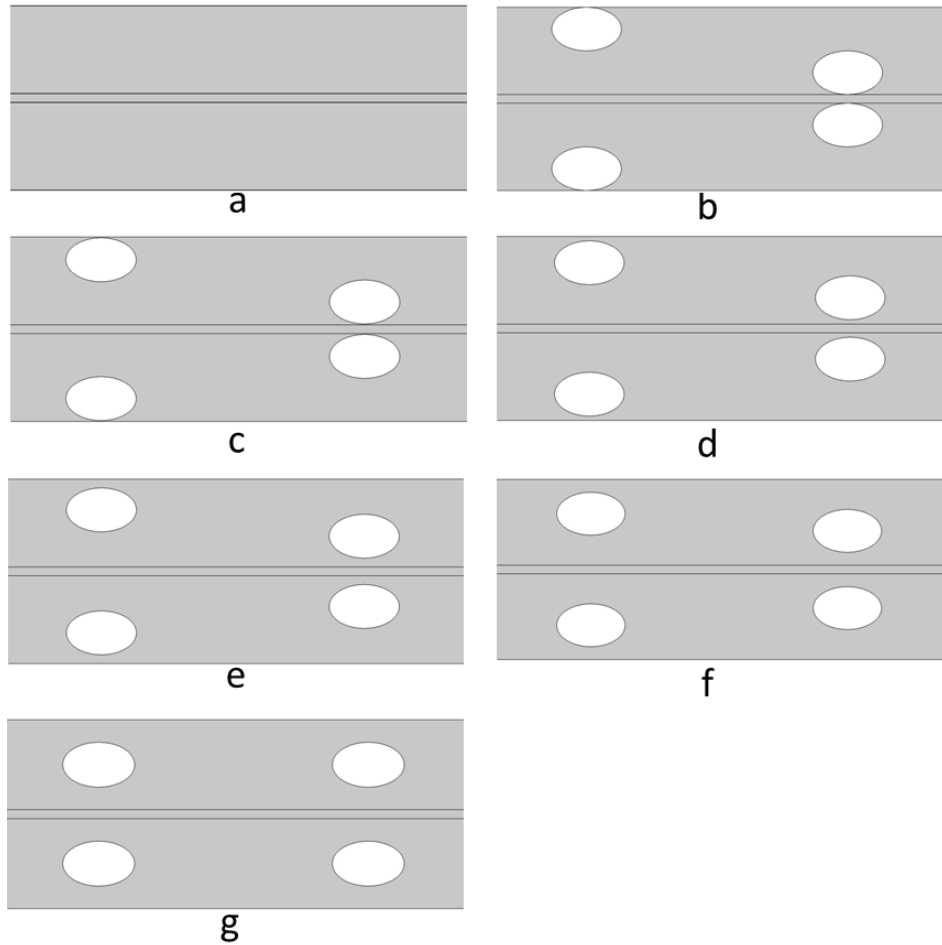


Figure 5-11. Illustration of (a) the empty channel and spacer-filled membrane channels with different membrane-filament distances (b) 0, (c) 0.01, (d) 0.05, (e) 0.1, (f) 0.15, and (g) 0.25 mm.

The permeate water flux from simulations with different membrane-filament distances is shown in Fig. 5-12. Permeate fluxes for the 0 mm distance under all velocities were the lowest because of surface blockage by the spacer. At the velocity 0.01 m/s, the flux in the spacer-filled membrane channels increased with the membrane-filament distance and only the channels with 0.1 mm and 0.15 mm membrane-filament distance had higher flux than the empty channel. For velocity 0.08 m/s and 0.15 m/s, the highest flux was observed at the 0.05 mm membrane-filament distance and the flux decreased as the distance continued to increase.

Fig. 5-12 also showed that the fluxes increased with the inlet velocity. However, the rates of the increment varied with velocity range and membrane-filament distance. The rate of permeate flux increment was much greater from 0.01 m/s to 0.08 m/s than from 0.08 m/s to 0.15 m/s indicating 0.08 m/s was the most economical velocity among the three as higher velocity would also incur higher energy cost in operation. In addition, the slopes of empty channel and spacer-filled membrane channel with 0 mm membrane-filament distance were very similar. However, for the spacer-filled membrane channels with non-zero headspace, the slope decreased as the membrane-filament distance increased. The fluxes from the channel with velocity of 0.08 m/s and 0.15 m/s and membrane-filament distance of 0.01 mm or higher were all greater than the empty membrane channel.

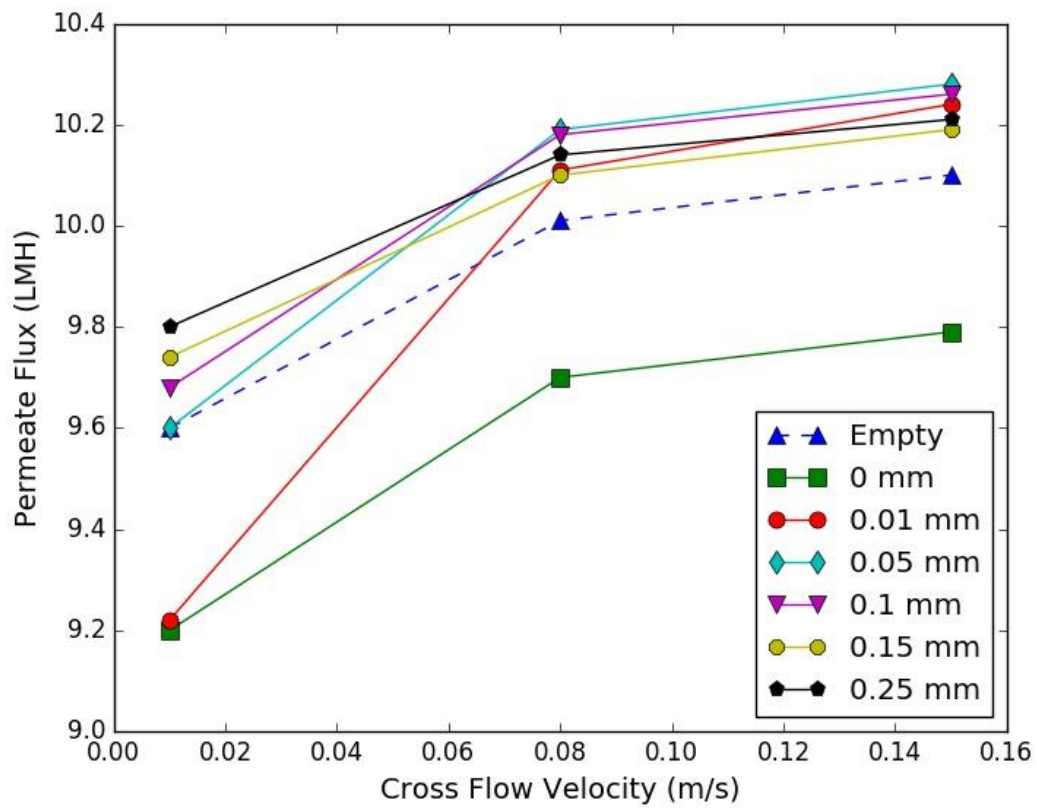


Figure 5-12. Permeate flux with different membrane-filament distances.

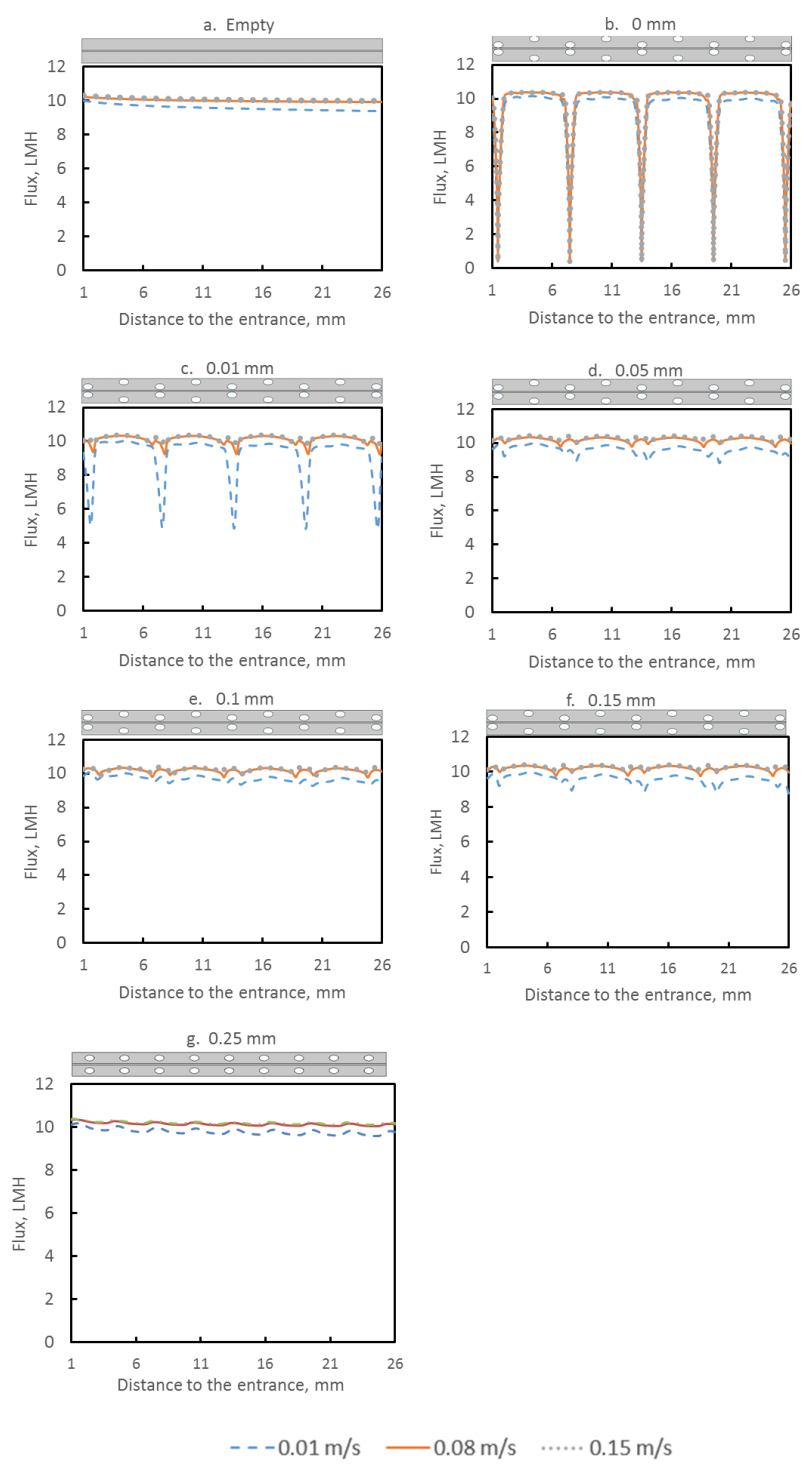


Figure 5-13. Water fluxes under different velocities along the membrane surface from the empty membrane channel and the spacer-filled membrane channels with various membrane-filament distances. The first and last 1 mm of the channel were excluded in order to remove entrance and exit effects. The sketch of the part of the channel whose data was presented was placed above the corresponding plot to illustrate the location of the spacer inside the membrane channel.

The local fluxes on the membrane surface are shown in Fig. 5-13. The flux profiles for membrane-filament distances from 0 mm to 0.05 mm were very distinct and those profiles suggested the impact of the spacer became smaller as the membrane-filament distance increased. The flux profiles became flatter and the flux profiles at the three velocities tended to be more similar as the membrane-filament distance increased. This is especially noted as the distance increased to 0.25 mm; the flux profiles in that channel became very similar to those in the empty channel, suggesting the impact of the spacer was very small when it was furthest from the membrane.

The velocity and concentration profiles for velocity 0.01 m/s and 0.15 m/s of various membrane-filament distances are shown in Fig. 5-14. Velocity 0.08 m/s was not shown in this plot as the result of Fig. 5-10, Fig. 5-12 and Fig. 5-13 suggested that the velocity and concentration profile for velocity 0.08 m/s would be very similar to velocity 0.15 m/s. Fig. 5-14 shows that both higher membrane-filament distance and velocity reduced the dead zones around the spacer near the membrane on the draw side. Also higher crossflow velocity suppressed the CP layer near the membrane on the draw side. It was also observed in Fig. 5-14 that the higher crossflow velocity created turbulence in spacer-filled channels; however, the turbulence started to diminish when the membrane-filament distance was increased from 0.05 mm to 0.1 mm or higher. The diminution of turbulence in channels with membrane-filament distance of 0.1 mm and 0.25 mm explains the reduction of permeate flux in those channels shown in Fig. 5-12.

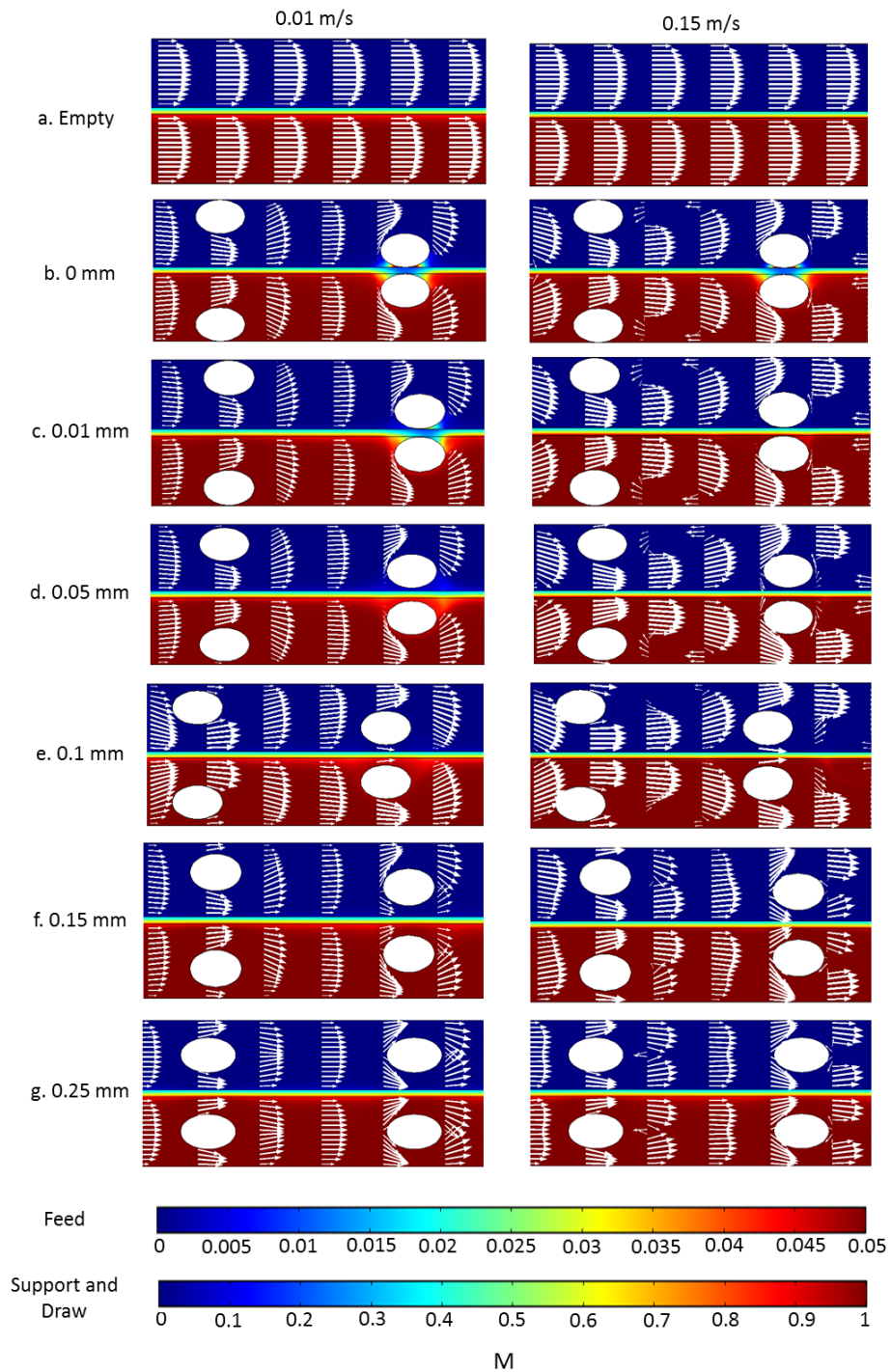


Figure 5-14. Concentration profile (indicated by the color flood) and velocity profile (indicated by the arrows) under different inlet velocities and membrane-filament distances for spacer-filled membrane channels with $CC = 6$ mm. The size of the arrows is proportional to the logarithmic value of the velocity in order to better show the vortices. These data were from the section whose distance to the entrance was approximately 14.5 to 20.5 mm.

3D Feed Spacer Filled FO Membrane Channel

In order to compare 2D and 3D modeling results, two series of sections (0° to the flow direction and 90° to the flow direction) were taken from the 3D model (Fig. 5-15).

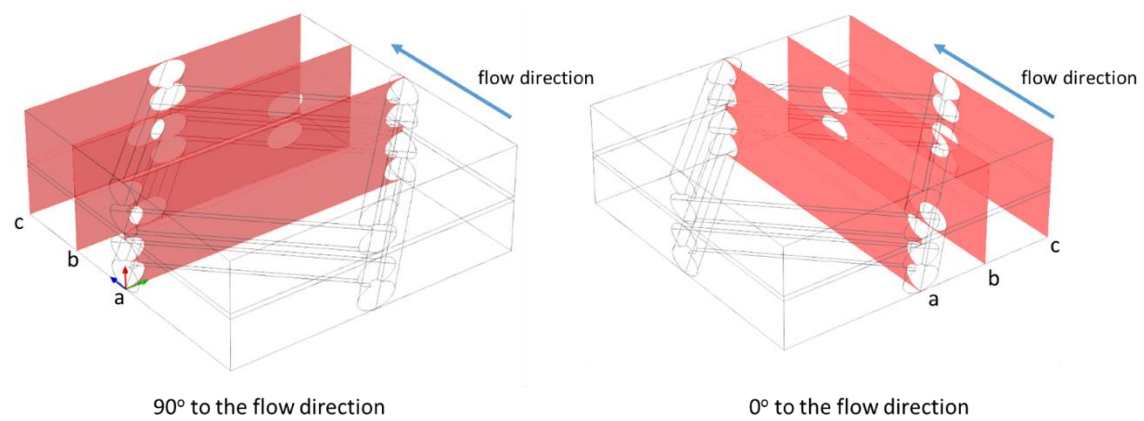


Figure 5-15. Two series of cross sectional slices selected from 3D modeling. On the left is the section perpendicular to the flow direction and on the right is the section parallel to the flow direction. The sections from both directions included (a) one center section, (b) one section between the center and boundary section and (c) one boundary section.

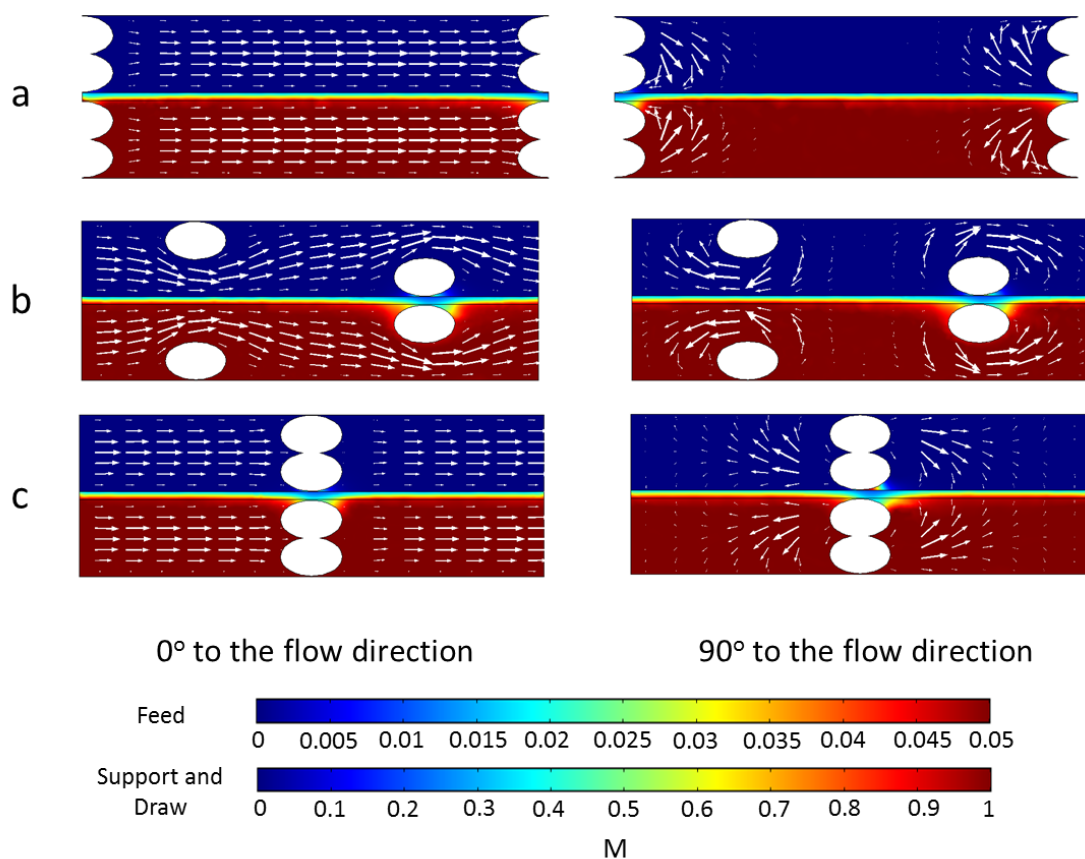


Figure 5-16. Concentration profile (indicated by the color flood) and velocity profile (indicated by the arrows) in the sections of the 3D model corresponding to Fig. 12. Velocity was 0.01 m/s. For each cross section, the size of the arrows is proportional to the value of the velocity.

As mentioned in the Materials and Methods, the limitation of fully coupled 3D multiphysics simulation was that it could only converge for velocity 0.01 m/s. The result of the concentration and velocity distribution from different cross sections are shown in Fig. 5-16. In the slices perpendicular to the main flow direction are seen vortex flow patterns near the spacer filaments, which 2D models could not show.

By comparing the results of 2D and 3D modeling in the slice that is similar to the 2D models, similar concentration profiles were found overall (Fig. 5-17). The velocity profiles from the two models were similar in the region between spacer filaments. There

was, however, a notable difference in velocity magnitudes in the areas above and below the spacer filaments. In the 2D model, the velocities above and below the spacer filaments were higher than those calculated in the 3D model. This is because in the 3D model the flow was able to travel around the filaments in multiple directions, but in 2D the flow was forced to go through the narrowed section of the channel.

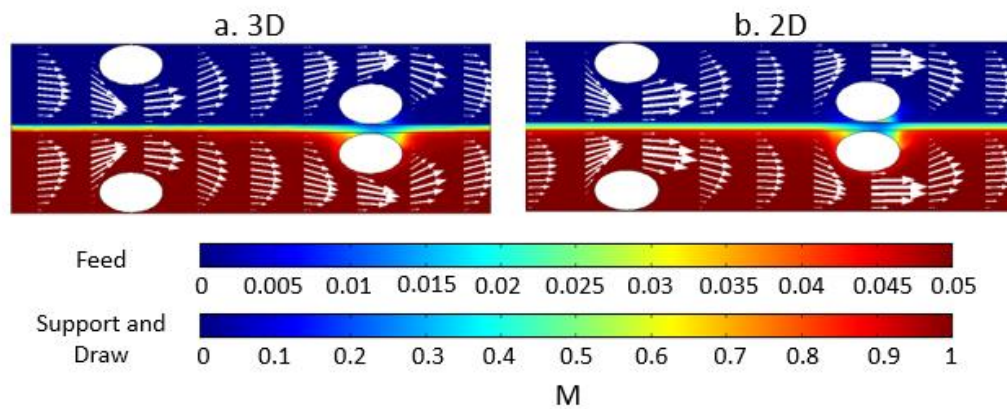


Figure 5-17. Concentration profile (indicated by the color flood) and velocity profile (indicated by the arrows) in (a) the middle section of the 3D model and (b) the section from the 2D model where the distance to the entrance was from 9.5 mm to 14.5 mm. The size of the arrows is proportional to the value of the velocity.

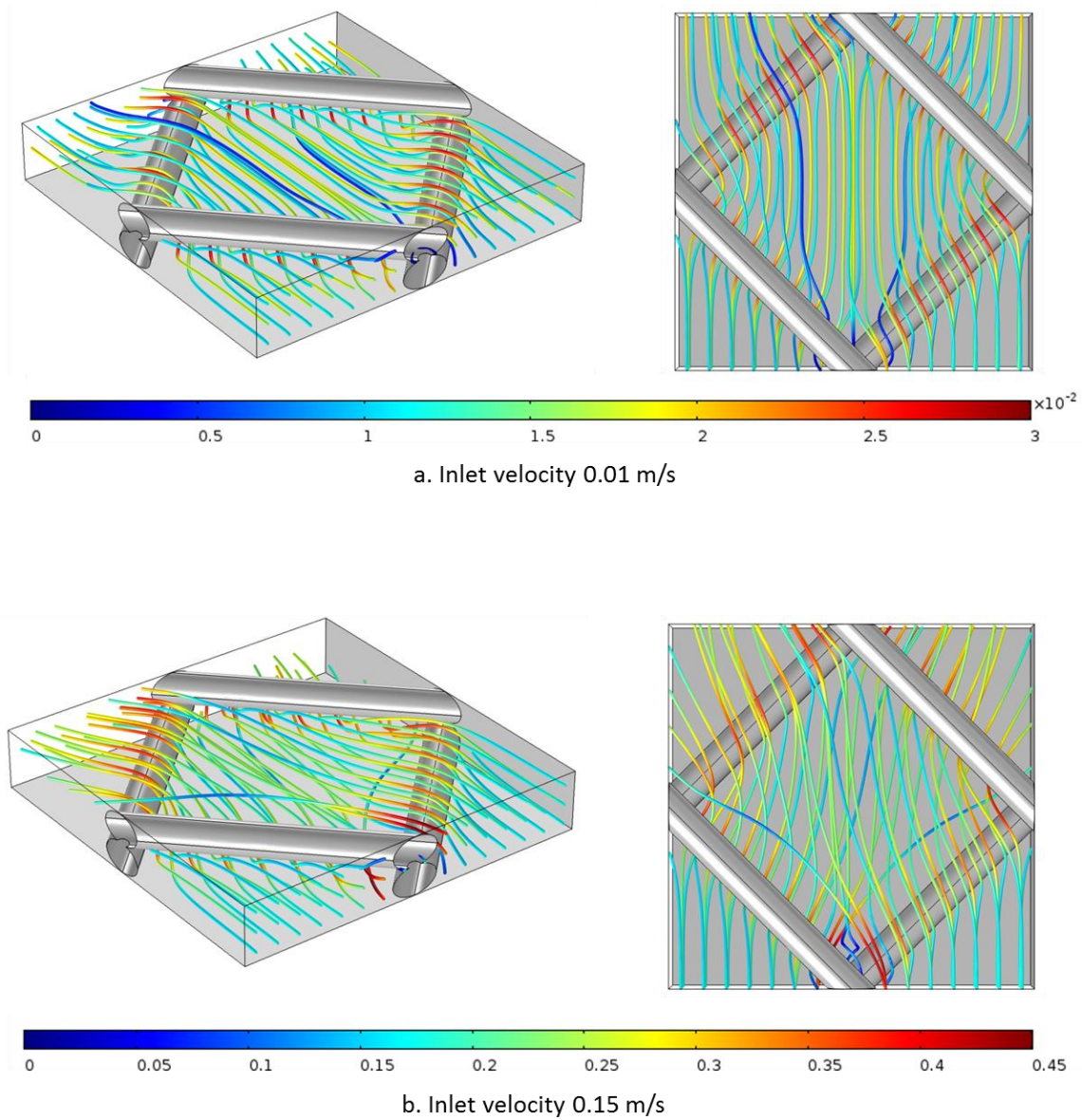


Figure 5-18. Velocity profiles inside 3D spacer-filled channels. The flow path is indicated by the streamline and the local velocity value is indicated by the color. Two inlet flow rates were tested: (a) $6 \times 10^{-7} \text{ m}^3/\text{s}$ (corresponding to inlet velocity 0.01 m/s) and (b) $9 \times 10^{-6} \text{ m}^3/\text{s}$ (corresponding to inlet velocity 0.15 m/s). For each flow rate, an orthogonal view (left) and top view (right) are provided.

In order to reveal more details of the flow in the 3D model, the flow path inside the spacer-filled membrane channel under different flow velocities are plotted in Fig. 5-18. This model focused on fluid flow without considering the mass transfer of the salt and

permeate flux to enable the model to converge. As the permeate flux was only 0.2% of the inlet flow rate, neglecting the permeate flux did not have a significant impact on the flow pattern inside the channel.

The streamlines show how water flowed around the spacer: the flow paths travelled over and under the filaments, but also deviated left and right to find paths of least resistance. Increasing inlet velocity enhanced the 3D flow pattern as we observed higher degrees of flow path cross-over with 0.15 m/s than 0.01 m/s. These results show that the 3D model was more suitable to capture the 3D pattern of the flow inside spacer-filled membrane channels especially in high crossflow velocities. The information garnered from 2D models in this study (such as local permeate flux results shown in Fig. 5-13) is thus expected to deviate from reality to some degree. We expect that 2D models do shed light on the phenomena at play and the general trends in behavior (such as general changes in flux as the membrane-filament distance changes), but local numerical accuracy may suffer. Further work at improving modeling capabilities is warranted, such as modifying the coupling methods between fluid flow and solute transport such that solutions can be found even for 3D simulations of complex spacer geometries. This is the subject of ongoing work in our lab.

Conclusion

This study showed that fully coupled multiphysics CFD models could predict the permeate flux in empty FO and PRO membrane channels based on hydrodynamics and mass transfer calculated by the simulation. This is a step forward in membrane modeling because most previous modeling efforts used mechanical pressure gradients or assigned

the flux during simulations based on experimental data. Here flux values were truly predicted; they depended only on solute concentrations that created an osmotic driving force.

Both 2D and 3D CFD models showed that the presence of spacers would be able to create vortices inside the membrane channel. Increasing flow velocity would augment the vortices; however, such an effect was much more obvious when increasing the velocity from 0.01 to 0.08 m/s than from 0.08 m/s to 0.15 m/s, which suggested diminishing returns as inlet velocity increased. The study also showed that the membrane-filament distance had an important impact on the hydrodynamics and mass transfer in the membrane channel. Increasing the distance reduced the dead zones in the vicinity of the spacer; however, it also reduced the vortices and thus decreased the permeate flux. It was observed that the permeate flux increased with membrane-filament distances from 0 mm to 0.05 mm but the flux decreased again as the distance continued to increase.

By comparing the 2D and 3D simulations, the concentration and velocity profiles from the same cross section were very similar. However, the 3D model was able to show more detailed flow and concentration profiles because it was able to explore all possible flow angles. It was difficult to create fully coupled 3D multiphysics models that could easily converge and even when convergence was achieved they required much more computational power and time than the 2D models. In this study, the fully coupled 3D multiphysics model was only able to converge under inlet velocity 0.01 m/s. Future work

is needed to create methods to make fully coupled 3D multiphysics models that can converge at higher inlet velocities for ODMPs.

CHAPTER SIX
CONCLUSION AND RECOMMENDATIONS

Conclusions

The important conclusions for this study are summarized below:

CFD Modeling and Experimental Evaluation for Concentration Polarization Mitigation with Sinusoidal Spacers:

- Using CFD models that fully coupled Navier-Stokes and convection-diffusion equations enabled visualization of the velocity and concentration profile inside RO membrane channels.
- The irreversible thermodynamics model was used to calculate permeate flux through the membrane. The result of permeate flux from CFD modeling matched with the experiments, suggesting CFD models are reliable in studying RO membrane desalination.
- It was shown that sinusoidal channels generated vortices with maximum flow velocities that increased with the amplitude and decreased with the wavelength of the sinusoid. The vortices increased mixing that reduced the concentration at the membrane, enhancing the permeate flux. The pressure drop, and thus the energy loss, increased with more tortuous sinusoids showing that an appropriate geometry must be designed to strike a balance between the benefits of enhanced flux and the costs of increased energy loss.

Mitigating membrane fouling with sinusoidal spacers:

- It was suggested that the vortices generated by sinusoidal spacers were able to elevate the local shear stress to decrease foulant deposition on the membrane surface thus reducing the flux decline caused by depositional membrane fouling. It was also confirmed by both simulations and experiments that deposition was greatest in low-velocity regions, but was reduced in high-velocity regions.
- The fouling distribution produced by simulation successfully predicted the local patterns of foulant accumulation in experiments.
- The results also showed that the channel $3\sin(\pi/6)$ was able to reduce the flux decline better with lower energy consumption compared to the conventional mesh spacer.

Computational Modeling of Fluid and Mass Transfer in Forward Osmosis and Pressure Retarded Osmosis:

- CFD models predicted the permeate flux from empty FO and PRO membrane channels via fully coupled Navier-Stokes, convection-diffusion, and irreversible thermodynamics equations.
- Both 2D and 3D CFD models showed that the flow velocity profiles were different as velocity changed. At higher velocities vortices were observed. The permeate flux data suggest that the vortices were beneficial for mass transfer enhancement.

- The study also showed that the membrane-filament distance had an important impact on the hydrodynamics and mass transfer in the membrane channel. Increasing the distance reduced the dead zones in the vicinity of the spacer; however, it also reduced the turbulence and thus decreased the permeate flux. It was observed that the permeate flux increased with membrane-filament distances from 0 mm to 0.05 mm but the flux decreased again as the distance continued to increase.
- By comparing the 2D and 3D simulation, the concentration and velocity profiles from the same cross section were similar. However, the 3D model was able to show more detailed flow and concentration profiles because it was able to show the results in different flow angles. These fully coupled 3D multiphysics models did not converge easily and required much more computational power and time than the 2D models.

Recommendations for Future research

- Explore other sinusoidal or unobstructed membrane channels to investigate if there is a better design that can achieve higher flux enhancement with lower energy consumption and fouling propensity. One potential direction is to modify the tested sinusoidal spacers on locations where lower velocities or higher foulants were observed.
- Use CFD models to study the biofilm growth during membrane filtration. The modeling method will be different from the humic acid model in two ways. First of all, the model will use different equations to simulation the growth of the biofilm. Second of all, the presence of biofilm will interfere with fluid flow by blocking the membrane channel. Therefore, it is necessary to fully couple the fluid flow, mass transfer and growth of the biofilm in a time-dependent study. One common way to simulate the biofilm is to treat it as a type of fluid with extremely high viscosity.
- Improve the 3D spacer-filled FO membrane model so that it can converge under higher velocity. In addition, if the computational capacity will allow in the future, it will be necessary to enlarge the size of the 3D model to reduce the entrance and exit effects and make it more comparable to the real scenario.

APPENDICES

Appendix A

The Mesh Scheme and Quality Sensitivity Test of CFD models

The mesh scheme and quality selection is of vital importance for the convergence and accuracy of the models. Mesh scheme refers to the strategy that determines which part of the geometry needs to be assigned with denser mesh elements to ensure the convergence. For example, in membrane desalination, a sharp concentration gradient was expected in a thin layer near the membrane surface, therefore, a layer mesh that consisted of 5 layers was employed near the membrane in order to capture the gradient for sinusoidal spacers (Fig. 3-4). The reason that layer mesh was chosen was that it is very thin and can be stretched to match the surface geometry. For ODMP models, boundary layer mesh was also used in 3D models but not in 2D models because in 2D models we were able to use even better mesh quality (Fig. 5-6 and 5-5). In RO models layer mesh was only applied to the membrane surface that faced the bulk flow, but in ODMP models layer mesh was applied to the membrane surfaces that face the bulk flow and the internal porous structure. As a result, four layer meshes were used. However, it should be noted that in the scenario where the membrane to filament distance was 0 mm, layer mesh could not be applied. As a result, in this scenario, no boundary layer mesh was used.

Mesh quality refers to the density of the number of mesh elements used in the model. The mesh quality is important for the accuracy of the results. For CFD models, it is very important to make sure the results would not be undermined by the poor mesh quality, however higher quality of mesh means higher requirement on computational

power. It is necessary to ensure that the results of the simulation will not change significantly when a denser mesh is used. Mesh quality sensitivity evaluation was used to determine the minimum mesh quality that could ensure the results would be independent of the mesh quality. During mesh density sensitivity evaluation, a series of mesh qualities were tested and the value of the simulation results were recorded. The test would be terminated if the difference of the results between the two simulations were under 1% while the mesh number difference was over 10%. An example of mesh quality sensitivity test is shown in Fig. A-1. The test was based the change of permeate flux and pressure drop with the change of mesh quality. It was shown that the value of the permeate flux and pressure drop were independent of mesh quality when mesh elements were larger than 750,000. Therefore, the required mesh quality for sinusoidal spacer $6\sin(\pi/6)$ was determined to be 750,000.

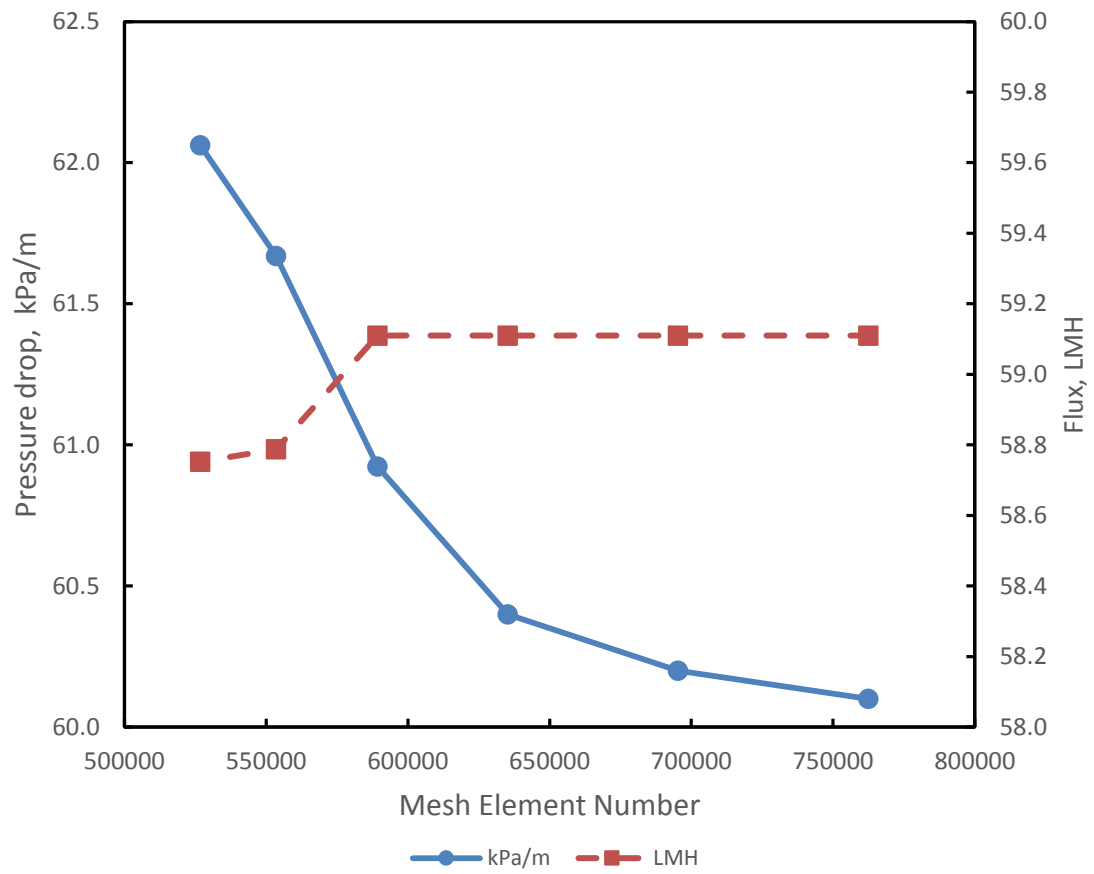


Figure A-1. Pressure drop and permeate flux under different mesh qualities in sinusoidal spacer $6\sin(\pi/6)$.

Appendix B

CFD Modeling on the Individual Impact of Spacers on the Feed and Draw Side of FO Membrane Channels

In order to investigate the impact of the spacers in the feed channel and draw channel individually a series of 2D models were built to simulate the scenarios where the spacers existed only in feed side, draw side or both feed and draw side under different cross flow velocities (0.05, 0.1 and 0.15 m/s) (Fig. B-1). The study also investigated the impact of the center-to-center (CC) distance on permeate flux. Three CC distances (10, 20 and 25 mm) were tested in this study (Fig. B-2).

The dimension of the feed and draw membrane channel is 77 mm long by 3 mm deep. The membrane type was HTI membrane from Chapter 5. It was shown in Fig. B-3 that the configuration of the spacer did not enhance the permeate flux. In addition, compared to the empty membrane channel the presence of spacer did not have significant impact on permeate flux.

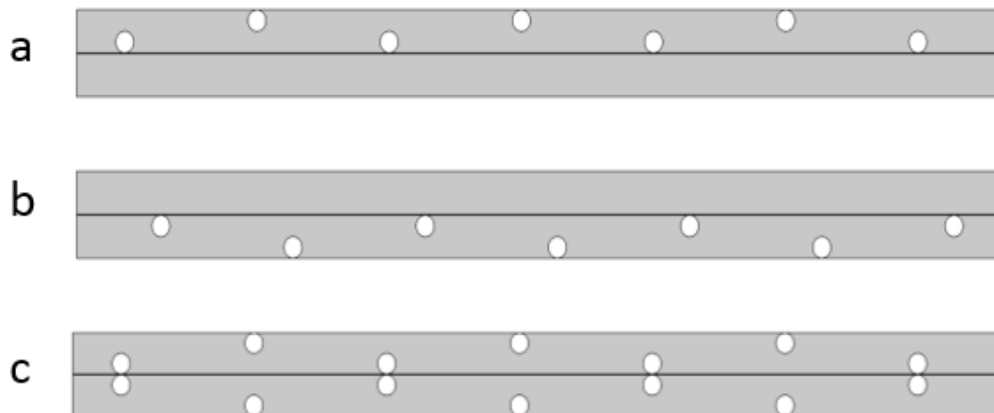


Figure B-1. Illustration of the spacer configurations. (a) the spacer only existed in the feed side; (b) the spacer only existed in the draw side; (c) the spacer existed in both feed and draw side. The filament to membrane distance is 0 mm and the CC distance is 12 mm.

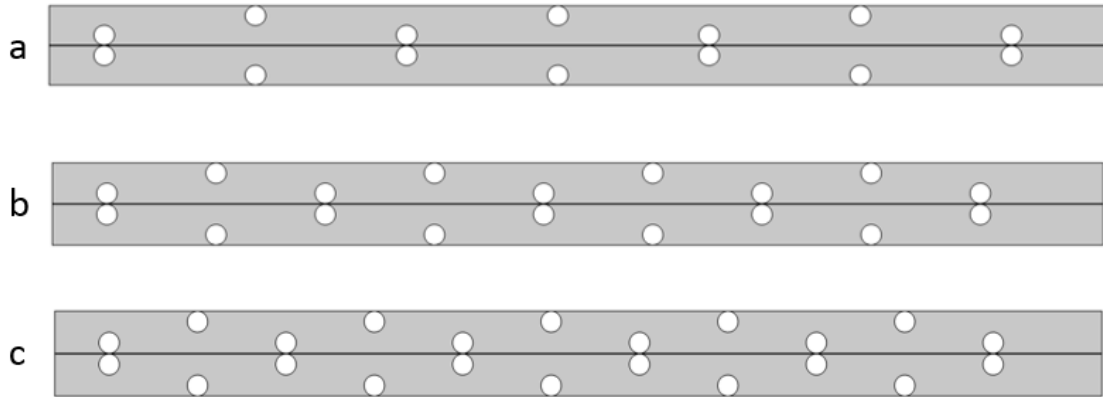


Figure B-2. Illustration of the spacer configurations. (a) CC distance is 12 mm (b) CC distance is 8 mm; (c) CC distance is 5 mm. The filament to membrane distance is 0 mm and the spacer existed in both the feed and draw side.

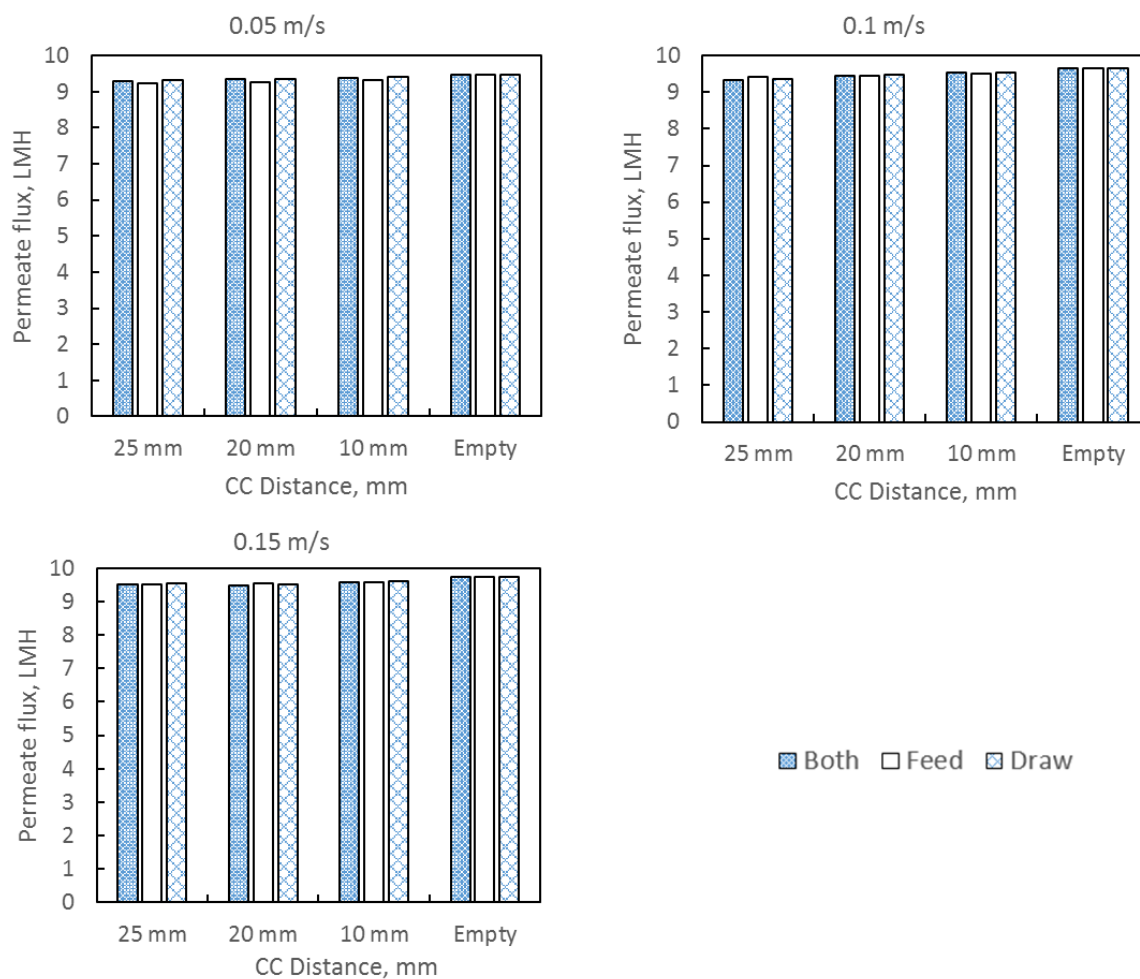


Figure B-3. Permeate flux from membrane channels with different flow velocity, CC distance and spacer configuration.

Appendix C

Models for Dissertation

This Appendix is a listing of the models used to generate the data in this dissertation. The electronic files are available from the author, or through David Ladner at Clemson University (ladner@clemson.edu). The model list below is intended to mimic the directory structure of the model files housed in the electronic repository.

MODELS FOR CHAPTER 3: HYDRODYNAMICS OF SINUSOIDAL SPACERS FOR IMPROVED REVERSE OSMOSIS PERFORMANCE

Most of the model names in this section begin with “y” denoting that an equation is envisioned in the file name. Then the file name contains information about the equation used and other information about the model. For example,

“y_3sin_pi12__p_1000_c_400_0.06.mph” uses the geometry of $y = 3 \sin(\pi x/12)$, with x being the distance from the entrance. “p_1000” denotes a pressure of 1000 psi. “c_400” denotes a solute concentration of 400 mol/m³. The trailing “0.06” denotes an inconsistent stabilization parameter of 0.06. “Straight” denotes a spacer with a straight (non-sinusoidal) channel.

$3\sin(\pi/12)$

y_3sin_pi12__p_1000_c_400_0.06.mph

y_3sin_pi12__p_1000_c_500_0.06.mph

y_3sin_pi12__p_1000_c_600_0.06.mph

y_3sin_pi12__p_800_c_600_0.06.mph

y_3sin_pi12__p_900_c_600_0.06.mph

3sin($\pi/6$)

y_3sin_pi6__p_1000_c_400_0.06.mph

y_3sin_pi6__p_1000_c_500_0.06.mph

y_3sin_pi6__p_1000_c_600_0.06.mph

y_3sin_pi6__p_800_c_600_0.06.mph

y_3sin_pi6__p_900_c_600_0.06.mph

6sin($\pi/6$)

y_6sin_pi6__p_1000_c_400_0.06.mph

y_6sin_pi6__p_1000_c_500_0.06.mph

y_6sin_pi6__p_1000_c_600_0.06.mph

y_6sin_pi6__p_800_c_600_0.06.mph

y_6sin_pi6__p_900_c_600_0.06.mph

6sin($\pi/12$)

y_6sin_pi12__p_1000_c_400_0.06.mph

y_6sin_pi12__p_1000_c_500_0.06.mph

y_6sin_pi12__p_1000_c_600_0.06.mph

y_6sin_pi12__p_800_c_600_0.06.mph

y_6sin_pi12__p_900_c_600_0.06.mph

Straight

straight__p_1000_c_400_0.06.mph

straight__p_1000_c_500_0.06.mph

straight__p_1000_c_600_0.06.mph

straight__p_800_c_600_0.06.mph

straight__p_900_c_600_0.06.mph

MODELS FOR CHAPTER 4: MITIGATING MEMBRANE FOULING WITH SINUSOIDAL SPACERS

The naming convention on these models is the same as in the Chapter 2 models section above, except that here, “with shear” means the adsorption equation includes a shear stress term and “without shear” means no shear stress term in the adsorption equation.

With shear

y_3sin_pi12__p_1000_c_00_with shear.mph

y_3sin_pi6__p_500_c_00_final4.2a) with shear.mph

y_6sin_pi12__p_500_c_00_final4.2a)with shear.mph

y_6sin_pi6__p_500_c_00_final4.2a)with shear.mph

y_straight__p_500_c_00_final4.2a)with shear.mph

Without shear

y_3sin_pi12__p_1000_c_00_without shear.mph

y_3sin_pi6__p_500_c_00_final4.2a) without shear.mph

y_6sin_pi12__p_500_c_00_final4.2a)without shear.mph

y_6sin_pi6__p_500_c_00_final4.2a)without shear.mph

y_straight__p_500_c_00_final4.2a)without shear.mph

MODELS FOR CHAPTER 6: COMPUTATIONAL MODELING OF FLUID FLOW AND MASS TRANSPORT IN FORWARD OSMOSIS AND PRESSURE RETARDED OSMOSIS

3D models

The names for these models begin with the dimensionality (3D). “FO1” denotes forward osmosis scenario #1, as described in Chapter 6. “YALE” denotes the institution that created the data set from which the membrane parameters were pulled. “HTI” is the membrane manufacturer, “elips” denotes the spacer shape, “hs001” denotes the head space (which was called “filament-membrane distance” in Chapter 6), “spacer” means a spacer was included in the model, and “001ms” denotes 0.01 m/s crossflow velocity.

3D no spacer FO1 YALE HTI elips hs0 spacer001ms.mph

3D no spacer FO1 YALE HTI elips hs001 spacer001ms.mph

3D no spacer FO1 YALE HTI elips hs005spacer001ms.mph

3D no spacer FO1 YALE HTI elips hs01spacer001ms.mph

2D models

The names for these models begin with the dimensionality (2D). “FO” denotes forward osmosis. “YALE” denotes the institution that created the data set from which the membrane parameters were pulled. “HTI” is the membrane manufacturer, “elips” denotes the spacer shape, “hs001” denotes the head space (which was called “filament-membrane distance” in Chapter 6), “spacer” means a spacer was included in the model, and “001ms” denotes 0.01 m/s crossflow velocity.

Verification based on Oasys

These models were used to verify whether CFD results matched the experimental data from Oasys in the literature [7].

2D FO HTI 05M 15M.mph
2D FO HTI 0M 1M.mph
2D FO OASYS 05M 15M .mph
2D FO OASYS 0M 1M .mph
2D PRO HTI 05M 15M.mph
2D PRO HTI 0M 1M.mph
2D PRO OASYS 0M 1M.mph
2D PRO oasys 05M 15M.mph

Verification based on Yale

These models were used to verify whether CFD results matched the experimental data from Yale in the literature [7].

2D FO HTI 05M 15M.mph
2D FO HTI 0M 1M.mph
2D FO OASYS 05M 15M.mph
2D FO OASYS 0M 1M .mph
2D PRO HTI 05M 15M.mph
2D PRO HTI 0M 1M.mph
2D PRO OASYS 05M 15M.mph
2D PRO OASYS 0M 1M .mph

Verification based on UConn

These models were used to verify whether CFD results matched the experimental data from the University of Connecticut in the literature [7].

2D FO CSM 05M 15M .mph
2D FO CSM 0M 1M.mph
2D FO HTI 05M 15M.mph
2D FO HTI 0M 1M.mph
2D PRO CSM 05M 15M.mph
2D PRO CSM 0M 1M.mph
2D PRO HTI 05M 15M.mph
2D PRO HTI 0M 1M.mph

Spacer CC10mm

These models had spacers with a center-to-center (CC) distance of 10 mm.

2D FO CSM 0M 1M with spacer in both 001mm.mph
2D FO CSM 0M 1M with spacer in draw 0.05mm.mph
2D FO CSM 0M 1M with spacer in draw head 001mm.mph
2D FO CSM 0M 1M with spacer in feed 0.05mm.mph
2D FO CSM 0M 1M with spacer in feed head 001mm.mph
2D FO CSM 0M 1M without spacer.mph
2D FO CSM 0M 1M with spacer in both 0.05.mph

Spacer CC12mm

These models had spacers with a center-to-center (CC) distance of 12 mm.

2D FO CSM 0M 1M with spacer both 001mm.mph
2D FO CSM 0M 1M with spacer in draw head 001mm.mph
2D FO CSM 0M 1M with spacer in feed head 001mm.mph

Spacer CC5mm

These models had spacers with a center-to-center (CC) distance of 5 mm.

2D FO CSM 0M 1M with spacer in both 001mm.mph

2D FO CSM 0M 1M with spacer in draw head 001mm.mph

2D FO CSM 0M 1M with spacer in feed head 001mm.mph

Spacer based on UConn

These models comprise the spacer-filled channel study with membrane properties based on experimental data from the University of Connecticut [7].

HTI

4 (indicating 4 mesh elements close to the membrane surface)

2D FO HTI 0M 1M uconn feed.mph

2D FO HTI 0M 1M uconn both.mph

2D FO HTI 0M 1M uconn draw.mph

5 (indicating 5 mesh elements close to the membrane surface)

2D FO HTI 0M 1M uconn feed.mph

2D FO HTI 0M 1M uconn both.mph

2D FO HTI 0M 1M uconn draw.mph

6 (indicating 6 mesh elements close to the membrane surface)

2D FO HTI 0M 1M uconn feed.mph

2D FO HTI 0M 1M uconn both.mph

2D FO HTI 0M 1M uconn draw.mph

TFC

4 (indicating 4 mesh elements close to the membrane surface)

2D FO TFC 0M 1M both uconn .mph

2D FO TFC 0M 1M draw uconn .mph

2D FO TFC 0M 1M feed uconn .mph

5 (indicating 5 mesh elements close to the membrane surface)

2D FO CSM 0M 1M with no spacer BOTH .mph

2D FO TFC 0M 1M draw uconn .mph

2D FO TFC 0M 1M feed .mph

6 (indicating 6 mesh elements close to the membrane surface)

2D FO CSM 0M 1M DRAW .mph

2D FO CSM 0M 1M with no spacer BOTH .mph

2D FO CSM 0M 1M with no spacer FEED .mph

Spacer based on Yale

These models comprise the spacer-filled channel study with membrane properties based on experimental data from the University of Connecticut [7].

HTI

4 (indicating 4 mesh elements close to the membrane surface)

2D FO HTI 0M 1M both.mph

2D FO HTI 0M 1M draw.mph

2D FO HTI 0M 1M feed.mph

5 (indicating 5 mesh elements close to the membrane surface)

2D FO HTI 0M 1M both.mph

2D FO HTI 0M 1M draw.mph

2D FO HTI 0M 1M feed.mph

6 (indicating 6 mesh elements close to the membrane surface)

2D FO HTI 0M 1M empty yale.mph

2D FO HTI 0M 1M both empty for 3D comparision.mph

2D FO HTI 0M 1M both with head space 0.01 CONSTANT B mm
for 3D comparision.mph

2D FO HTI 0M 1M both with head space 0.01mm for 3D
comparision.mph

2D FO HTI 0M 1M both with head space 0.01mm sparse for 3D
comparision.mph

2D FO HTI 0M 1M both with head space 0.01mm.mph

2D FO HTI 0M 1M both with head space 0.05mm constant Bfor
3D comparision.mph

2D FO HTI 0M 1M both with head space 0.05mm for 3D
comparision.mph

2D FO HTI 0M 1M both with head space 0.05mm.mph

2D FO HTI 0M 1M both with head space 0.15mm constant Bfor
3D comparision.mph

2D FO HTI 0M 1M both with head space 0.1mm for 3D
comparision.mph

2D FO HTI 0M 1M both with head space 0.1mm.mph

2D FO HTI 0M 1M both with head space 0.25mm for 3D
comparision.mph

2D FO HTI 0M 1M both with head space 0.25mm.mph

2D FO HTI 0M 1M both with head space 0.2mm constant B for

3D comparision.mph

2D FO HTI 0M 1M.mph

2D FO HTI 0M 1M both.mph

2D FO HTI 0M 1M draw.mph

2D FO HTI 0M 1M feed.mph

TFC

2D FO CSM 0M 1M with no spacer.mph
2D FO CSM 0M 1M with spacer in both .mph
2D FO CSM 0M 1M with spacer in draw .mph
2D FO CSM 0M 1M with spacer infeed .mph
2D FO CSM 0M 1M with spacer in both .mph
2D FO CSM 0M 1M with spacer in both 0.05.mph
2D FO CSM 0M 1M with spacer in draw .mph
2D FO CSM 0M 1M with spacer in feed .mph
2D FO CSM 0M 1M with spacer in feed.mph
2D FO CSM 0M 1M with spacer in both .mph
2D FO CSM 0M 1M with spacer in draw .mph
2D FO CSM 0M 1M with spacer in feed .mph
2D FO HTI 0M 1M both.mph
2D FO HTI 0M 1M.mph
2D FO CSM 0M 1M with spacer both head 001mm.mph
2D FO CSM 0M 1M with spacer in draw head 001mm.mph

REFERENCES

- [1] C. Fritzmann, J. Löwenberg, T. Wintgens, T. Melin, State-of-the-art of reverse osmosis desalination, *Desalination*. 216 (2007) 1–76. doi:10.1016/j.desal.2006.12.009.
- [2] J. Schwinge, P.R. Neal, D.E. Wiley, D.F. Fletcher, a. G. Fane, Spiral wound modules and spacers: Review and analysis, *J. Memb. Sci.* 242 (2004) 129–153. doi:10.1016/j.memsci.2003.09.031.
- [3] C. Charcosset, A review of membrane processes and renewable energies for desalination, *Desalination*. 245 (2009) 214–231. doi:10.1016/j.desal.2008.06.020.
- [4] K. Lutchmiah, a R.D. Verliefe, K. Roest, L.C. Rietveld, E.R. Cornelissen, Forward osmosis for application in wastewater treatment: a review., *Water Res.* 58 (2014) 179–97. doi:10.1016/j.watres.2014.03.045.
- [5] J.R. McCutcheon, M. Elimelech, Influence of concentrative and dilutive internal concentration polarization on flux behavior in forward osmosis, *J. Memb. Sci.* 284 (2006) 237–247. doi:10.1016/j.memsci.2006.07.049.
- [6] M. Park, J.H. Kim, Numerical analysis of spacer impacts on forward osmosis membrane process using concentration polarization index, *J. Memb. Sci.* 427 (2013) 10–20. doi:10.1016/j.memsci.2012.09.045.
- [7] T.Y. Cath, M. Elimelech, J.R. McCutcheon, R.L. McGinnis, A. Achilli, D. Anastasio, A.R. Brady, A.E. Childress, I. V. Farr, N.T. Hancock, J. Lampi, L.D. Nghiem, M. Xie, N.Y. Yip, Standard Methodology for Evaluating Membrane Performance in Osmotically Driven Membrane Processes, *Desalination*. 312 (2013) 31–38. doi:10.1016/j.desal.2012.07.005.
- [8] Q. She, D. Hou, J. Liu, K.H. Tan, C.Y. Tang, Effect of feed spacer induced membrane deformation on the performance of pressure retarded osmosis (PRO): Implications for PRO process operation, *J. Memb. Sci.* 445 (2013) 170–182. doi:10.1016/j.memsci.2013.05.061.
- [9] Z. Zhou, J.Y. Lee, T.S. Chung, Thin film composite forward-osmosis membranes with enhanced internal osmotic pressure for internal concentration polarization reduction, *Chem. Eng. J.* 249 (2014) 236–245. doi:10.1016/j.cej.2014.03.049.
- [10] G. Han, J. Zhou, C. Wan, T. Yang, T.-S. Chung, Investigations of inorganic and organic fouling behaviors, antifouling and cleaning strategies for pressure retarded

- osmosis (PRO) membrane using seawater desalination brine and wastewater, *Water Res.* 103 (2016) 264–275. doi:10.1016/j.watres.2016.07.040.
- [11] K.L. Hickenbottom, J. Vanneste, M. Elimelech, T.Y. Cath, Assessing the current state of commercially available membranes and spacers for energy production with pressure retarded osmosis, *Desalination*. (2015). doi:http://dx.doi.org/10.1016/j.desal.2015.09.029.
- [12] U.T. Boris Liberman, Gal Greenberg, Vitaly Levitin, Tal Oz-Ari, Three Pressure Retarded (PRO) Process, (n.d.).
- [13] S. Sarp, Z. Li, J. Saththasivam, Pressure Retarded Osmosis (PRO): Past experiences, current developments, and future prospects, *Desalination*. 389 (2016) 2–14. doi:10.1016/j.desal.2015.12.008.
- [14] J.R. McCutcheon, R.L. McGinnis, M. Elimelech, A novel ammonia—carbon dioxide forward (direct) osmosis desalination process, *Desalination*. 174 (2005) 1–11. doi:10.1016/j.desal.2004.11.002.
- [15] D.L. Shaffer, N.Y. Yip, J. Gilron, M. Elimelech, Seawater desalination for agriculture by integrated forward and reverse osmosis: Improved product water quality for potentially less energy, *J. Memb. Sci.* 415–416 (2012) 1–8. doi:10.1016/j.memsci.2012.05.016.
- [16] A. Alturki, J. McDonald, S.J. Khan, F.I. Hai, W.E. Price, L.D. Nghiem, Performance of a novel osmotic membrane bioreactor (OMBR) system: flux stability and removal of trace organics., *Bioresour. Technol.* 113 (2012) 201–6. doi:10.1016/j.biortech.2012.01.082.
- [17] S. Lin, Mass transfer in forward osmosis with hollow fiber membranes, *J. Memb. Sci.* 514 (2016) 176–185. doi:10.1016/j.memsci.2016.04.053.
- [18] J.W. Carter, G. Hoyland, A.P.M. Hasting, Concentration polarisation in reverse osmosis flow systems under laminar conditions. Effect of surface roughness and fouling, *Chem. Eng. Sci.* 29 (1974) 1651–1658. doi:10.1016/0009-2509(74)87017-X.
- [19] J. Fárková, The pressure drop in membrane module with spacers, *J. Memb. Sci.* 64 (1991) 103–111. doi:10.1016/0376-7388(91)80081-G.
- [20] S. Karode, A. Kumar, Flow visualization through spacer filled channels by computational fluid dynamics I.Pressure drop and shear rate calculations for flat sheet geometry, *J. Memb. Sci.* 193 (2001) 69–84. doi:10.1016/S0376-7388(01)00494-X.

- [21] M. Shakaib, S.M.F. Hasani, M. Mahmood, CFD modeling for flow and mass transfer in spacer-obstructed membrane feed channels, *J. Memb. Sci.* 326 (2009) 270–284. doi:10.1016/j.memsci.2008.09.052.
- [22] S.A. Avlonitis, K. Kouroumbas, N. Vlachakis, Energy consumption and membrane replacement cost for seawater RO desalination plants, *Desalination.* 157 (2003) 151–158. doi:10.1016/S0011-9164(03)00395-3.
- [23] G.T. Gray, J.R. McCutcheon, M. Elimelech, Internal concentration polarization in forward osmosis: role of membrane orientation, *Desalination.* 197 (2006) 1–8. doi:10.1016/j.desal.2006.02.003.
- [24] J. Phattaranawik, R. Jiratananon, A.G. Fane, Effects of net-type spacers on heat and mass transfer in direct contact membrane distillation and comparison with ultrafiltration studies, *J. Memb. Sci.* 217 (2003) 193–206. doi:10.1016/S0376-7388(03)00130-3.
- [25] F. Li, W. Meindersma, A.B. de Haan, T. Reith, Novel spacers for mass transfer enhancement in membrane separations, *J. Memb. Sci.* 253 (2005) 1–12. doi:10.1016/j.memsci.2004.12.019.
- [26] L. Song, S. Ma, Numerical Studies of the Impact of Spacer Geometry on Concentration Polarization in Spiral Wound Membrane Modules, *Ind. Eng. Chem. Res.* 44 (2005) 7638–7645. doi:10.1021/ie048795w.
- [27] S. Ma, L. Song, Numerical study on permeate flux enhancement by spacers in a crossflow reverse osmosis channel, *J. Memb. Sci.* 284 (2006) 102–109. doi:10.1016/j.memsci.2006.07.022.
- [28] L. Song, S. Yu, Concentration polarization in cross-flow reverse osmosis, *AIChE J.* 45 (1999) 921–928. doi:10.1002/aic.690450502.
- [29] W.W. Focke, P.G.J.M. Nuijens, Velocity profile caused by a high porosity spacer between parallel plates (membranes), *Desalination.* 49 (1984) 243–253. doi:10.1016/0011-9164(84)85036-5.
- [30] A.S. Berman, Laminar Flow in Channels with Porous Walls, *J. Appl. Phys.* 24 (1953) 1232. doi:10.1063/1.1721476.
- [31] A. Subramani, S. Kim, E.M. V Hoek, Pressure, flow, and concentration profiles in open and spacer-filled membrane channels, *J. Memb. Sci.* 277 (2006) 7–17. doi:10.1016/j.memsci.2005.10.021.
- [32] G. a. Fimbres-Weihs, D.E. Wiley, Review of 3D CFD modeling of flow and mass transfer in narrow spacer-filled channels in membrane modules, *Chem. Eng.*

- Process. *Process Intensif.* 49 (2010) 759–781. doi:10.1016/j.cep.2010.01.007.
- [33] M.F. Gruber, C.J. Johnson, C. Tang, M.H. Jensen, L. Yde, C. Helix-Nielsen, Validation and analysis of forward osmosis CFD model in complex 3D geometries, *Membranes (Basel)*. 2 (2012) 764–782. doi:10.3390/membranes2040764.
- [34] Y.Y. Liang, M.B. Chapman, G. a. Fimbres Weihs, D.E. Wiley, CFD modelling of electro-osmotic permeate flux enhancement on the feed side of a membrane module, *J. Memb. Sci.* 470 (2014) 378–388. doi:10.1016/j.memsci.2014.07.039.
- [35] A. Alexiadis, D.E. Wiley, A. Vishnoi, R.H.K. Lee, D.F. Fletcher, J. Bao, CFD modelling of reverse osmosis membrane flow and validation with experimental results, *Desalination*. 217 (2007) 242–250. doi:10.1016/j.desal.2007.02.014.
- [36] P. Xie, L.C. Murdoch, D.A. Ladner, Hydrodynamics of sinusoidal spacers for improved reverse osmosis performance, *J. Memb. Sci.* 453 (2014) 92–99. doi:10.1016/j.memsci.2013.10.068.
- [37] M. Park, J.H. Kim, Numerical analysis of spacer impacts on forward osmosis membrane process using concentration polarization index, *J. Memb. Sci.* 427 (2013) 10–20. doi:10.1016/j.memsci.2012.09.045.
- [38] G.A. Fimbres-Weihs, D.E. Wiley, Review of 3D CFD modeling of flow and mass transfer in narrow spacer-filled channels in membrane modules, *Chem. Eng. Process. Process Intensif.* 49 (2010) 759–781. doi:10.1016/j.cep.2010.01.007.
- [39] A.L. Ahmad, K.K. Lau, Impact of different spacer filaments geometries on 2D unsteady hydrodynamics and concentration polarization in spiral wound membrane channel, *J. Memb. Sci.* 286 (2006) 77–92. doi:10.1016/j.memsci.2006.09.018.
- [40] C. Picioreanu, J.S. Vrouwenvelder, M.C.M. Van Loosdrecht, Three-dimensional modeling of biofouling and fluid dynamics in feed spacer channels of membrane devices, *J. Memb. Sci.* 345 (2009) 340–354. doi:10.1016/j.memsci.2009.09.024.
- [41] S. Ma, L. Song, Numerical study on permeate flux enhancement by spacers in a crossflow reverse osmosis channel, *J. Memb. Sci.* 284 (2006) 102–109. doi:10.1016/j.memsci.2006.07.022.
- [42] J. Schwinge, Characterization of a zigzag spacer for ultrafiltration, *J. Memb. Sci.* 172 (2000) 19–31. doi:10.1016/S0376-7388(00)00312-4.
- [43] V. Geraldés, V. Semião, M.N. de Pinho, The effect of the ladder-type spacers configuration in NF spiral-wound modules on the concentration boundary layers disruption, *Desalination*. 146 (2002) 187–194. doi:10.1016/S0011-9164(02)00467-

8.

- [44] V. Geraldes, V. Semiao, M. Norberta de Pinho, Concentration polarisation and flow structure within nanofiltration spiral-wound modules with ladder-type spacers, *Comput. Struct.* 82 (2004) 1561–1568. doi:10.1016/j.compstruc.2004.03.052.
- [45] J. Schwinge, D.E. Wiley, a. G. Fane, Novel spacer design improves observed flux, *J. Memb. Sci.* 229 (2004) 53–61. doi:10.1016/j.memsci.2003.09.015.
- [46] F. Li, G.W. Meindersma, a. B. De Haan, T. Reith, Optimization of non-woven spacers by CFD and validation by experiments, *Desalination.* 146 (2002) 209–212. doi:10.1016/S0011-9164(02)00472-1.
- [47] G.A. Fimbres-Weihs, D.E. Wiley, Numerical study of mass transfer in three-dimensional spacer-filled narrow channels with steady flow, *J. Memb. Sci.* 306 (2007) 228–243. doi:10.1016/j.memsci.2007.08.043.
- [48] N. Delgrange, C. Cabassud, M. Cabassud, L. Durand-Bourlier, J.M. Lainé, Modelling of ultrafiltration fouling by neural network, *Desalination.* 118 (1998) 213–227. doi:10.1016/S0011-9164(98)00132-5.
- [49] S. Lee, W.S. Ang, M. Elimelech, Fouling of reverse osmosis membranes by hydrophilic organic matter: Implications for water reuse, *Desalination.* 187 (2006) 313–321. doi:10.1016/j.desal.2005.04.090.
- [50] M. Amin Saad, Early discovery of RO membrane fouling and real-time monitoring of plant performance for optimizing cost of water, *Desalination.* 165 (2004) 183–191. doi:10.1016/j.desal.2004.06.021.
- [51] S. Zou, Y.-N. Wang, F. Wicaksana, T. Aung, P.C.Y. Wong, A.G. Fane, C.Y. Tang, Direct microscopic observation of forward osmosis membrane fouling by microalgae: Critical flux and the role of operational conditions, *J. Memb. Sci.* 436 (2013) 174–185. doi:10.1016/j.memsci.2013.02.030.
- [52] S. Kim, E.M.V. Hoek, Modeling concentration polarization in reverse osmosis processes, *Desalination.* 186 (2005) 111–128. doi:10.1016/j.desal.2005.05.017.
- [53] K. Touati, F. Tadeo, Study of the Reverse Salt Diffusion in pressure retarded osmosis: Influence on concentration polarization and effect of the operating conditions, *Desalination.* 389 (2016) 171–186. doi:10.1016/j.desal.2016.02.014.
- [54] H. Strathmann, B. Keilin, Control of concentration polarization in reverse osmosis desalination of water, *Desalination.* 6 (1969) 179–201. doi:10.1016/0011-9164(69)80003-2.

- [55] S. Ma, L. Song, S. Ong, W. Ng, A 2-D streamline upwind Petrov/Galerkin finite element model for concentration polarization in spiral wound reverse osmosis modules, *J. Memb. Sci.* 244 (2004) 129–139. doi:10.1016/j.memsci.2004.06.048.
- [56] H.K.L.R.L.R. Ulrich Merten, Boundary-layer effects in reverse osmosis, *I&EC Fundam.* (1960) 2–5.
- [57] A. Siddiqui, N. Farhat, S.S. Bucs, R.V. Linares, C. Picioreanu, J.C. Kruithof, M.C.M. van Loosdrecht, J. Kidwell, J.S. Vrouwenvelder, Development and characterization of 3D-printed feed spacers for spiral wound membrane systems, *Water Res.* 91 (2016) 55–67. doi:10.1016/j.watres.2015.12.052.
- [58] H. Chang, J.-A. Hsu, C.-L. Chang, C.-D. Ho, T.-W. Cheng, Simulation study of transfer characteristics for spacer-filled membrane distillation desalination modules, *Appl. Energy.* (2015). doi:10.1016/j.apenergy.2015.12.030.
- [59] J.S. Vrouwenvelder, D. a. Graf von der Schulenburg, J.C. Kruithof, M.L. Johns, M.C.M. van Loosdrecht, Biofouling of spiral-wound nanofiltration and reverse osmosis membranes: A feed spacer problem, *Water Res.* 43 (2009) 583–594. doi:10.1016/j.watres.2008.11.019.
- [60] G. Kang, Y. Cao, Development of antifouling reverse osmosis membranes for water treatment: A review., *Water Res.* 46 (2012) 584–600. doi:10.1016/j.watres.2011.11.041.
- [61] Y. Baek, J. Yu, S.H. Kim, S. Lee, J. Yoon, Effect of surface properties of reverse osmosis membranes on biofouling occurrence under filtration conditions, *J. Memb. Sci.* 382 (2011) 91–99. doi:10.1016/j.memsci.2011.07.049.
- [62] J. Balster, D.F. Stamatialis, M. Wessling, Membrane with integrated spacer, *J. Memb. Sci.* 360 (2010) 185–189. doi:10.1016/j.memsci.2010.05.011.
- [63] G. Schock, A. Miquel, Mass transfer and pressure loss in spiral wound modules, *Desalination.* 64 (1987) 339–352. doi:10.1016/0011-9164(87)90107-X.
- [64] W. Li, K.K. Chen, Y.-N. Wang, W.B. Krantz, A.G. Fane, C.Y. Tang, A conceptual design of spacers with hairy structures for membrane processes, *J. Memb. Sci.* 510 (2016) 314–325. doi:10.1016/j.memsci.2016.03.021.
- [65] J.S. Vrouwenvelder, J.W.N.M. Kappelhof, S.G.J. Heijman, J.C. Schippers, D. van der Kooij, Tools for fouling diagnosis of NF and RO membranes and assessment of the fouling potential of feed water, *Desalination.* 157 (2003) 361–365. doi:10.1016/S0011-9164(03)00417-X.
- [66] D. Jermann, W. Pronk, R. Kägi, M. Halbeisen, M. Boller, Influence of interactions

- between NOM and particles on UF fouling mechanisms, *Water Res.* 42 (2008) 3870–3878. doi:10.1016/j.watres.2008.05.013.
- [67] T. Lin, Z. Lu, W. Chen, Interaction mechanisms and predictions on membrane fouling in an ultrafiltration system, using the XDLVO approach, *J. Memb. Sci.* 461 (2014) 49–58. doi:10.1016/j.memsci.2014.03.022.
- [68] L. Song, Flux decline in crossflow microfiltration and ultrafiltration: mechanisms and modeling of membrane fouling, *J. Memb. Sci.* 139 (1998) 183–200. doi:10.1016/S0376-7388(97)00263-9.
- [69] N. Lee, G. Amy, J.P. Croué, H. Buisson, Identification and understanding of fouling in low-pressure membrane (MF/UF) filtration by natural organic matter (NOM), *Water Res.* 38 (2004) 4511–4523. doi:10.1016/j.watres.2004.08.013.
- [70] J.S. Choi, J.T. Kim, Modeling of full-scale reverse osmosis desalination system: Influence of operational parameters, *J. Ind. Eng. Chem.* 21 (2014) 261–268. doi:10.1016/j.jiec.2014.02.033.
- [71] J.S. Vrouwenvelder, D.A. Graf von der Schulenburg, J.C. Kruithof, M.L. Johns, M.C.M. van Loosdrecht, Biofouling of spiral-wound nanofiltration and reverse osmosis membranes: a feed spacer problem., *Water Res.* 43 (2009) 583–94. doi:10.1016/j.watres.2008.11.019.
- [72] P. Araújo, D.J. Miller, P.B. Correia, M.C.M. Van Loosdrecht, J.C. Kruithof, B.D. Freeman, D.R. Paul, J.S. Vrouwenvelder, Impact of feed spacer and membrane modification by hydrophilic, bactericidal and biocidal coating on biofouling control, *Desalination.* 295 (2012) 1–10. doi:10.1016/j.desal.2012.02.026.
- [73] S.R. Suwarno, X. Chen, T.H. Chong, V.L. Puspitasari, D. McDougald, Y. Cohen, S.A. Rice, A.G. Fane, The impact of flux and spacers on biofilm development on reverse osmosis membranes, *J. Memb. Sci.* 405 (2012) 219–232. doi:10.1016/j.memsci.2012.03.012.
- [74] T. Tran, B. Bolto, S. Gray, M. Hoang, E. Ostarcevic, An autopsy study of a fouled reverse osmosis membrane element used in a brackish water treatment plant, *Water Res.* 41 (2007) 3915–3923. doi:10.1016/j.watres.2007.06.008.
- [75] M. Gimmelshtein, R. Semiat, Investigation of flow next to membrane walls, *J. Memb. Sci.* 264 (2005) 137–150. doi:10.1016/j.memsci.2005.04.033.
- [76] R. Iwatsu, K. Ishii, T. Kawamura, K. Kuwahara, J.M. Hyun, Numerical simulation of three-dimensional flow structure in a driven cavity, *Fluid Dyn. Res.* 5 (1989) 173–189. doi:10.1016/0169-5983(89)90020-8.

- [77] W.S. Kim, J.K. Park, H.N. Chang, Mass transfer in a three-dimensional net-type turbulence promoter, *Int. J. Heat Mass Transf.* 30 (1987) 1183–1192. doi:10.1016/0017-9310(87)90047-0.
- [78] R. Ikan, Aquatic humic substances—Influence on fate and treatment of pollutants, *Org. Geochem.* 15 (1990) 219. doi:10.1016/0146-6380(90)90087-G.
- [79] Z. Domanya, I. Galambosb, G. Vataib, E. Bekassy-molnarb, Humic substances removal from drinking water by membrane filtration, *Desalination.* 145 (2002) 333–337.
- [80] M.F. a. Goosen, S.S. Sablani, H. Al-Hinai, S. Al-Obeidani, R. Al-Belushi, D. Jackson, Fouling of Reverse Osmosis and Ultrafiltration Membranes: A Critical Review, *Sep. Sci. Technol.* 39 (2005) 2261–2297. doi:10.1081/SS-120039343.
- [81] M.R. Esfahani, H. a. Stretz, M.J.M. Wells, Comparing humic acid and protein fouling on polysulfone ultrafiltration membranes: Adsorption and reversibility, *J. Water Process Eng.* 6 (2015) 83–92. doi:10.1016/j.jwpe.2015.03.001.
- [82] A.I. Schäfer, M. Mastrup, R.L. Jensen, Particle interactions and removal of trace contaminants from water and wastewaters, *Desalination.* 147 (2002) 243–250. doi:10.1016/S0011-9164(02)00544-1.
- [83] E. Salehi, S.S. Madaeni, Adsorption of humic acid onto ultrafiltration membranes in the presence of protein and metal ions, *Desalination.* 263 (2010) 139–145. doi:10.1016/j.desal.2010.06.050.
- [84] K.L. Jones, C.R. O’Melia, Protein and humic acid adsorption onto hydrophilic membrane surfaces: Effects of pH and ionic strength, *J. Memb. Sci.* 165 (2000) 31–46. doi:10.1016/S0376-7388(99)00218-5.
- [85] S.M.G. Demneh, B. Nasernejad, H. Modarres, Modeling investigation of membrane biofouling phenomena by considering the adsorption of protein, polysaccharide and humic acid., *Colloids Surf. B. Biointerfaces.* 88 (2011) 108–14. doi:10.1016/j.colsurfb.2011.06.018.
- [86] P. Kanagaraj, A. Nagendran, D. Rana, T. Matsuura, Separation of macromolecular proteins and removal of humic acid by cellulose acetate modified UF membranes, *Int. J. Biol. Macromol.* (2016). doi:10.1016/j.ijbiomac.2016.04.054.
- [87] K. Li, T. Huang, F. Qu, X. Du, A. Ding, G. Li, H. Liang, Performance of adsorption pretreatment in mitigating humic acid fouling of ultrafiltration membrane under environmentally relevant ionic conditions, *Desalination.* 377 (2016) 91–98. doi:10.1016/j.desal.2015.09.016.

- [88] M. Elimelech, S. Bhattacharjee, A novel approach for modeling concentration polarization in crossflow membrane filtration based on the equivalence of osmotic pressure model and filtration theory, *J. Memb. Sci.* 145 (1998) 223–241. doi:10.1016/S0376-7388(98)00078-7.
- [89] A. Sagiv, A. Zhu, P.D. Christofides, Y. Cohen, R. Semiat, Analysis of forward osmosis desalination via two-dimensional FEM model, *J. Memb. Sci.* 464 (2014) 161–172. doi:10.1016/j.memsci.2014.04.001.
- [90] S. Zhao, L. Zou, C.Y. Tang, D. Mulcahy, Recent developments in forward osmosis: Opportunities and challenges, *J. Memb. Sci.* 396 (2012) 1–21. doi:10.1016/j.memsci.2011.12.023.
- [91] H. Zhang, S. Cheng, F. Yang, Use of a spacer to mitigate concentration polarization during forward osmosis process, *Desalination.* 347 (2014) 112–119. doi:10.1016/j.desal.2014.05.026.
- [92] C.H. Tan, H.Y. Ng, Revised external and internal concentration polarization models to improve flux prediction in forward osmosis process, *Desalination.* 309 (2013) 125–140. doi:10.1016/j.desal.2012.09.022.
- [93] W. Li, Y. Gao, C.Y. Tang, Network modeling for studying the effect of support structure on internal concentration polarization during forward osmosis: Model development and theoretical analysis with FEM, *J. Memb. Sci.* 379 (2011) 307–321. doi:10.1016/j.memsci.2011.05.074.
- [94] C.H. Tan, H.Y. Ng, Modified models to predict flux behavior in forward osmosis in consideration of external and internal concentration polarizations, *J. Memb. Sci.* 324 (2008) 209–219. doi:10.1016/j.memsci.2008.07.020.
- [95] R. Valladares Linares, S.S. Bucs, Z. Li, M. AbuGhdeeb, G. Amy, J.S. Vrouwenvelder, Impact of spacer thickness on biofouling in forward osmosis, *Water Res.* 57 (2014) 223–233. doi:10.1016/j.watres.2014.03.046.
- [96] D.S. Kamenetskiy, On the relation of the Embedded Discontinuous Galerkin method to the stabilized residual-based finite element methods, *Appl. Numer. Math.* 108 (2016) 271–285. doi:10.1016/j.apnum.2016.01.004.
- [97] M. Wurst, M. Keßler, E. Krämer, A high-order Discontinuous Galerkin Chimera method for laminar and turbulent flows, *Comput. Fluids.* 121 (2015) 102–113. doi:10.1016/j.compfluid.2015.08.013.
- [98] Comsol, Comsol Multiphysics User’s Guide, Heat Transf. Branch. (2012) 709–745, The Heat Transfer Branch.

- [99] S. Of, G. Approximations, O.F. Transport, E. By, S. Modeling, Jean-Luc Guermond 1, *Math. Model. Numer. Anal.* (1999).
- [100] M.M. Clark, *Transport Modeling for Environmental Engineers and Scientists*, Second Edition, John Wiley & Sons, Hoboken, 2009.
- [101] R. McGinnis, G. McGurgan, Patent application of forward osmosis membranes by Oasys Water, Inc., 2010.
- [102] A. Tiraferri, N.Y. Yip, W.A. Phillip, J.D. Schiffman, M. Elimelech, Relating performance of thin-film composite forward osmosis membranes to support layer formation and structure, *J. Memb. Sci.* 367 (2011) 340–352.
doi:10.1016/j.memsci.2010.11.014.
- [103] W.A. Phillip, J.D. Schiffman, M. Elimelech, High performance thin-film membrane, *Environ. Sci. Technol.* 44 (2010) 3812–3818.
- [104] V. a Jambhekar, *Forchheimer Porous-media Flow Models - Numerical Investigation and Comparison with Experimental Data*, (2011) 85.
- [105] M.M.A. Shirazi, A. Kargari, A.F. Ismail, T. Matsuura, Computational Fluid Dynamic (CFD) opportunities applied to the membrane distillation process: State-of-the-art and perspectives, *Desalination.* 377 (2016) 73–90.
doi:10.1016/j.desal.2015.09.010.
- [106] G. Guillen, E.M.V. Hoek, Modeling the impacts of feed spacer geometry on reverse osmosis and nanofiltration processes, *Chem. Eng. J.* 149 (2009) 221–231.
doi:10.1016/j.cej.2008.10.030.